Enzymatic and Non-Enzymatic Aspects of Biosensor Design

A thesis submitted

in partial fulfillment of the

requirements for the degree of

Doctor of Philosophy

by

Ms. Sheetal Das

226159101

Jyoti and Bhupat Mehta School of

Health Science and Technology

Indian Institute of Technology, Guwahati

June 2026

C E R T I F I C A T E

It is certified that the works contained in this thesis, entitled "**Enzymatic and non-enzymatic aspects of Biosensor Design**" by Ms. Sheetal Das, have been carried out under my supervision and have not been submitted as a thesis elsewhere for a Ph.D degree.

Thesis supervisor

Prof. Rajiv K Kar

Assistant Professor

Jyoti and Bhupat Mehta School of Health Sciences and Technology

Indian Institute of Technology Guwahati

June, 2026

Dedicated to My *Family*

Acknowledgment

I am deeply grateful to my thesis supervisor, **Dr Rajiv Kumar Kar** for his mentorship and academic guidance during my doctoral journey. Despite his hectic work schedule, he always found time to offer essential suggestions to improve my work. I am extremely thankful to my doctoral committee members, **Prof. Siddhartha Sankar Ghosh**, **Prof. Selvaraju Narayanasamy** and **Prof. Ranjan Tamuli** from Department of Biosciences and Bioengineering Engineering, for their invaluable suggestions and rendering me fit for an early submission of my PhD.

I am also thankful to my senior, mentor, and collaborator, **Mr. Prathu Raja Parmar**, for his constant guidance and encouragement. My sincere thanks to Prof. **Omkar Suresh Deshmukh** from the Department of Chemical Engineering for his time, kind encouragement, and for being approachable whenever guidance was needed. I am deeply grateful to my batchmates and friends **Anusua, Pooja, Shimpy** and **Shikha**, for being constant companions throughout this journey.

I acknowledge my parents Sri **Samir Kumar Das** and Smt **Swarna Prava Das**, whose belief in education never wavered. I acknowledge Stormy, whose presence grounded me during difficult times. I acknowledge the science itself, the experiments that failed repeatedly before they worked. I acknowledge the people who helped directly, whether through discussions, resources, technical assistance, or timely advice. Your contributions mattered, even if you may not realize how much.

I also acknowledge, without bitterness, the experiences that did not go as planned. These experiences sharpened my boundaries, strengthened my independence, and forced growth that comfort never could. This thesis carries the imprint of those lessons.

I am also thankful to my friend and lab member **Mr. Ravishankar Srivastava**, for his consistent support throughout my PhD journey. I am thankful to all my lab members. I thank all my PhD seniors, juniors, and batchmates for stepping in and helping me directly or indirectly.

Special thanks to all the faculty and staff members of **the Jyoti and Bhupat Mehta School of Health Sciences and Technology, IIT Guwahati**, for providing consistent administrative support and access to the facilities and resources that were essential for the successful completion of this research work. I also want to thank the Centre for Nanotechnology and Central Instruments Facility, IIT Guwahati, for their support and cooperation.

Contents

List of Figures

List of Tables

Nomenclature

A. Abbreviations

AuNP: Gold Nanoparticle

LSPR: Localized Surface Plasmon Resonance

SPR: Surface Plasmon Resonance

DTSSP: 3,3′-[Dithiobis(sulfosuccinimidyl propionate)]

DSP: [Dithiobis(succinimidyl propionate)]

NHS: N-hydroxysuccinimide

MD: Molecular Dynamics

EDX: Energy Dispersive X-ray Spectroscopy

TEM: Transmission Electron Microscopy

HRTEM: High-Resolution Transmission Electron Microscopy

SAED: Selected Area Electron Diffraction

XRD: X-ray Diffraction

UV–Vis: Ultraviolet–Visible Spectroscopy

GRAVY: Grand Average of Hydropathicity

pI: Isoelectric Point

RMSD: Root Mean Square Deviation

RMSF: Root Mean Square Fluctuation

fcc: Face-Centered Cubic

B. Units

nm: Nanometer

Å: Angstrom

ns: Nanosecond

mg: Milligram

mL: Milliliter

µM: Micromolar

rpm: Revolutions per minute

°C: Degree Celsius

L: Liter

g: Gram

Chapter 1

Introduction

Abstract

This work compiles both enzymatic and non-enzymatic strategies in the design of advanced biosensing platforms. The enzymatic component of this work focuses on allantoinase, a key enzyme involved in purine catabolism associated with oxidative stress. A comprehensive bioinformatic and structural evaluation of allantoinases from multiple species was performed to identify physicochemical determinants critical for enzyme immobilization. Parameters including solubility, hydrophobicity, compactness, disorder propensity, thermostability, and solvent accessibility were systematically analyzed to rank enzyme suitability for biosensing applications. This establishes design criteria for enzyme-based sensing platforms with improved stability and catalytic efficiency. The non-enzymatic component centers on the rational functionalization of gold nanoparticles (AuNPs) as plasmonic transducers. Comparative experimental studies were conducted using two bifunctional thiol linkers, DTSSP and DSP, to investigate concentration-dependent sensing from its adsorption behavior, colloidal stability, and localized surface plasmon resonance (LSPR) modulation. Distinct differences in surface coverage, aggregation tendencies, and optical red-shift responses between the two linkers were obtained. DTSSP exhibited pronounced concentration-dependent aggregation and significant SPR red shifts, whereas DSP demonstrated comparatively minimal spectral changes, highlighting the influence of linker chemistry on plasmonic signal transduction. To complement experimental observations, all-atom molecular dynamics simulations were performed to examine linker–AuNP interactions at the molecular level. Computational modelling provided mechanistic insight into adsorption energetics, surface coordination, and stability, enabling a correlation between atomistic behaviour and macroscopic optical responses. Collectively, this work integrates enzymatic characterisation, quantitative surface chemistry, adsorption thermodynamics, and molecular simulation into a coherent strategy for biosensor development. This thesis advances the fundamental understanding of enzymatic and non-enzymatic biosensing strategies.

Introduction and Literature Review

1.1 Oxidative Stress and Allantoin as a Clinical Biomarker

Oxidative stress arises when the generation of reactive oxygen species (ROS) exceeds the capacity of antioxidant defenses, leading to damage to lipids, proteins, and nucleic acids.[1,2] This imbalance is implicated in the onset and progression of a wide range of pathologies, including metabolic disorders, cardiovascular disease, chronic kidney disease, neurodegeneration, and inflammatory conditions.[3,4] Because ROS themselves are short-lived and highly reactive, their presence is typically inferred indirectly through chemically more stable downstream products formed by the oxidative modification of endogenous metabolites.[5,6] The quantitative assessment of such products has therefore become central to redox biology and clinical chemistry, both for mechanistic studies and for diagnostic or prognostic applications.

Among the numerous oxidative stress biomarkers proposed like F2-isoprostanes, protein carbonyls, 8-hydroxy-2′-deoxyguanosine, and thiobarbituric acid reactive substances (TBARS), urine oxidation products occupy a special place because of their direct relationship to cellular energy metabolism and purine catabolism.[7,8] Uric acid, the end product of purine metabolism in humans, is particularly susceptible to non-enzymatic oxidation by ROS, generating several oxidation products, of which allantoin has emerged as a robust marker of systemic oxidative damage. Unlike many lipid peroxidation markers, allantoin is chemically stable, can be measured in minimally invasive matrices such as urine and serum, and its formation in humans is almost exclusively non-enzymatic, thereby directly reflecting oxidative processes rather than confounded enzymatic pathways.

1.1.1 Allantoin as a Non-Enzymatic Oxidation Product of Uric Acid

Several clinical and translational studies have demonstrated elevated allantoin levels in conditions associated with heightened oxidative stress, including chronic renal failure, metabolic syndrome, and inflammatory diseases.[9,10] Patients with chronic renal failure showed significantly higher allantoin concentrations in both plasma and erythrocytes compared to healthy controls, supporting its utility as a marker of oxidative damage in renal dysfunction.[11] In gout and hyperuricemic states, serum allantoin is increased and correlates with disease severity, reflecting enhanced oxidation of uric acid during chronic inflammation and crystal-induced oxidative bursts. Moreover, allantoin has been proposed as a sensitive biomarker in exercise-induced oxidative stress and environmental exposure studies.[12] These

findings position allantoin as a promising, non-invasive oxidative stress biomarker linked to metabolic perturbations, inflammation, and renal dysfunction.

1.1.2 Limitations of Current Allantoin Detection Methods

For routine clinical and point-of-care applications, however, sensitive, selective, and rapid analytical methods are needed to quantify allantoin in complex biological matrices.[13] Conventional chromatographic techniques, although highly accurate, often require elaborate sample preparation, expensive equipment, and trained personnel, limiting their use outside specialized laboratories. This has motivated the development of enzymatic and biosensing strategies that leverage the specificity of biocatalysts, for example, toward allantoin or its metabolic context. In this regard, allantoinase, the hydrolase that converts allantoin to allantoate in plants and lower organisms, has been exploited as a recognition element for biosensors targeting allantoin in biological samples.[14]

1.1.3 Enzymatic Recognition: Allantoinase as a Biocatalytic Element

Allantoinase catalyzes the ring-opening hydrolysis of allantoin, and when coupled with appropriate secondary reactions or detection chemistries, it enables the transduction of allantoin levels into measurable optical or electrochemical signals.[15] Enzyme-based sensing offers several advantages: high substrate specificity, potential for signal amplification through catalytic turnover, and operation under physiologically relevant conditions. Yet, the practical realization of allantoinase-based sensors requires a detailed understanding of enzymatic parameters such as Michaelis–Menten kinetics, turnover numbers, pH and temperature optima, and inhibition or activation by matrix components. Moreover, the immobilisation of allantoinase onto suitable transducer surfaces must preserve its activity and stability while supporting robust signal generation.[16] These considerations motivate a systematic investigation of allantoinase kinetics and immobilisation strategies as a foundation for biosensor development targeting allantoin and, by extension, oxidative stress and associated metabolic and renal disorders.

Despite substantial advances in redox biology, the routine clinical assessment of oxidative stress still relies predominantly on chromatographic and mass spectrometric techniques that are labour-intensive, instrument-dependent, and unsuitable for rapid or point-of-care deployment. Although allantoin is a chemically stable and physiologically relevant oxidation product of uric acid, it remains underutilised in clinical diagnostics due to the lack of simple, selective, and miniaturizable detection platforms. Integrating enzymatic specificity

with plasmonic transduction offers a promising strategy to overcome these limitations, enabling rapid, sensitive, and potentially portable detection of oxidative stress biomarkers through controlled nanobiointerfacial engineering.

1.2. Plasmonic Gold Nanoparticles in Biosensing

Gold nanoparticles (AuNP) are widely used nanocomponents in biosensors for the detection of target analytes. The ease of surface functionalization, such as modification of AuNP with thiol groups (Brust-Schiffrin method), ligands, antibodies, or DNA, allows tuning of sensors to target very specific analytes.[17] A key advantage of AuNPs is their high surface-to-volume ratio, suitable for efficient binding to the target molecule and enhancing sensitivity at low analyte concentration.[18] Additional critical properties that render high suitability for sensing applications include their inertness,[19] resistance against oxidation,[20] thereby supporting long-term performance.[21] The principle behind their use in sensing is based on surface plasmon resonance (SPR), where the electrons in gold nanoparticles oscillate in response to light.[22] This property is also linked to the quantum size effect where changes in the electronic and optical properties of AuNPs takes place when the size becomes comparable to that of de Broglie wavelength of electrons.[23] In principle, the continuous energy band level of bulk gold particles becomes discrete when the particle size reduces to a few nanometers, which is referred to as quantum confinement.[24] The SPR phenomena can be observed through UV-vis spectroscopy, the synthesis of citrate-stabilised AuNPs, and the principle of SPR detection using the Kretschmann configuration are illustrated in Fig. 1.1.[25] The approach allows researchers to detect angle shifts in reflected light, which are caused by increased perturbations at the metal-solution interface and by the mass increase on the AuNP surface. Importantly, the SPR phenomenon occurs in continuous thin films, where the coupling of light striking and the excitation causes a dip in reflected light intensity at a specific resonance angle. Though the phenomenon can be effectively captured through a prism, the relative change in wavelength can be detected using a straightforward optical setup, as reported by several researchers. Localised SPR (LSPR) is a similar phenomenon that involves oscillation of electrons, which occurs in metallic nanoparticles and results in strong absorption and scattering of light at the resonance wavelength.[26] The Kretschmann configuration is the most widely used method for conventional SPR sensing, where biomolecular interactions are monitored through shifts in the resonance angle.[25] Alternatively, localised surface plasmon resonance (LSPR) sensors based on metallic nanoparticles enable detection through shifts in the plasmon resonance wavelength, allowing simpler optical instrumentation without the need for prism-based angular interrogation.

The peak position and intensity of LSPR bands are highly sensitive to size,[27] shape,[28] aggregation,[29] and refractive index[30] of the surrounding environment. Henceforth, the quantum size effect is critical in controlling and tuning the properties of AuNPs, particularly for application in optoelectronics and biosensing.

1.2.1 Role of Surface Chemistry in Optical Stability

Surface chemistry plays a decisive role in governing the optical stability of gold nanoparticles (AuNPs).[31] The density and organisation of surface-bound linkers directly influence interparticle interactions and aggregation behaviour. At low surface coverage, insufficient steric or electrostatic stabilisation can permit nanoparticles to approach closely, promoting plasmonic coupling and red shifts in the localised surface plasmon resonance (LSPR) band. Conversely, higher linker densities can enhance colloidal stability by introducing steric barriers and/or electrostatic repulsion, thereby maintaining interparticle separation and preserving a sharp, well-defined SPR peak. Interparticle plasmonic coupling is highly distance-dependent, with nanometer-scale changes in spacing leading to significant spectral shifts and band broadening. In addition, the surface charge imparted by functional ligands modulates zeta potential and governs long-range electrostatic interactions in solution, further influencing dispersion stability. Therefore, precise control over linker chemistry, surface coverage, and charge distribution is essential for achieving reproducible optical responses and stable plasmonic performance in AuNP-based biosensing platforms. Thus, surface functionalization is the central determinant of plasmonic response.

Additionally, the quantum size effect is also responsible for generating fluorescence, which is relatively weaker compared to traditional fluorophores.[32] However, it is observed only when AuNPs are small-sized.[33] The strategy that has been implemented to harness the fluorescence effect is via surface modification, where a tagged fluorescence can influence via a phenomenon called fluorescence resonance energy transfer.[34] The application has been demonstrated not only for biosensing but also in the field of bioimaging.[35]

In addition to the experimental proceedings, significant advancements in computational resources have transformed the integration of molecular computation into research. Understanding the structural arrangement and electronic and chemical properties of AuNPs is crucial for complementing and interpreting the experimental observations.[36] The insights at the atomic and molecular levels are crucial for assigning the spectral changes such as acquisition from UV-vis, FT-IR, and Raman. Density functional theory (DFT)[37] and molecular dynamics (MD) simulations for modelling gold clusters and nanoparticles allow

predicting their stability, binding modes, and charge transfer characteristics. Researchers have also used such *in silico* results to uncover the mechanism governing the AuNP's complex behavior, as demonstrated through microscopy and catalytic assays. Further, these simulations have accelerated the rational design and optimisation of AuNP's property for specific applications in sensing and biomedicine.

1.3 Applications of AuNP-Based Biosensing Platforms

This section reviews recent advances in the use of surface-functionalized gold nanoparticles (AuNPs) for the detection of biologically and clinically relevant analytes. Particular emphasis is placed on how nanoparticle size, shape, surface chemistry, and interfacial architecture influence sensitivity, selectivity, and signal amplification in optical and electrochemical sensing platforms. The discussion also addresses surface-induced processes at the nano–bio interface, including protein adsorption, enzyme immobilisation, antibody orientation, and conformational modulation, as characterised through spectroscopic and microscopic techniques. Finally, computational approaches such as molecular dynamics simulations and quantum chemical calculations are introduced as complementary tools for interpreting experimental observations and guiding the rational design of high-performance plasmonic biosensors.

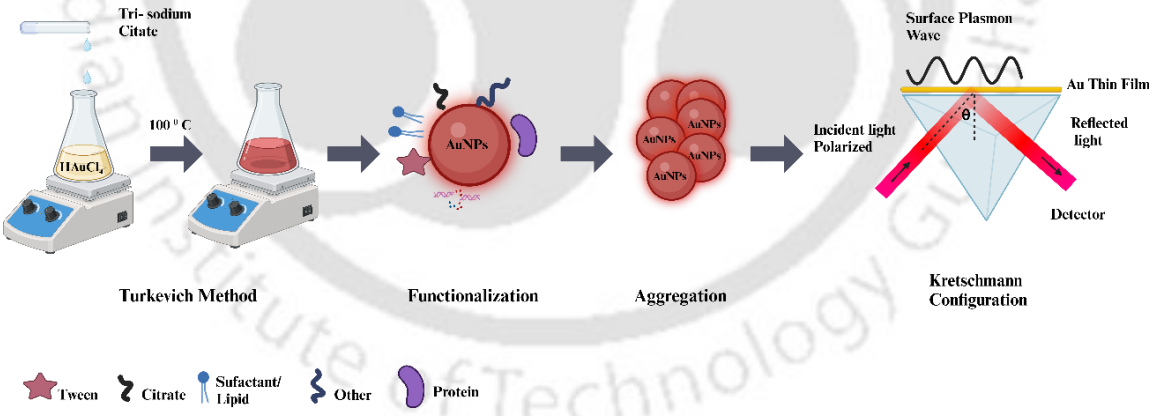

Figure 1.1: Schematic representation of citrate-mediated synthesis of AuNPs and Kretschmann SPR configuration

1.3.1 Gold nanoparticle for the sensing of small molecules and metabolites

AuNPs have emerged as a versatile nanomaterial for engineering with biorecognition elements in sensors owing to their electrical, optical, and surface properties. In particular, the strong surface plasmon resonance, high surface-to-volume ratio, and ease of surface functionalization make them excellent candidates for developing sensitive and selective detection platforms. These processes include surface engineering with functional ligands,

biomolecules, and nanocomposites, which effectively recognise the relative physical changes in colourimetric, plasmonic, and spectroscopic signals upon recognition of analytes. Several studies have explored these strategies for varieties of targets metabolites relevant for diseases such as neurotransmitters, hormones, and small molecules, which demonstrate the adaptability of AuNP across biomedical applications.

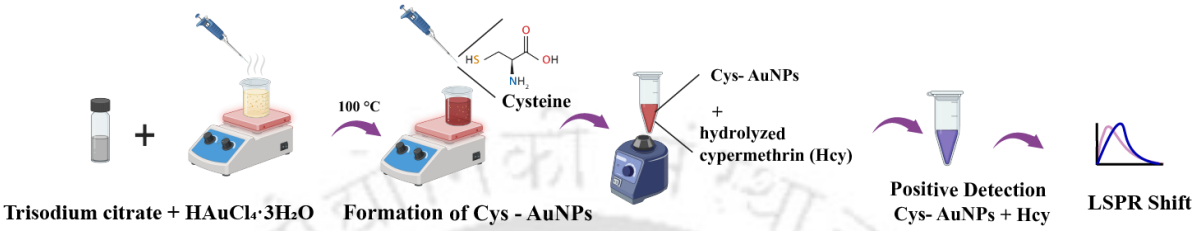

Figure 1.2: L-cysteine modified AuNPs showing LSPR redshift for cypermethrin sensing [22]

Rujiralai et al. demonstrated the use of L-cysteine functionalized AuNP for detecting cypermethrin – an insecticide which is a water pollutant and hazardous to health.[38] Their work highlights the advantage of conventional surface functionalization, in which AuNPs were synthesized using the Turkevich method (Fig. 1.2). The functionalization of AuNPs was achieved using L-Cys, in which the reaction mixture was stirred at room temperature. The authors reported the colloidal solution attained uniform dispersion, attributed to the electrostatic repulsion of AuNP@L-Cys carboxy terminals and with the observed particle size of 14 nm. The analyte cypermethrin was hydrolysed with alkali KOH solution and then vortexed with AuNP@L-Cys for the sensing reaction. The resulting redshift of the plasmonic peak from 525 nm to 634 nm, confirmed the presence of analyte with the limit of detection of 0.2 mg L^{-1}. In another work, Onifade et al.[39] have proposed an SPR sensor probe that integrates AuNP with graphene quantum dots (GQDs) for the detection of uric acid. The authors used self-assembled monolayers of (3-aminopropyl) triethoxysilane (APTES), which is a silane coupling agent and binds covalently with the glass substrate, providing attachment of AuNP-GQD stacking (Fig. 1.3). The Au films attained a thickness of 50 nm, confirmed through microscopy, and were deposited using a sputter coater. In this reaction scheme, the carboxyl groups of GQD act as binding sites for the amino group of uric acid. The binding kinetics were evaluated using the Langmuir adsorption isotherm model. The Kretschmann-configured plasmonic platform shows a lower limit of detection of 0.2 mg. L^{-1}, with noticeable reproducibility and repeatability.

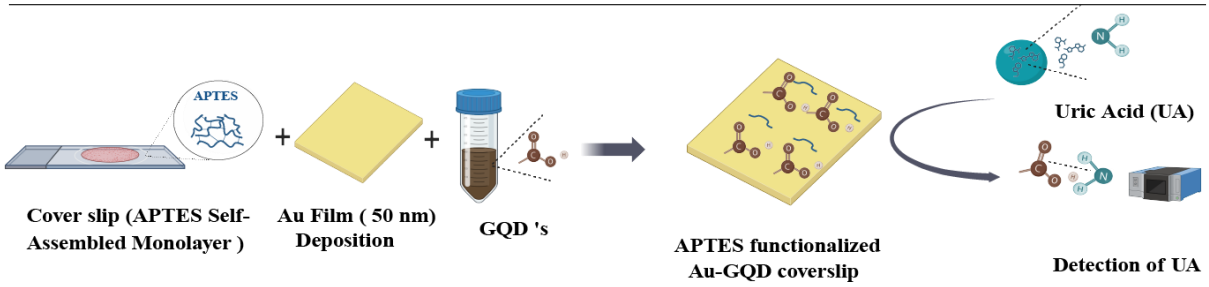

Figure 1.3: APTES–Au–GQD SPR platform for uric acid binding.[39]

Wang et al. reported the use of functionalized gold nanoparticles for the detection of serotonin in which the sensing mechanism was both colorimetry and SERS dual-mode.[40] The synthesized AuNP particle of 26 nm size was used for preparing two functionalized forms with dithiobis succinimidyl propionate (DSP-AuNP) and N-acetyl-L-cysteine (NALC-AuNP) The functionalization mechanism was mediated through their sulfhydryl groups. Both forms aid in double reaction, that is, the amino group of 5-HT with DSP via hydrogen bond and electrostatic interactions. Interestingly, the surface plasmon absorption peak of both functionalized forms was not significantly different, indicating the surface modification does not affect the SPR effect of AuNPs. The detection of 5-HT was confirmed with the redshift peak from 535 nm to 730 nm. This dual-mode system is advantageous, as it avoids interference with other biomolecules due to specific interaction and further results in high selectivity. The detection limit based on this liquid sensor was 0.15 nmol L^{-1}, and showed high accuracy with human serum for 5-HT detection. The sensing mechanism of DSP/NALC-functionalized AuNPs for serotonin detection is illustrated in Figure 1.4.

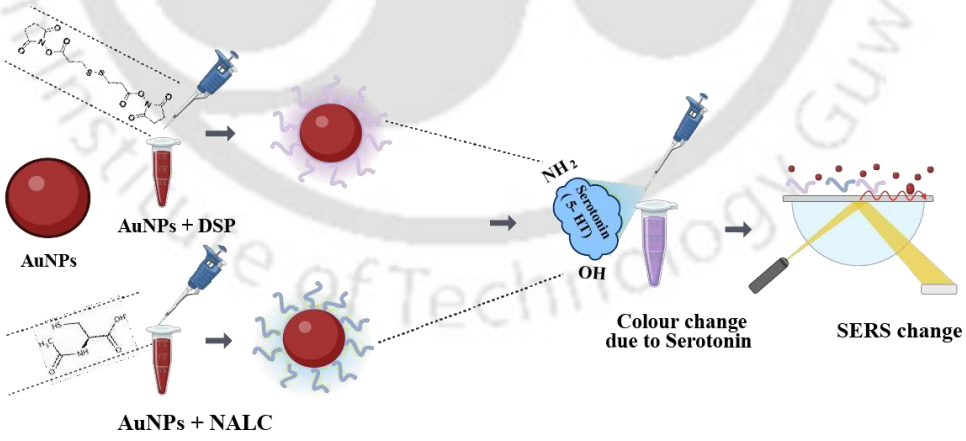

Figure 1.4: DSP/NALC-functionalized AuNPs enabling dual colorimetric–SERS detection of serotonin.[40]

In another work, Kim et. al have used AuNP for signal enhancement in competitive lateral flow immunoassay (LFI) for detection of cortisol.[41] Though it is a well-known approach which combines gold ions and reducing agents like hydroxylamine, hydroquinone,

and tartaric acid to form a layer around AuNP, resulting in upto 100-fold increase in the colorimetric signal (Fig. 1.5). The challenge being the reactiveness of the reducing agents, which have potential to bring non-specific signals. In their work, the authors have incorporated an internalized auto-enhancement complex, which is a gold ion pad, containing: (i) dried gold enhancement reagent on a cotton pad and (ii) buffer pad with hydrophobic material. This complex delays the rate of gold ion dissolution and separates the flow of AuNP conjugated anti-cortisol antibody. The AuNP of ca. 15 nm diameter was used for conjugation with the antibodies. Later, with the AuNP conjugates, the dried gold enhancement reagent flows through the strip, resulting in signal. The detection range of this method was effective with the reported LFI method, as the limit of detection is 3.8 pg mL^{-1} to 10 ng mL^{-1}, even with 10,000-fold fewer AuNP conjugates compared to competitive FLI.

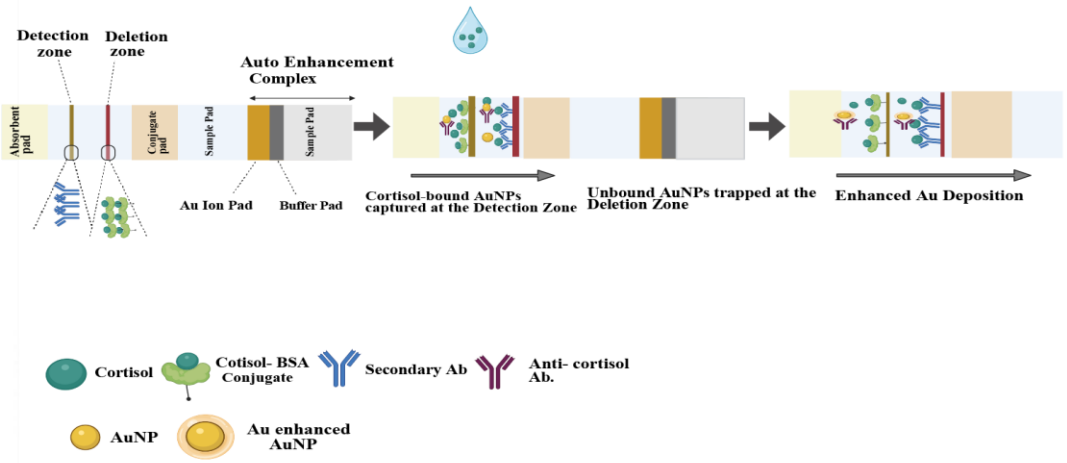

Figure 1.5: Auto-enhanced AuNP signal amplification in competitive LFI for cortisol [25]

1.3.2 AuNP conjugation with DNA probes for detection

The biomolecule DNA can either tether or wrap around AuNPs, offering high affinity for attachment of AuNPs.[42] This interfacial process enhances the colloidal stability and surface charge, while modulating the localized microenvironment which in turn moderates the signal readout. Engineering schemes have been developed to optimize the mechanism of DNA attachment to AuNPs and maintain their sensing performance in complex samples.[43] The conjugation method is widely achieved through a thiol-modified surface. However, other methods such as freeze thaws, chemical binders, and microwave assisted dry heating are also suitable for this purpose. It enables sensing with high specificity and selectivity for complementary DNA sequences, proteins, and specific biomolecules. Thus, it transforms them into a powerful tool for minimizing non-specific adsorption and translates the binding event into detectable optical or fluorescence changes even at ultra-low concentration of analytes.

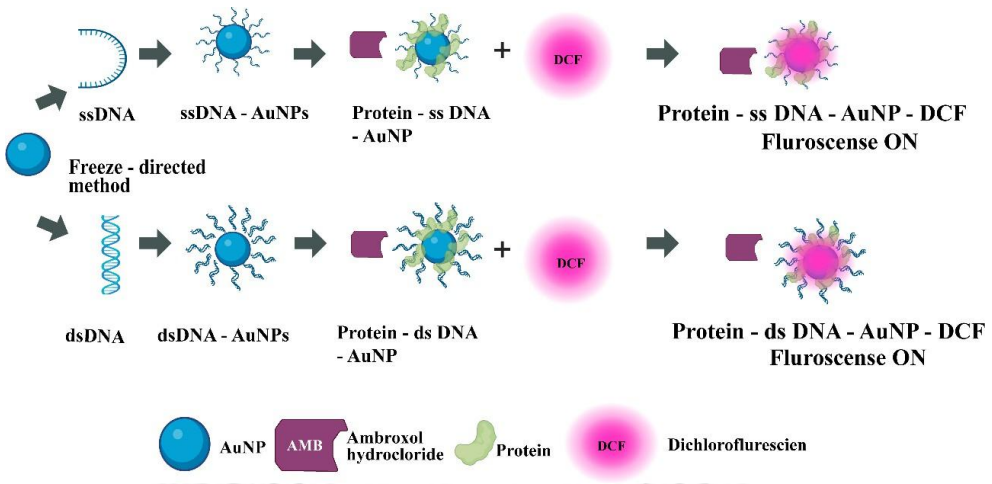

Figure 1.6: ssDNA- and dsDNA-coated AuNPs interacting with proteins to activate DCF fluorescence.[44]

Qin et al. have investigated the use of DNA strands for surface decoration of AuNPs with the objective of investigating the probe performance for detection of small molecules.[44] This strategy is relevant when the AuNPs are used for detection of metabolites in biological fluid, where non-specific interaction with biological macromolecules tends to form protein corona and reduces the overall detection efficiency. In their work, they used AuNPs having diameter of ca. 13 nm to conjugate with single-stranded (ss) DNA through denaturation and incubation (Fig. 1.6). Additionally, they also processed sulfhydryl-modified ss and double-stranded (ds) DNA with freeze-directed method to combined with incubation strategies to couple them with AuNPs. This approach results in a less negative zeta potential and a decrease in contact angle, indicating a reduction in electrostatic repulsion and a change in overall hydrophobicity. These probes are then linked with dichlorofluorescence (DCF) molecule and tested for detection of ambroxol hydrocholoride (AMB). The adsorption of DCF was more in dsDNA compared to ssDNA and led to quenching of fluorescence intensity. Interestingly, in the sample, AMB adsorbs competitively onto the surface of AuNP, thereby replacing DCF, resulting in increased fluorescence intensity and confirming the detection. The limit of detection (LoD) with DNA-AuNP-DCF in commercial milk samples was 14.23 nM, which was 2-fold compared to 35.82 nM with AuNP-DCF probes. Overall, this strategy is useful for reducing the impact of interfering molecules in AuNP probes-based detection.

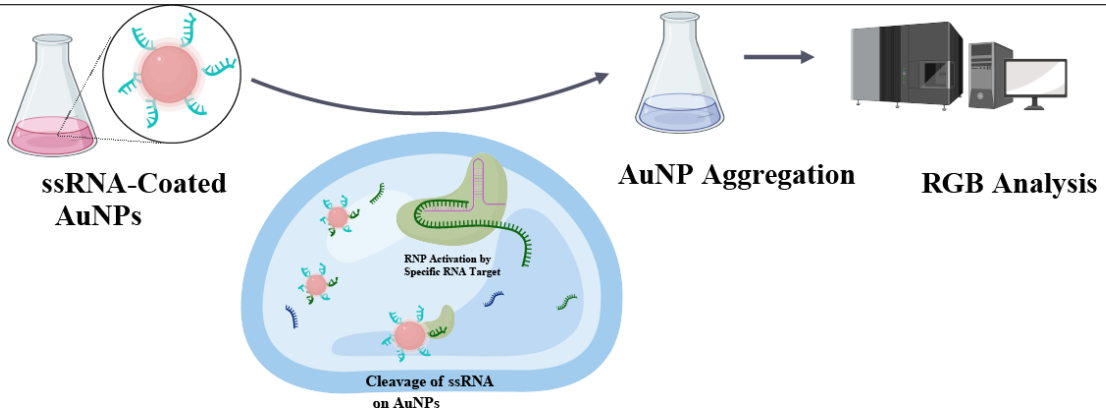

Figure 1.7: ssRNA–AuNP systems where target-induced RNA cleavage causes aggregation detected via RGB analysis.[45]

Another advancement in AuNP-based nucleic acid biosensor has been reported by Alarcón et al., which they refer to as the CRISPR-associated plasmonic colorimeter method.[45] In this approach, they combine AuNP aggregates with CRISPR RNA target recognition, specifically LwaCas13a, to facilitate colorimetric readout (Fig. 1.7). The typical size of AuNP used was 12 nm, functionalized with ssRNA. The hybrid composite remains in the colloidal dispersion state until a specific RNA target was present in the analyte sample. Once the ribonucleoprotein recognizes the target RNA, its nuclease activity is activated, leading to the cleavage of the ssRNA attached to the AuNP. This reaction triggers the aggregation of AuNP, which promotes plasmonic change, responsive for detection. The method shows LoD of 1 fM for RNA detection in biological samples as a specific application in diagnostics.

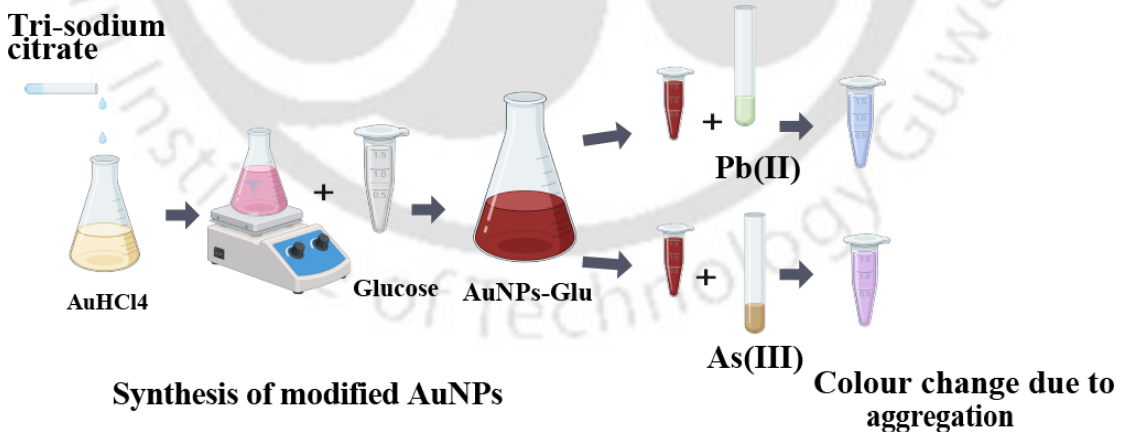

Figure 1.8: SPR shifts of AuNPs synthesized with different reducing agents along with stability changes of citrate–AuNPs over time.[46]

Ding et al. have investigated how surface chemistry and storage conditions affect DNA adsorption, stability, and sensing performance.[46] They employed Turkevich method to synthesize AuNPs using four different reducing agents, viz. citrate, glucose, ascorbate, and a

zwitterionic organic chemical buffering agent - HEPES. Notably, citrate and glucose-reduced AuNPs exhibited the highest level of DNA adsorption (Fig. 1.8). Among these, citrate-reduced AuNPs exhibited the most pronounced colorimetric response with an LSPR shift of 13 nm. On the contrary, HEPES-reduced AuNPs resulted in a broader particle size distribution, ranging from 6.5 nm to 43 nm, while ascorbate-reduced AuNPs have an average size of 41 nm. The colorimetric change observed in HEPES–reduced AuNPs was more substantial than other reducing agents used in this study. Each of the AuNPs exhibited stronger SPR peaks, measuring at 520 nm, 526 nm, 530 nm were for citrate-, ascorbate-, and HEPES-AuNPs, respectively. The authors also optimize the NaCl concentration to evaluate colloidal stability, identifying 32 mN NaCl as the critical transition point. The findings of this work also indicate that the choice of surface ligand is crucial for modulating sensor performance. In principle, only intermediary binding affinity of surface ligands offer critical optical signaling. In this context, only citrate provides an intermediate affinity, which is optimal under the tested conditions. However, a critical finding of this work also suggests that the storage of citrate leads to a loss, both for colloidal stability and DNA adsorption capacity.

1.3.3 Integration of AuNPs with wearable sensors

Wearable and flexible sensors with integrated AuNP can be considered as another step closure to the laboratory measurement and its translational application for real-time monitoring of analytes. With the combination of optical and electrical properties of AuNPs, researchers have integrated them with elastomeric substrate, hydrogels, and microfluidics that can be conforming with dynamic physiological or environmental system while maintain a stable signal readout. Such platforms are reported to enable on-skin biochemical analysis, motion tracking, and strain analysis. Thus, these examples suggest that AuNP can be considered a soft sensor component for personalized and precision applications.

A wearable SERS-based sensor developed by Ye et al. was reported to transform sweat detection, featuring a microfluidic channel.[47] In this design, the channels were modified using a PDMS and AuNPs superlattice film. The reducing agent used to synthesize AuNPs is a mixture of oleylamine and n-hexane. The resulting high quality AuNPs is a large continuous superlattice film with monodispersed and uniformly sized AuNP of 6.3 nm. For testing the sensing performance, the system was attached to skin using medical adhesive tape. A hydrogel modified with cobalt (II) chloride was used to measure sweat along with pH values and SERS signals. The LoD pertains to be 5 mM, indicating the robustness of the design for real-time diagnostics of hydration and lactate levels.

In another study by Huang et al., a flexible stain sensor was developed using AuNPs

with a size of 25 nm.[48] These nanoparticles were linked through tetra (ethylene glycol) dithiol (SH – TEG- SH) linkers, which facilitate the formation of covalent bonds. The role of AuNPs is to act as a conducting material within the hybrid strain sensor. The AuNPs were synthesized by seeded growth method (Fig. 1.1), allowing precise tuning of its conductive property and adaptability with the substrate, as an application in flexible electronics.

In the same line, Ramesh et. al, have developed AuNP-based humidity sensors that are integral to smart irrigation schemes.[49] The designed system enhances agriculture through automation of water scheduling and minimizing water wastage. The authors have used the classical Turkevich method to synthesize AuNPs ranging from 10 – 15 nm. These nanoparticles were deposited on Kapton (polymide film) substrate, integrated with silver electrodes to create the sensor. The sensor is multipurposed in nature, which functions for humidity detection and detects breathing patterns when attached to a 3D printed mask to distinguish between normal, deep, and fast breathing patterns. Furthermore, the sensor can also detect moisture from fingers, which offers a prospect of extending its application in diagnostics.

1.3.4 Detection of pathogen using AuNPs-based probe design

AuNP-based colorimetric assays also offer suitable platform design for translating the pathogen binding events into optical signals for sensing. Using unique approaches to decorating AuNPs with biological recognition elements such as antibodies, bacteriophages, and small-molecule ligands, the nanoscale interaction can be translated into notable shifts in plasmonic peak position. This enables the researchers to track the presence of target microbes based on visual color change. Interestingly, the nanomaterial design helps track the subtle changes in particle spacing, surface chemistry, and aggregation pattern for tracking the concentration of pathogen and generating distinct optical responses. Thus, these platforms offer rapid and crucial point-of-care technology useful for infection diagnostics.

In a study by Oh et al, the researchers successfully utilized AuNP to detect SARS-CoV-2 nucleocapsid proteins.[50] The approach involves combining streptavidin-coated AuNP cores with the biotin-antibody-coated AuNP satellites. The binding of these particles maintains a critical size separation of approximately 15 nm, which is estimated for the combined size of antibody and streptavidin. The engineered nanoparticle effectively prevents strong plasmon coupling and enhances detection sensitivity. In the synthesis procedure, the authors have employed melamine to induce a gap size of < 2 nm. The AuNP cores, which displayed a surface plasmon resonance peak in the range of 529 nm for bare particles (size 40 nm), while for the final clusters (particle size in cluster was either 40–40 nm or 40–15 nm), the peak shifted to 532 nm. Both sized AuNPs have been used for preparing streptavidin-loaded AuNPs and a

bioinylated AuNPs. After adding antibodies, the colorimetric shift was observed from red to pale purple. The resulting LoD was 0.038 ng mL^{-1} and a detection range spanning from 300 pg mL^{-1} to 1,000 ng mL^{-1}, which were comparable to the commercially available COVID-19 test kits.

In another study by Olszewska et al, bacteriophages - viruses that infect bacteria, were employed to develop a method for pathogen detection.[51] The target microbes include *Pseudomonas aeruginosa*, *Vibrio cholerae*, or *E. coli*. Herein, the bacteriophages were modified with thiol groups, which enables them to aggregate the AuNPs upon interaction with samples containing the target bacteria. The reaction results in a notable colorimetric change from red to purple colour, which is indicative of the detection sensitivity. The AuNPs are synthesized using the seed-mediated method, yielding four distinct sizes 7 nm, 20 nm, 50 nm and 85 nm. The LoD of this system ranges from 100 to 102 CFU, indicating high efficacy and precision. Alongside the colorimetric shift, a significant redshift was also recorded in SPR peaks, which establishes a new benchmark for pathogen detection.

Similarly, Sekar et al, have modified the AuNPs with glucose, which act as a targeting molecule for detection of bacteria.[52] The approach demonstrated that the interaction between glucose functionalized AuNPs and bacteria leads to either aggregation or repulsion, resulting in significant shift in the SPR peaks. A redshift in this context is indicative of aggregation, while a blue shift signifies repulsion. Since the glucose molecules have hydroxyl groups, it tends to bind with the cis-diols of the peptidoglycan present in the bacterial cell walls, facilitating targeted detection. For AuNPs synthesis, a green method was used, using the plant extracts from *Physalis minima*. The SPR for these nanoparticles was initially measured at 546 nm, with an average particle size of 36 nm. Following the functionalization with glucose, the SPR shifted to 552 nm. Notably, as the concentration of *E. coli* increased, a significant blue shifted SPR peak at 539 nm was observed along with notable color change from light brown to bluish pink, indicating the capability of bacterial detection.

Sahar et al, have also reported a sensor fabricated for detection of Streptococcus pyogenes M1 serotype (M1-GAS), which is a causative organism for pharyngitis (sore throat).[53] The effectiveness of this sensor is attributed to the use of AuNPs that were modified with the H-1 antigen, a bacterial surface protein which binds with sugar moiety and lectin. The LoD of the sensor was achieved at 1.5×10^2 $CFU.mL^{-1}$, with a detection time of 20 minutes. The AuNPs are synthesized using the traditional Turkevich method, exhibiting standard SPR of 520 nm., aligning well with average particle size of 20 nm. The study observed redshifts ranging from 14 to 56 nm for the M1-GAS concentrations range of 1×10^3 to 10^6 $CFU.mL^{-1}$.

Such engineered technology can thus be useful as a point-of-care diagnostic. An account of various AuNP particle sizes along with biorecognition, nanocomposites employed and corresponding LoD for sensing studies are in **Table 1**. However, despite extensive work on AuNP biosensors, systematic understanding of linker-controlled surface chemistry remains limited.

Table 1: Account of AuNP-based sensors with corresponding biorecognition elements, nanocomposites, and Limit of Detection (LoD).

AuNP size	Analyte	Biorecognition/ Nanocomposite	LoD	Reference
14 nm	Cypermethrin (insecticide)	L-Cysteine functionalized AuNP	0.2 mg L−1	[38]
~50 nm (Au film)	Uric acid	AuNP + Graphene quantum dots (GQD)	0.2 mg/dL	[39]
13 nm	Ambroxol hydrochloride (AMB)	DNA-AuNP (ssDNA/dsDNA)	14.23 nM (in milk)	[44]
12 nm	RNA target	AuNP + CRISPR (LwaCas13a + ssRNA)	1 fM	[45]
6.3 nm	Sweat metabolites	AuNP superlattice film + PDMS + hydrogel	5 mM	[47]
25 nm	Strain (mechanical stress)	AuNP connected with TEG dithiol linkers	GF≈126	[48]
16 nm, 25 nm, 40 nm	Histamine	AuNP + cation-selective polymer	0.72 µM	[54]
15–20 nm	Norovirus	AuNP+ SMV25 aptamer	9.65 ng/µL	[55]
15 nm	SARS-CoV-2	Strp-AuNP+Ab-satelite	0.038 ng mL−1	[50]
7, 20, 50, 85 nm	Bacteria	Phage-induced AuNP aggregation	100 – 102 CFU	[56]

1.4 Fundamental mechanism of amino-acid attachment to AuNPs

Within the context of modern diagnostics and sensor application, protein-coated

AuNPs are at the core. However, these engineering solutions are critically dependent on the basic science through which the proteins are anchored to the metal surface. This reflects a balance between electrostatic interaction, hydrophobic forces, coordination bond, and covalent bonding that locks the key residues with AuNPs while preserving their biochemical activity (Fig. 1.9).[57] The subtle variation in amino acid composition, protein orientation, and local surface chemistry of biomacromolecules are key for stable and nearly covalent attachment [42]. This, however, is more crucial for achieving colloidal stability, controlling aggregation, signal reliability, and stability of the nano-bio interfacial processes.

Cysteine is considered as the most effective amino acid for protein attachment to AuNPs through the formation of a covalent Au-S bond. This thiol group attachment undergoes a three-step attachment process, which begins with physisorption, followed by chemisorption involving electron transfer and concludes with formation of a stable Au-thiolate covalent bond.[58] Interestingly, it has been established that the binding energy of for Cys-Au interactions is 1.5-2 times greater than that of other covalent interactions. A remarkable property of Cys is its ability to form a hard corona, which makes the amino acid a critical component for bioconjugates. In this context, Cys plays critical role in irreversible adsorption, as reported through its interaction with IgG antibodies.[59] It demonstrates the highest affinity for citrate-AuNPs, among all 20 natural acids, as reflected through the Gibbs free energy value of 5.69. This affinity is attributed to the strong Au-S bond, which has a binding energy 3.5 times greater than Lys or His amino acids.[60] Furthermore, the strength of Au-thiol interaction has been established in the range of 40–50 kcal mol^{-1}, comparable to that of covalent bonds.[59]

Tryptophan with its indole ring structure, has potential to adsorb onto gold surface in a stacking orientation.[61] This interaction mode utilizes the delocalized π electrons clouds, while the -COOH and $-NH_2$ groups provide additional binding affinity through salt bridges with Au. Furthermore, Ozaki have established that the reducing ability of protein during AuNP synthesis is proportional to the number of Trp residues, as it enhances the predominance of nucleation reactions, resulting in increased yield.[62]

Tyrosine has exceptional ability to facilitate molecular assembly through both non-covalent interactions and covalent crosslinking. As emphasized by Kima and Min, Tyr plays critical role in reduction of Au^{3+} and subsequent initiation of nanoparticle formation.[63] As per the suggested mechanism, Tyr transfers an electron to Au^{3+} or $AuCl_4^-$ and reduce them to neutral atom (Au^0). These atoms further nucleate and form AuNPs. The process is referred as green synthesis, as it uses biocompatible amino acid, in which the phenolic hydroxyl group

chelates Au^{3+} ions and help reduce them to Au^0, thus serving dual role in chemical transformation and nucleation. Additionally, Tyr also serves as a protective corona layer in which the -COOH and -NH_2 groups provides steric and electrostatic stabilization.[64]

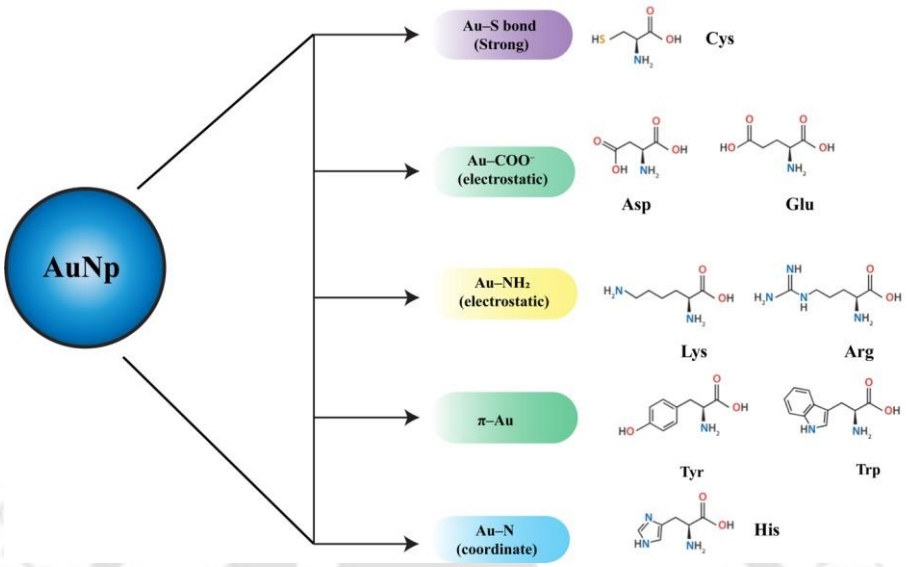

Figure 1.9: Schematic showing the major interaction modes between amino-acid residues and AuNPs: Au–S, Au–COO^-, Au–NH_2, π–Au, and Au–N coordination

Glycine exists as a zwitterion in aqueous environment which can readily adsorbed onto AuNP through electrostatic and coordination interaction. It has been reported that the neutral glycine has potential to bind Au3 the amine groups,[65] however, the size of gold cluster has negligible impact on the interaction vibrational peaks.[66] However, Vesga et al. have reported that glycine promotes aggregation which can increase the strength of surface-enhanced Raman signal.[67]

Likewise, Aspartate and glutamate interact with the gold surface through their -COOH groups, yet it shows minimal binding. These amino acids with negative charges exhibit a near flat pattern in UV-vis spectra indicating weak binding and surface interaction compared to aromatic and positively charged amino acids.[68] Based on the study by Buglak and Kononov, it was concluded that Binding of gold ions with negatively charged amino acids (aspartate and glutamate) is significantly weaker than with cysteine, tyrosine, and histidine.[69]

1.4.1 Amino-acid contributions to protein orientation on AuNPs

Antibody-Au interactions are fundamentally driven by the ionizable amino acid residue present on the protein surface.[70] These residues become protonated below pH 7.5, while the citrate-capped AuNPs have a negative charge, which in the presence of clusters of basic amino acid like Lys/His residue generate electrostatic attraction. This leads to aggregation of AuNPs and a change in LSPR. Further, the self-assembly process helps in the

formation of protein-gold nanoclusters. Notably, at low pH, the high concentration of protonate Lys and His, generates a positive charge to neutralise the deprotonated citrate groups. As a result, it eliminates the electrostatic repulsion, stabilizes the colloidal suspension, and predominates the vdW forces to cause aggregation.[59]

In the work of Xu et al, the focus was on critical process of direct adsorption and role of each amino acid in maintaining orientation during the binding of protein on AuNPs.[60] They elucidated that aliphatic amino acids like Gly and Ala have effective binding efficiency due to reduced steric hindrance compared to the amino acids with bulkier side chains. This enhances their ability to maximize contact with the nanoparticle surface.

Li et. al, prepared certain class of AuNP-based artificial antibodies (Goldbody), by engineering peptide (Pep1), derived from an antibody CDR.[71] This peptide includes Cys residues at both ends, allowing for dual Au–S bonding to anchor with nanoparticle surface while restoring its native conformation. This thiol-specific conjugation preserves the active state of the protein. Their work highlights that peptides or polyethylene glycol (PEG) chains which lack cysteine lacks specificity, highlighting that Cys is the critical for achieving stable orientation in functional bioconjugates. As Raman spectroscopy is a versatile tool for probing disulfide bonds (S-S), notable orientation of Cys interactions on AuNP surface impact the overall dynamics and results in variation in wavenumbers for characterization. Often these interactions exhibit bidentate anchoring, which often induces a strained conformation to the S-S linkage.[72] This information is crucial especially when studying the interaction mechanism of AuNPs with proteins via Cys-based linkage.

1.5 Thiol-Based Linker Chemistry at the AuNP Interface

As discussed previously, thiol–Au linkers are widely used for biomolecule immobilization due to the strong affinity of the –SH group for gold surfaces. When cysteine residues are positioned away from the active site, this mode of attachment can preserve protein orientation and catalytic activity. Extending this concept, bifunctional thiol-containing crosslinkers such as dithiobis(succinimidyl propionate) (DSP) and its sulfonated analogue 3,3′-dithiobis(sulfosuccinimidyl propionate) (DTSSP) are commonly employed to couple gold anchoring with selective amine-reactive chemistry for controlled surface functionalization.[73,74]

1.5.1 Oriented protein conjugation via site specific linkers

Bare AuNPs attach onto proteins indiscriminately, which creates non-specific attachments. This effect arises due to the multivalent nature, from electrostatic to covalent thiol

bonding. Such functionalization is a challenge for achieving precise sensing because the AuNPs can bury the active sites or destabilize the overall conjugated system. The smart approach of surface engineering overcomes this challenge by introducing targeted linkers, such as thiol-PEG, 1-ethyl-3-(3-dimethylaminopropyl) carbodiimide (EDC) and N-hydroxysuccinimide (NHS) coupling chemistry, or acrylate modifications. These linkers selectively target the protein via Cys, Lys, or His residues while spacing themselves appropriately to retain the functional site available.[75,76] Henceforth, these approaches lock the oriented binding without affecting the activity and result in reproducible bioconjugates for diagnostic applications.

Thiol-Au linkers is one of the most common linker approaches, in which the -SH group attaches strongly through the cysteine residues of the protein.[77] In some cases, where the position of Cys residue is far from the active site, the orientation is generally preserved. This allows the bioconjugate to maintain strong activity. This has been highlighted in the work by Gao et al., as the bioconjugate's activity was found significantly decreased, when the Cys residue is situated near the active site.[78] Furthermore, in another work by Okyem et al, the anti-horseradish peroxidase IgG antibody was modified with N-succinimidyl acrylate to modify the lysine residues.[59] The work also demonstrated that as pH decreases the positive charge increases, resulting in change in protonation state of the imidazole on His residue. This modulation fine tunes the protein charge within the range of pH 6.0 – 8.0, Lys residue remains protonated. Likewise, EDC/NHS linker is another common linking strategy used in context with AuNP-functionalized probes. EDC activates the carboxyl group on AuNPs with NHS stabilizing this activation and facilitating the coupling reaction with Lys. Moreover, the PEG linkers, possessing a thiol end that bond to the AuNP surface, demonstrates dual-action capability. It allows to bind with His, Cys, and other residues.[79] Similarly, Malemide-SH linkers react only with Cys (-SH) group, thereby providing a targeted approach.[80]

Localized surface plasmon resonance (LSPR) is a collective oscillation of conduction band electrons in metallic nanoparticles driven by incident electromagnetic radiation. When the frequency of the incoming light matches the natural frequency of these electron oscillations, strong resonant absorption and scattering occur, manifesting as intense and size-, shape-, and environment-dependent optical bands.[81,82] Gold nanoparticles (AuNPs) have become prototypical LSPR platforms due to their biocompatibility, chemical stability, and straightforward synthesis with well-controlled sizes and shapes. The LSPR band of spherical AuNPs in the visible region is highly sensitive to changes in the local refractive index,

interparticle spacing, and surface chemistry, making them excellent transducers for biosensing. [81,83,84]

In colorimetric biosensing formats, the aggregation of AuNPs, or changes in their local dielectric environment upon analyte binding, leads to distinct spectral shifts and visible color changes that can be detected by simple spectrophotometry or even by the naked eye. This label-free optical response has been widely harnessed for the detection of proteins, nucleic acids, small molecules, and ions. The ability to integrate AuNPs into surface plasmon resonance (SPR) configurations further enhances sensitivity, where AuNPs act as amplifying elements on planar plasmonic substrates.[85] For oxidative stress biomarker detection, including allantoin, AuNP-based platforms offer the possibility of coupling enzymatic reactions or affinity binding events to plasmonic readouts, enabling rapid, miniaturizable, and potentially point-of-care assays.[86,87]

Fundamental to the performance of AuNP biosensors is the surface functionalization strategy used to immobilize recognition elements such as enzymes, antibodies, or synthetic receptors. The Au–S bond between gold and thiolated ligands provides a versatile and robust anchor for constructing self-assembled monolayers (SAMs) and crosslinked architectures on nanoparticle surfaces. The choice of linker molecules, their functional groups, spacer length, and hydrophilicity directly affect colloidal stability, surface coverage, and analyte accessibility. Mixed self-assembled monolayers and bifunctional linkers have been extensively explored to optimize orientation, density, and bioactivity of immobilized biomolecules. In addition, adsorption of proteins and polymers onto AuNPs frequently follows characteristic isotherms whose parameters reflect the affinity, capacity, and cooperativity of binding, thereby influencing sensor response, dynamic range, and reproducibility.

For enzymatic sensing of allantoin using allantoinase, AuNPs can serve as either dispersed colorimetric reporters or as nanostructured interfaces in SPR setups, providing enhanced optical sensitivity compared to flat metal films alone. To exploit these advantages, it is crucial to engineer the AuNP surface such that the enzyme is stably attached, correctly oriented, and retains its catalytic properties, while the underlying plasmonic response remains tunable and reproducible. These requirements, in turn, place stringent demands on the linker chemistry and on a quantitative understanding of linker adsorption and organization on the AuNP surface.

Dithiobis(succinimidyl propionate) (DSP) and its sulfonated analogue 3,3′-dithiobis(sulfosuccinimidyl propionate) (DTSSP) are homobifunctional, thiol-containing

crosslinkers widely used in bioconjugation and surface immobilization. Both molecules comprise an internal disulfide spacer flanked by N-hydroxysuccinimide (NHS or sulfo-NHS) ester groups at each terminus. The disulfide moiety, reduced or chemisorbed, provides a strong anchoring point to gold via Au–S bonds, while the NHS esters react selectively with primary amines on proteins and other biomolecules at near-neutral pH to form stable amide linkages. In the context of AuNP functionalization, DSP is soluble in organic solvents such as dimethyl sulfoxide (DMSO) and is often used to introduce amine-reactive groups on gold electrodes and nanoparticle surfaces, whereas DTSSP, bearing sulfonate substituents, is water-soluble and membrane-impermeable, enabling aqueous-phase and extracellular crosslinking. [88,89]

The structural differences between DSP and DTSSP give rise to distinct solubility, adsorption, and aggregation behaviors when used to modify AuNPs. DSP's hydrophobic character and limited aqueous solubility typically require organic cosolvents, which can influence nanoparticle stability and protein conformation during functionalization. DTSSP, by contrast, is intrinsically hydrophilic due to its sulfonate groups, favoring electrostatic repulsion between modified particles and thereby potentially improving colloidal stability in physiological buffers.[90,91] At the same time, the presence of charged groups may alter the packing density and orientation of the linker on the gold surface, as well as the accessibility and reactivity of the NHS esters toward amine-containing ligands. These differences can manifest in the extent of AuNP aggregation, surface charge (zeta potential), and changes in LSPR band position and width, all of which are critical for reproducible plasmonic sensing.

Thiol–gold chemistry is central to the formation of ordered linker layers and their subsequent interaction with biomolecules. The chemisorption of thiolated linkers on gold involves the formation of strong Au–S bonds and, depending on the linker structure and surface conditions, can lead to densely packed monolayers or more heterogeneous, patchy arrangements.[92,93] The balance between Au–S binding, ligand–ligand interactions, and solvation effects governs surface coverage, orientation, and mobility. Experimental studies, often interpreted using adsorption isotherm models, provide macroscopic parameters such as maximum surface coverage and binding constants that reflect underlying molecular-scale processes. For AuNPs, where curvature and finite size further complicate packing, adsorption isotherms become a powerful tool to quantify the interaction of DTSSP and DSP with the nanoparticle surface and to relate surface coverage to optical response and colloidal stability.

In addition to their anchoring function, the NHS (or sulfo-NHS) ester termini of DSP and DTSSP provide reactive handles for covalent attachment of proteins such as allantoinase,

as well as stabilizing polymers or blocking agents. The reactivity and hydrolytic stability of these esters determine the efficiency of bioconjugation and the resultant density of active enzyme on the AuNP surface. Differences in linker hydrophilicity, steric hindrance, and surface packing can thus influence not only the initial adsorption and aggregation behavior of the AuNPs but also the distribution, orientation, and activity of immobilised biomolecules. Despite widespread practical use of DSP and DTSSP in biosensor construction, systematic comparative studies that correlate their adsorption thermodynamics, surface organization, and plasmonic behavior with biosensing performance remain limited.

1.5.2 Relevance of Adsorption Isotherms in Linker–AuNP Interactions

The adsorption of linkers, proteins, and other ligands onto AuNP surfaces is frequently analyzed using isotherm models such as Langmuir, Hill-modified Langmuir, Freundlich, or Temkin isotherms. These models provide quantitative descriptors of surface binding, including the maximum surface coverage, affinity constants, and potential cooperativity among adsorbed species. For example, Ruiz et al. systematically investigated the adsorption of antibodies onto citrate-stabilized AuNPs across different pH conditions using nanoparticle tracking analysis and fitted the data to a Hill-modified Langmuir equation to extract binding constants and layer thickness.[94] Such analyses reveal how environmental factors and surface charge influence monolayer formation and the functional orientation of biomolecules, directly impacting biosensor sensitivity and specificity.

In the context of DSP and DTSSP modification, adsorption isotherms can be used to compare the binding energetics and saturation coverage of the two linkers on AuNP surfaces. Deviations from ideal Langmuir behavior may indicate heterogeneous binding sites, multilayer formation, or linker–linker interactions that promote aggregation or clustering. Moreover, correlating isotherm parameters with LSPR shifts and colloidal stability provides insight into how molecular-scale adsorption translates into macroscopic optical behavior. This is particularly relevant for colorimetric sensing, where controlled aggregation or subtle interparticle distance changes underpin signal generation. A rigorous isotherm-based characterization of DTSSP and DSP adsorption thus offers a quantitative framework for rationally selecting and optimizing linker chemistry in plasmonic biosensors.

To evaluate linker adsorption over a broad concentration range, gold nanoparticles were incubated with varying concentrations of DSP and DTSSP. A calibration curve was used to quantify the amount of unbound linker, allowing calculation of the number of linker molecules adsorbed per nanoparticle at equilibrium. From these values, adsorption capacity

and apparent binding constants were determined.

1.6 Need for Computational Modeling

While experimental techniques such as UV–vis spectroscopy, dynamic light scattering, zeta potential analysis, and electron microscopy offer valuable information on AuNP functionalization and aggregation, they provide limited direct insight into the molecular-level organization, dynamics, and energetics of linkers and biomolecules at the metal interface. Many key questions such as how DTSSP and DSP arrange themselves on curved AuNP surfaces, how mobile they remain once adsorbed, how solvation and counterions influence their conformations, and how these factors collectively affect colloidal stability and protein binding, are challenging to address experimentally with high spatial and temporal resolution. As a result, mechanistic interpretations of adsorption isotherms and plasmonic responses often rely on simplified assumptions about surface coverage and orientation.

Molecular dynamics (MD) simulations have emerged as a powerful tool to complement experiments by providing atomistic or coarse-grained descriptions of ligand-functionalized AuNPs in explicit solvent. Several studies have used MD to investigate the solvation, structure, and thermodynamics of thiolated AuNPs, revealing how surface coverage, ligand chain length, and terminal functional groups influence ligand shell anisotropy, solvent penetration, and interparticle interactions. For instance, Yadav and Chakravarty examined thiolated AuNP solvation in near-critical fluids and showed that density and temperature modulate the anisotropy of the ligand corona and the Helmholtz free energy of solvation. Similarly, Cetin and co-workers demonstrated that the aggregation behavior of functionalized AuNPs in toluene strongly depends on the polarity of terminal ligand groups, affecting interparticle distances, radial distribution functions, and hydrogen bonding networks.

MD simulations have also been successfully applied to probe biomolecular adsorption onto AuNPs, including the formation of protein coronas and competitive binding of multiple proteins on citrate-capped particles.[95] These multiscale approaches provided detailed information on recognition processes, adsorption modes, and structural preservation or rearrangement of proteins, offering explanations for sometimes conflicting experimental observations. Importantly, simulations can directly quantify binding energetics, surface diffusion, and conformational ensembles that are difficult to access experimentally. Integrating such computational insights with experimental data enables more accurate mechanistic models of nanoparticle functionalization, stability, and biosensing performance.

For the specific case of DSP and DTSSP on AuNPs, computational modeling can elucidate how the introduction of sulfonate groups, variations in hydrophilicity, and differences in charge distribution influence the adsorption geometry, surface packing, and mobility of the linkers. Moreover, simulations can probe how linker coverage affects the local dielectric environment and interparticle potential of mean force, thereby providing a microscopic basis for understanding experimentally observed differences in colloidal stability, aggregation propensity, and LSPR shifts between DSP- and DTSSP-modified AuNPs. In addition, modeling can help rationalize how linker organization modulates the accessibility and orientation of immobilized enzymes such as allantoinase, ultimately affecting catalytic efficiency in biosensing configurations.

Molecular computation for AuNPs has proved to be a valuable tool for obtaining atomistic information relevant to the structure, dynamics, and reaction mechanism. Furthermore, these tools are indispensable to assign and understand the spectroscopic results, including UV-vis, Raman, and FT-IR. CHARMM-GUI's nanomaterial modeler in this context have emerged as a bridge between experimental design and modelling its *in-silico* counterpart.[96] The transformative algorithm face-centered cubic (fcc) metals, including gold atoms.[97] Furthermore, the offer for not only building the starting atomistic coordinates for simulation but include interoperability among available standard simulation engines including Charmm, Gromacs, NAMD, and AMBER.[98] Especially for modelling of AuNP, the implementation of 'interface force-field' (IFF) in CHARMM-GUI which provides straightforward atomistic description of AuNPs. Furthermore, it validated lattice constant and surface energy, which are more accurate than DFT-level accuracy, in context of remaining close to the experimental values. Notably, IFF parameters are based on Wulff construction method for equilibrated nanoparticle shapes.[97] Kariuki et al. to AuNP in a 10 × 10 × 10 nm box along with the capping agent citrate and neutralizing counter ions.[99] Another major advantage of CHARMM-GUI is that they provide options for creating appropriate Miller indices such as low-energy [111] and intermediate-energy [100] facets which corresponds to the characteristic truncated octahedral AuNPs commonly observed experimentally.[100] Henceforth, the interface is ideal to create comparable facet-dependent adsorption or protein binding. Kaumbekova et al. employed CHARMM-GUI to construct face-centered cubic structures of Au nanospheres varying from 1 nm to 5 nm and performed all-atom MD simulations using Amber99SB force field for bovine serum albumin (BSA).[101] They discovered that Au nanoparticles and NaCl synergistically induce conformational changes in BSA. In the model containing 5 nm Au nanoparticles, it enhances helices and protein folding

in presence of salt; while 1 nm Au nanoclusters destabilize BSA structure. This computational modeling provided critical insights into size-dependent protein corona formation. Baruah et al. utilized CHARMM-GUI Nanomaterial Modeler to construct 4 nm spherical AuNPs and functionalized them with polyphenols derived from turmeric and curcumin.[102] The authors generated the starting structural model for simulation and using the interoperable file system, the coordinates were processed in GROMACS for calculating the simulation trajectory.

Other studies using innovative approach for AuNP modelling including embedded-atom model and machine learning potential for computational modelling of AuNPs. For example, a study by Zeni et al. employed machine learning force fields (ML-FFs) coupled with molecular dynamics to investigate size-dependent melting of AuNP containing 147 to 6,266 atoms.[103] Their valuable findings revealed that melting initiates preferentially at low-coordinated atoms on vertices and edges, then propagates to atoms on [100] and [111] facets before finally extending to the nanoparticle interior. This data-driven characterization using unsupervised learning revealed that thermodynamic stability varies systematically with nanoparticle size. Recently, they also developed an efficient and interpretable machine learning force field for AuNPs, which uses DFT based data.[104] Their benchmarking on the melting temperature of AuNPs are in-line with experimental data, which suggest that such data driven thermodynamic properties can be predicted with good accuracy.

In another work, Li et al. employed all-atom polarizable approach for MD simulations of AuNP in aqueous electrolyte solutions with varying ionic compositions.[105] The study implemented a core-shell model for Au atoms to account for surface polarization effects. This approach captured information relevant to facet-dependent polarization, hydration energy, and ion adsorption dynamics revealing that Au [100] facets exhibit greater polarizability than Au [111] facets. The study also highlights that 'image charge effects' are significant near the cluster surfaces.

These computational strategies employing CHARMM-GUI and other customized algorithms have established quantitative framework for strategic modelling of AuNPs with engineered properties suitable for biomedical applications. Furthermore, with the integration of machine learning force fields and advanced sampling methods with CHARMM-GUI, the capabilities to predict complex dynamic behaviour can be advances. Henceforth, such innovative approach in future can accelerate computational predictions for advancing clinically validated nanotherapeutics.

1.6.1 Model preparation strategies for AuNPs using CHARMM-GUI

CHARMM-GUI's Nanomaterial Modeler offers a visual and controllable method for building AuNPs with specific shapes, sizes, and surface facets. This workflow details various AuNP model classes with illustrations corresponding to different strategies, including sprehere-like nanoparticles, cylinders, rods, boxes, polygons, and Wulff-based polyhedral which are predominantly [111], [100], and [110] surfaces.

Simple geometric particles and slabs of AuNP with dimensions in the order of 5–10 Å, which are often modelled to probe local structure and interface chemistry at a minimal computational cost. In CHARMM-GUI, these are constructed by choosing gold as an fcc metal, specifying the target size along X, Y, and Z coordinates, and choosing a shape. Note that the builder internally works from an oriented fcc unit cell for Au, and thus for a shape such as "sphere" in Fig. 1.10 (a), it corresponds to a cluster-cut from a crystalline lattice and wrapped in a smooth envelope. Such nearly spherical particles are frequently used as generic models for ultrasmall AuNPs where curvature dominates over explicit facet expression. A similar strategy has been employed as starting points in MD simulations by Kariuki et al. where they have used citrate-capped and ligand-protected ultrasmall gold particles.[99] In Fig. 1.10 B–E, a gradual transition from compact clusters to extended slabs and cubic particles has been illustrated by changing the box dimensions and periodicity. These geometrical setups, the periodicity needs to be called in X and Y direction while keeping Z non-periodic. The corresponding thickness is ~5 Å and the lateral dimensions are ~10 Å. These compact slabs are ideal to compute surface energies, adsorption geometries, and short-time diffusion of adsorbates on Au. Conversely, using equal dimensions (e.g., 10 × 10 × 10 Å^3) with full periodicity in all directions gives the small cubic particle as shown in Fig. 1.10 E, which displays a predominance of [001]-like terraces on each face. These cubes are common in studies where one wants a finite particle but with clear, extended {001} facets.[106]

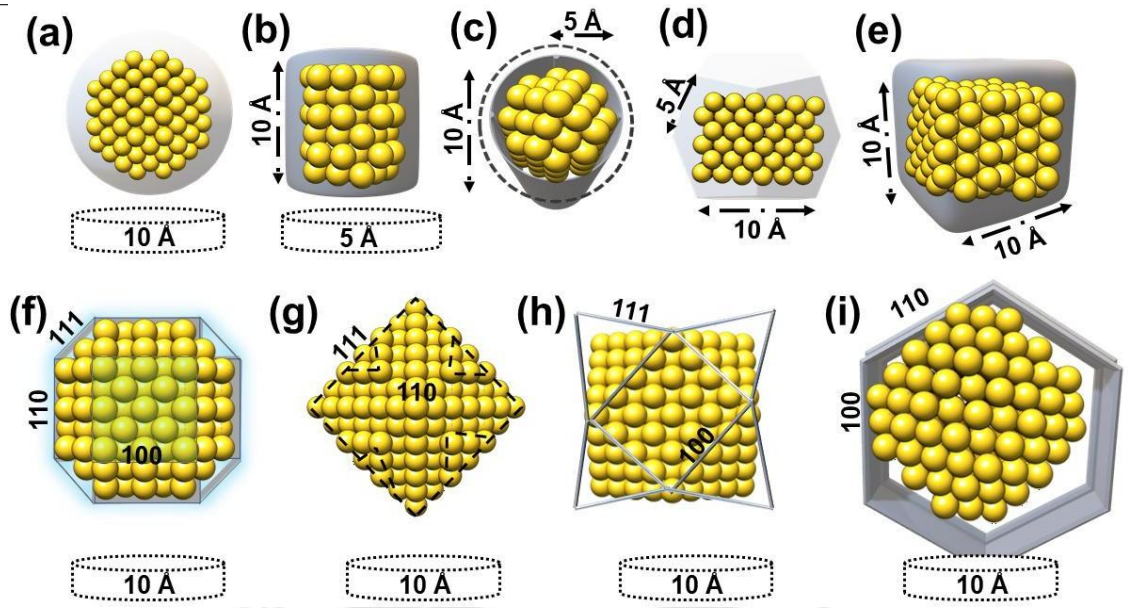

Figure 1.10: Representative gold nanoparticle (AuNP) geometries generated with CHARMM-GUI Nanomaterial Modeler using Interface Force Field parameters for fcc gold. Gometric models constructed by specifying target dimensions and periodicity for (a) compact quasi-spherical Au cluster, (b) short Au nanorod, (b) cylindrical AuNP, (d) thin Au[111] slab, and (e) small cubic AuNP with predominantly [100] terraces. Wulff-type polyhedral AuNPs where facet exposure is tuned by selecting combinations of Miller indices and associated surface energies, shown for (f) mixed-facet particle exposing [111], [100], and [110]; (g) [111]-dominated morphology with minor [110] edges; (h) [100]-rich polyhedron with smaller [111] caps; and (i) [110]/[100]-enriched particle highlighting high-energy facets.

Likewise, modeling Wulff-type equilibrium shapes for AuNPs by combining explicit Miller indices and orientation-dependent surface energies is shown in the lower panel of Fig. 1.10 (E). In the Wulff construction, the distance of each facet from the particle center is proportional to its surface free energy $\gamma(hkl)$, which are supplied as $\gamma(111)$, $\gamma(100)$, and $\gamma(110)$ from the Interface Force Field database, CHARMM-GUI can generate polyhedra that minimize total surface energy for a given volume. For gold, the typical hierarchy $\gamma(111) < \gamma(100) < \gamma(110)$ means that [111] facets tend to dominate at equilibrium, with smaller contributions from [100] and only limited [110] exposure. This is accounting most of the experimental observations for AuNPs corresponding to the 5–20 nm size range as a truncated octahedra or related shapes made mainly of [111] and [100] faces. Wulff-type particle where [100], [110], and [111] facets all appear on the surface is shown in Fig. 1.10 (F). Such mixed-facet models are useful when studying structure–activity relationships in catalysis, because catalytic turnover often localizes on edges and corners where different facets meet, and the junctions mimicking realistic

nanocrystal catalyst. Barmparis et al. In his study showed that for Au particles below about 16 nm, equilibrium shapes derived from such Wulff constructions match experimental transmission electron microscopy quite well, with surfaces dominated by [111] and [100] and only minor appearance of higher-index planes. In MD simulations, these [111]-rich models are often chosen to represent thermodynamically stable seeds growth and to benchmark surface diffusion of adsorbates under near-equilibrium conditions.[106,107] In **Fig. 1.10 (H)**, a more [100] - dominated polyhedron, where square facets are clearly visible and the [111] facets appear as smaller triangular caps. For AuNPs, such [100]-rich morphologies are important because they exhibit distinct adsorption energies and electronic properties compared with [111] surfaces, impacting reactions like oxidation, and electron transfer at AuNP interfaces. Using CHARMM-GUI models with controlled [100]/[111] ratios allow simulation studies to separate geometric and chemical contributions to these facet-dependent effects in a consistent force-field framework. Fig. 1.10 (I) shows [110] feature prominent alongside [100]. MD simulations on such [110]-rich AuNPs have been used to rationalize experimental observations where high-index or stepped surfaces show enhanced catalytic rates or stronger protein adsorption compared to low-index [111] surfaces.[99,108,109]

1.6.2 Integration of Experimental and Computational Approaches

Despite significant advances in both experimental characterization and computational modeling of functionalized AuNPs, these approaches are often pursued in parallel rather than in a fully integrated manner. Experimental studies report LSPR responses for specific linker–AuNP systems, this might lack the Conversely, computational works frequently focus on model systems that are only loosely connected to experimentally realizable conditions, limiting their immediate applicability to sensor design. Bridging this gap requires coordinated studies where experimental observables and simulation outputs are explicitly correlated, allowing mutual validation and refinement of both approaches.

In the context of enzymatic sensing of oxidative stress biomarkers, such integration is particularly valuable. Experimental determination of enzymatic parameters for allantoinase, such as Michaelis constant, maximum velocity, and operational stability upon immobilization, provides critical input for biosensor performance modeling. At the same time, MD simulations of linker-modified AuNPs can illuminate how surface chemistry influences enzyme loading density, orientation, and microenvironment, which in turn affect the experimentally measured kinetic parameters and optical responses. By iteratively comparing simulation-predicted trends in surface coverage, mobility, and binding energetics with adsorption isotherm parameters and plasmonic readouts, a deeper mechanistic understanding of the entire sensing interface can be

achieved.

Such an integrated framework is aligned with broader trends in nanobiointerfaces research, where multiscale simulations are increasingly used to rationalize experimental data and guide the design of plasmonic biosensors with improved sensitivity, selectivity, and robustness. For complex systems like enzyme-functionalized AuNPs employing bifunctional linkers, this combined approach is essential to disentangle the contributions of linker chemistry, nanoparticle morphology, enzyme properties, and environmental conditions to the overall sensor performance.

1.7 Research Gap and Motivation

Although allantoin has gained considerable attention as a non-invasive biomarker of oxidative stress in humans and experimental models, there remains a lack of biosensing platforms that simultaneously demonstrate high selectivity, sensitivity, and operational simplicity for its detection in complex biological matrices. Existing analytical approaches are dominated by chromatographic and mass spectrometric techniques, which, while accurate, are not readily translatable to routine clinical or point-of-care settings. Enzymatic biosensors based on allantoinase offer a promising alternative, but systematic investigations of the underlying enzymatic parameters, especially in immobilized and nanostructured contexts, are limited. A detailed characterization of allantoinase kinetics, stability, and performance in conjunction with plasmonic transducers is therefore needed to realize practical devices for oxidative stress assessment.

On the nanomaterials side, AuNP-based plasmonic sensors have achieved impressive sensitivity for a variety of analytes; however, the role of bifunctional thiol-based linkers such as DSP and DTSSP in modulating colloidal stability, surface coverage, and optical response has not been comprehensively elucidated. Many studies employ these linkers as convenient crosslinking agents without fully characterizing their adsorption mechanisms or quantifying their impact on LSPR properties and aggregation behavior under biosensing conditions. Comparative analyses of DSP and DTSSP, particularly in aqueous environments and under conditions relevant to enzyme immobilization, are sparse. In addition, the use of adsorption isotherm models to connect linker binding parameters with plasmonic behavior and biosensor performance remains underexplored.

At the molecular level, there is a notable gap in atomistic understanding of how DSP and DTSSP arrange and diffuse on curved AuNP surfaces, how solvation and electrostatic interactions shape their organization, and how these factors correlate with macroscopic

observables such as adsorption isotherm parameters, zeta potential, and LSPR shifts. While MD simulations have been applied to thiolated ligand shells and protein adsorption on AuNPs, there is a lack of studies that specifically target bifunctional NHS-based linkers and directly integrate simulation outcomes with experimentally measured adsorption and optical data.

Consequently, current literature lacks a unified study that: (i) develops and characterizes an enzymatic sensing framework for allantoin based on allantoinase, (ii) systematically investigates the adsorption, surface chemistry, colloidal stability, and plasmonic response of AuNP platforms functionalized with DSP and DTSSP, and (iii) employs molecular dynamics simulations to elucidate the molecular-level behavior of these linkers on AuNP surfaces and to correlate these insights with experimental adsorption and optical measurements. Addressing this gap is essential for rationally designing AuNP-based biosensors that harness both the specificity of enzymatic recognition and the tunability of plasmonic transducers, grounded in a mechanistic understanding of the underlying nanobiointerface.

1.8 Objectives of the Present Thesis

In light of the above considerations, the overall aim of this thesis is to construct a coherent, mechanistically informed framework that integrates biochemical sensing, plasmonic nanomaterials, surface chemistry, and computational modeling for biosensing purposes. The work is structured around three interlinked objectives that collectively bridge biochemistry, nanoplasmonics, and computational chemistry.

Objective 1: To investigate evolutionary relationships and structural variables influencing adsorption in allantoinase proteins from diverse sources through comparative sequence and three-dimensional structural analyses, with emphasis on substrate-binding sites, amino acid interaction networks, molecular packing, hydrophobic surface area, and overall surface characteristics.

Objective 2: To experimentally investigate and compare the sensing behavior using surface coverage kinetics, colloidal stability, and optical responses of thiol-based linkers DTSSP and DSP on citrate-stabilized gold nanoparticles, using spectroscopic, microscopic, and adsorption isotherm analyses, to identify an optimal linker for AuNP-based colorimetric biosensor platforms.

Objective 3: To elucidate the molecular-level adsorption mechanisms, interfacial dynamics, and binding energetics of DTSSP- and DSP-functionalized gold nanoparticles using all-atom molecular dynamics simulations, and to correlate computational insights with

experimental observations to rationalize linker-dependent aggregation, stability, and plasmonic behavior.

Taken together, these three objectives form a unified research framework in which biochemical characterization of allantoinase (Objective 1) defines the requirements for selective enzymatic detection; systematic experimental study of linker-functionalized AuNPs (Objective 2) provides the plasmonic transducer platform and quantifies how DSP and DTSSP govern surface properties and optical responses; and molecular-level simulations of linker–AuNP interfaces (Objective 3) explain and refine the interpretation of experimental data. This integrative approach aims not only to advance fundamental understanding of enzyme-functionalized plasmonic nanoparticles for oxidative stress biomarker detection but also to establish general design principles for nanoplasmonic biosensors that leverage coordinated

1.9 Thesis Contribution Statement

This thesis establishes two complementary frameworks for biosensor development. First, the enzymatic study demonstrates as a model for converting underexplored metabolic enzymes into biosensing elements by coupling enzymatic specificity with measurable physicochemical signals. Using allantoinase as a case study, the work outlines a systematic pipeline for identifying, characterizing, and integrating enzymes with sensing platforms, which can be extended to a wide range of catalytic proteins with biosensing potential. Second, the plasmonic nanoparticle study develops a predictive model linking linker chemistry, adsorption thermodynamics, and plasmonic behavior. By quantitatively correlating linker structure with surface organization and LSPR response, the work provides design rules for engineering functionalized gold nanoparticles with controlled sensitivity and stability. Together, these studies present a complete biosensor design strategy that integrates biological recognition with tunable plasmonic signal amplification, offering a general framework for the rational development of next-generation biosensing platforms.

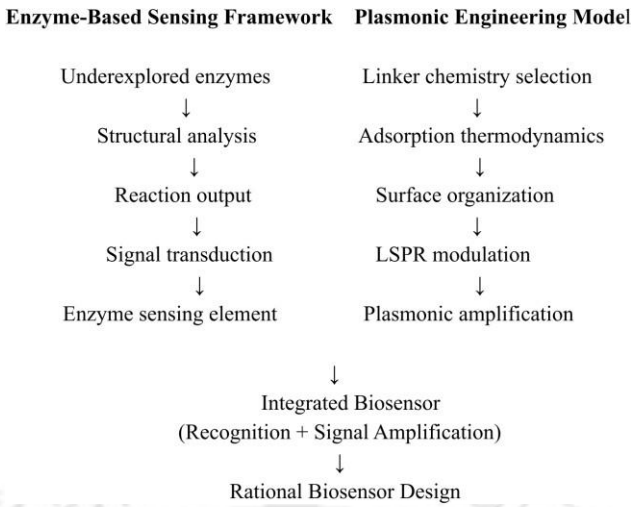

1.10 Thesis Structure

The work done during the doctoral program is organized into a thesis having six chapters, as following:

Chapter 1 presents the literature review and identifies the key research gaps addressed in this thesis. It outlines the overall framework of the study and introduces the enzymatic biosensor design based on allantoinase (Chapter 2) and the non-enzymatic plasmonic sensing approach (Chapter 4) with its computational validation (Chapter 5). The chapter also highlights the limited fundamental understanding of linker behavior in biosensing, which this work aims to address.

Chapter 2 consists investigation of allantoinases enzyme, from 86 different sources. These sequences were thoroughly evaluated to determine their biochemical and biophysical properties and to rank their suitability for immobilisation. When it comes to developing enzyme-based sensors, properties such as solubility, structural compactness, hydrophobicity, and hydrodynamic attributes must be thoroughly considered. The information is essential for the precise engineering of enzymes with specific biochemical and kinetic properties to achieve unparalleled sensitivity for analyte detection and long-term sensor stability against environmental perturbations. This study is helpful for future studies involving underexplored enzymes with potential for sensing.

Chapter 3 entails designing a protocol for image analysis based on gel electrophoresis. The objective of this work is to develop a quantitative understanding of agarose gel electrophoresis by analysing DNA band mobility, relative band intensity, and pore-

size distribution using ImageJ. By measuring migration distances and intensity profiles, this study aimed to correlate DNA transport with gel microstructure. Additionally, SEM-based pore-size analysis enabled quantification of the nanoscale architecture governing electrophoretic behaviour.

Chapter 4 involves a detailed comparative study of the mechanistic framework for AuNP functionalization. This chapter focuses on the quantitative experimental comparison of AuNP functionalization using DTSSP and DSP. The core finding revealed a stark difference in colloidal stability and optical response: DTSSP functionalization resulted in concentration-dependent aggregation, causing a large SPR red shift, which was visually confirmed. In contrast, DSP-functionalized AuNPs exhibited high colloidal stability, showing only a minimal SPR shift and retaining a well-dispersed morphology. Adsorption isotherm studies further quantified this difference, showing DTSSP had a significantly higher maximum adsorption capacity and reached saturation faster, while DSP exhibited a lower capacity but still showed favorable adsorption characteristics. These experimental results provided the definitive macroscopic evidence necessary for the molecular investigation in the subsequent chapter.

Chapter 5 This chapter established the molecular-level mechanism underpinning the experimental results from Chapter 4 using all-atom Molecular Dynamics (MD) simulations.

The findings conclusively linked the structural difference in the linkers to their functional outcomes. This chapter successfully validated the experimental findings by providing the quantitative, energetic, and kinetic reasons for the distinct DTSSP-mediated aggregation versus DSP-mediated stability.

Chapter 6 presents a comprehensive summary of the research carried out in this thesis and consolidates the key findings from all preceding chapters. It highlights the major scientific contributions of the study in the context of enzymatic and non-enzymatic biosensing strategies. The chapter also identifies remaining limitations and outlines potential directions for future research to address the existing gaps in the literature.

Chapter 2

Computational Evaluation of Allantoinase Structural Variables Influencing Adsorption

Abstract

Designing enzyme-based sensors necessitates a comprehensive exploration of macromolecular properties, including specificity, stability, and hydrodynamic attributes. Integrating an enzyme with a suitable transducer involves immobilizing it onto a surface, facilitated through adsorption or entrapment techniques. Allantoin, a stable biomarker metabolite, holds promise for detecting oxidative stress-related complications through its corresponding enzyme. In this study, we examined allantoinase from various taxa, with bacterial origin comprising over 70% of the dataset. Factors like relative pI, solubility index, and amino acid frequency-based hydropathy aid in estimating the basic solubility. The overall stability, along with the hydrophobic area, and thermostability using the aliphatic index, has been explored. Furthermore, the compactness and spherical geometry of the enzyme are crucial for protein adsorption and are evaluated through parameters like spatial conformation, asphericity, and hydrodynamic radius distribution. Bacterial allantoinase also demonstrates significant adaptability to environmental changes, as indicated by solvent-accessible surface area, hydrophobicity, and instability index. This study highlights the importance of the properties necessary for optimizing, calibrating, and ensuring the stability of enzyme-based sensor design.

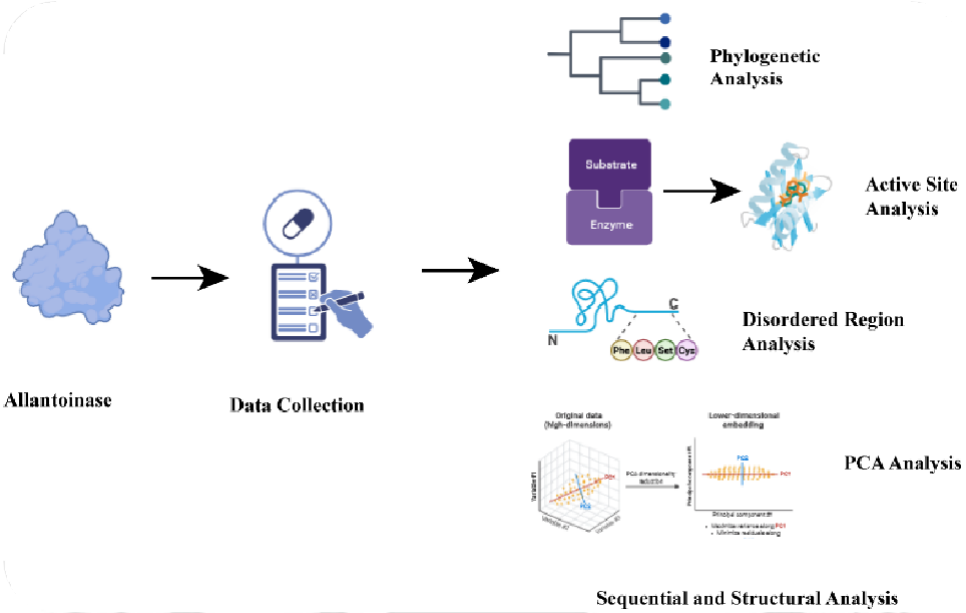

Figure 2.1: Workflow for sequential and structural analysis of Allantoinase

* This work has been published in:

Das, S., Krishnamoorthy, J., & Kar, R. K. (2025). Estimating the structural and spatial variables of allantoinase enzyme critical for protein adsorption. Biochemical and Biophysical Research Communications, 743, 151161.

2.1 Introduction

Purine metabolism is a central biochemical network that links nucleotide turnover, nitrogen disposal, redox homeostasis, and (in some organisms) energy generation. In all domains of life, the synthesis and degradation of purine nucleotides must remain tightly regulated to maintain balanced pools of ATP/GTP and of the corresponding deoxynucleotides needed for DNA replication and repair. Perturbations in these pathways can therefore influence diverse physiological outcomes, ranging from altered growth and development to inflammation and metabolic disease. Within the broader purine catabolic route, uric acid (urate) and its downstream oxidation products occupy a special position because they sit at the intersection of nitrogen metabolism and oxidative chemistry.

In many organisms, uric acid is further metabolized to allantoin and subsequently to allantoate and urea (or other downstream products depending on the lineage). The conversion of uric acid to allantoin occurs through oxidative steps in the same pathway and hence can generate reactive oxygen species (ROS). ROS are highly unstable and highly reactive molecular entities (including radicals and non-radical oxidants) capable of damaging lipids, proteins, and nucleic acids. When ROS generation exceeds the capacity of antioxidant defenses, oxidative stress develops, initiating or accelerating cellular dysfunction and disease progression.

2.1.1 Allantoinase and its role in purine catabolism

Allantoinase (EC 3.5.2.5), a member of the amidohydrolase (aminohydrolase) superfamily, plays a key catalytic role in this catabolic module by converting allantoin into allantoate (allantoic acid).[110] This transformation represents a chemically challenging hydrolytic opening of the imidazolidinedione ring of allantoin and thereby commits the metabolite to further degradation and nitrogen recovery. In microorganisms and plants, efficient utilization of purines can be advantageous under nitrogen-limited conditions, where purine degradation becomes a route to salvage nitrogen and carbon skeletons. More broadly, the enzymatic steps downstream of urate influence the steady-state concentrations of intermediates and can modulate the extent to which oxidative products accumulate. Thus, understanding the enzymes that regulate these downstream metabolic steps is essential for interpreting how oxidative intermediates are processed within the purine degradation pathway.

Allantoinase, a member of the amino hydrolase family, plays a crucial role in the purine metabolic pathway. Its primary function involves catalysing the conversion of allantoin into allantoic acid.[110] The substrate allantoin in this process is generated through the oxidation of

uric acid within the same pathway. Allantoinase significantly contributes to the efficient utilization of purines, ensuring the availability of nucleotide precursors for DNA and RNA synthesis [79]. The breakdown of purine metabolism results in the generation of reactive oxygen species (ROS), highly reactive molecules known to cause cellular damage.

2.1.2 Oxidative stress, antioxidants, and the urate-allantoin axis

Oxidative stress is closely linked to the progression of pathological conditions, including diabetes, arthritis, and cardiovascular diseases, among others. The cellular response to oxidative stress includes enzymatic defenses (e.g., superoxide dismutase, catalase, and peroxidases) as well as small-molecule antioxidants that neutralize ROS and related free radicals. In human physiology, urate is estimated to contribute up to 60% of free radical scavenging capacity in human plasma, making it a critical antioxidant in bodily fluids.[111] The interaction between ROS and urate results in the production of the metabolite allantoin, serving as a stable marker of free radical activity in human serum. Furthermore, it has been proposed as a potential biomarker for oxidative stress, indicating a broad spectrum of diseases.[9,10]

The level of allantoin in the serum of healthy individuals ranges from 2 to 3 μg/L,[11] while in biofluids such as urine, it ranges from 14–800 μM, demonstrating its remarkable stability.[112] Monitoring allantoin levels can provide valuable insights into oxidative stress and the body's antioxidant defense effectiveness.[13,113] This hints at the necessity for developing sensors capable of accurately sensing allantoin levels. There are several methods of generating a sensing mechanism for the detection of allantoin. Allantoinase can be immobilized on a surface material, such as a low-dimensional nanomaterial or nitrocellulose matrix.[16] When biofluids containing allantoin come into contact with the sensor, the analyte binds to the immobilized enzyme, inducing detectable changes in physical properties. These changes can be observed through various methods, including optical signals (UV/Vis, fluorimetry, chemiluminescence, and surface plasmon resonance) and electrochemical techniques (cyclic voltammetry and amperometry), for precise clinical diagnostics.

The potential application of allantoinase extends well beyond enzymatic and physiological function, offering opportunities in sensor development. Despite its biological relevance, allantoinase remains relatively underexplored, with limited information available regarding its structural characteristics and detailed functional properties. Despite allantoin's significance as a potential biomarker, there is a knowledge gap in the surface immobilization of allantoinase enzyme.[12] Access to sequential and structural information about allantoinase variants can provide valuable insights, aiding in the development of stable sensor prototypes through protein engineering.

2.1.3 Motivation for sensing: why enzymatic detection of allantoin?

Monitoring allantoin can provide insight into oxidative stress burden and into the effectiveness of antioxidant defenses in vivo. However, conventional analytical workflows (often chromatographic or mass-spectrometric) can be time-consuming, require specialized instrumentation, and may be poorly suited for point-of-care settings. These practical limitations motivate the development of selective, inexpensive, and rapid sensors that can quantify allantoin directly in complex matrices such as serum, urine, saliva, or sweat.

Enzyme-based sensors are particularly appealing for polar, small-molecule analytes because enzyme active sites provide molecular recognition and catalytic amplification. In an allantoinase-based sensor concept, immobilized allantoinase captures and converts allantoin, and the associated chemical transformation is transduced into an observable signal. Depending on the sensor architecture, the signal may arise from changes in absorbance/fluorescence, from coupled reactions that generate electroactive species, or from alterations in interfacial properties that can be read out by electrochemical or optical methods.

A central technical challenge in such devices is that the enzyme must operate efficiently when constrained on or within a material matrix. Immobilization can perturb enzyme conformation, modify access to the active site, and introduce mass-transport limitations. At the same time, immobilization can improve reusability, simplify integration into portable formats, and enhance stability by reducing aggregation or proteolytic susceptibility. Thus, the design of an effective allantoin sensor depends strongly on understanding how allantoinase behaves at interfaces.

2.1.4 Enzyme immobilization: materials, mechanisms, and performance constraints

To function as a practical biosensing element, allantoinase must be immobilized on a surface or within a scaffold, such as low-dimensional nanomaterials (e.g., nanoparticles, nanofibers, nanosheets) or porous matrices including nitrocellulose. Immobilization strategies include physical adsorption, covalent attachment, affinity-based capture, and entrapment in polymeric networks. Each approach presents tradeoffs among simplicity, activity retention, orientation control, and long-term stability.

Physical adsorption is attractive because of its minimal chemistry and compatibility with many substrates, but it can be sensitive to ionic strength and pH and may allow enzyme leaching. Covalent attachment can improve robustness, yet it risks modifying residues essential for catalysis or structural integrity unless attachment sites are carefully chosen. Affinity-based approaches (e.g., tag-mediated binding) can enforce orientation but require engineered

constructs and may add cost or complexity. Entrapment and hydrogel-based methods can preserve local hydration and reduce denaturation, but may introduce diffusional barriers for the analyte.

In all cases, a fundamental requirement is that the immobilized enzyme maintains (i) access of allantoin to the binding pocket, (ii) catalytic turnover under the relevant pH and ionic conditions, and (iii) mechanical and chemical stability over the intended device lifetime. These requirements connect molecular-scale properties (surface charge distribution, hydrophobic patches, flexible loops, oligomer interfaces, and the geometry of the active site) with device-scale performance metrics such as sensitivity, selectivity, response time, and operational stability.

Sensor readouts can be implemented via optical or electrochemical modalities. Optical methods include UV/Vis absorbance, fluorimetry, chemiluminescence, and surface plasmon resonance, while electrochemical methods include cyclic voltammetry and amperometry. The selection of a transduction method typically depends on the target matrix, required detection limit, and integration constraints (e.g., whether the platform is disposable, wearable, or compatible with microfluidics). Importantly, the immobilization matrix itself can influence signal generation, for instance by quenching fluorescence, altering refractive index near the surface, or contributing background currents.

Our objective in this work is to gain structural insights into enzymes and uncover hidden trends in their properties, such as surface charge, hydrophobicity, voids, and substrate specificities – critical factors in protein adsorption or immobilization. Allantoin, a chemically polar molecule found in body fluids, rapidly increases in concentration in response to oxidative stress.[12,15] Previous studies on allantoinase, employing a recombinant approach with high-yield expression, suggests the potential for precise modulation of its functional activity.[114–116] Our work focuses on a comprehensive analysis of allantoinase proteins from diverse sources, utilizing bioinformatics techniques to establish evolutionary relationship through the primary sequences of homologous proteins. Subsequent analysis delves into the three-dimensional structure of the proteins, with a particular emphasis on the substrate binding site, amino acid network, intrinsic volume, hydrophobic area, and surface analysis. Acquiring such information is invaluable for understanding critical details about structure, substrate specificity, and the impact of the environment on adsorption specificity and analyte sensitivity.

2.1.5 Knowledge gap and need for structural/bioinformatic insight

Despite the relevance of allantoin as a potential biomarker and the clear promise of

enzyme-based sensing, there remains a tremendous knowledge gap regarding how allantoinase variants behave upon surface immobilization and which molecular features best predict adsorption specificity and retained activity. Allantoin is a chemically polar analyte; therefore, subtle differences in the electrostatics and hydrogen-bonding capability of the substrate-binding pocket, as well as the distribution of polar residues on the protein surface, may strongly influence both catalytic efficiency and immobilization behavior.

Access to sequence and structural information across allantoinase homologs provides an opportunity to rationally select or engineer enzyme candidates for sensing applications. Sequence analysis can reveal conserved catalytic motifs and cofactor-binding residues, while also identifying variable regions that may tune stability, oligomerization, or surface properties. Phylogenetic relationships inferred from primary sequences can help organize homologs into clades that share functional characteristics or environmental adaptations (e.g., thermophily, halotolerance), which may translate into desirable device performance.

Structural analysis complements sequence-based approaches by providing a three-dimensional view of the features most relevant to immobilization and sensing. These include surface charge patterns that govern electrostatic adsorption, hydrophobic areas that mediate nonpolar interactions with materials, voids and internal packing that correlate with stability, and the geometry and accessibility of the active site. In addition, mapping residue networks around the substrate-binding pocket can reveal potential allosteric couplings or mutational hotspots that enable modulation of activity without compromising folding.

2.1.6 Scope and objectives of this work

The objective of this work is to gain structural insights into allantoinase enzymes and to uncover trends in properties that are critical for adsorption and immobilization, including surface charge, hydrophobicity, internal voids, and determinants of substrate specificity. We focus on a comprehensive analysis of allantoinase proteins from diverse sources, using bioinformatics tools to establish evolutionary relationships through primary-sequence comparisons of homologous proteins. Building on these relationships, we analyze three-dimensional structures (experimental when available and/or predicted models when appropriate) with particular emphasis on the substrate-binding site, amino-acid interaction networks, intrinsic volume and packing, hydrophobic surface area, and overall surface characteristics.

By linking evolutionary variation to structural features and physicochemical descriptors, this work aims to inform the rational selection and engineering of allantoinase

variants for robust biosensing. In the broader context of oxidative stress monitoring, such insight supports the development of stable sensor prototypes capable of accurately quantifying allantoin in clinically relevant matrices and thereby enabling improved assessment of physiological stress and disease Furthermore, recombinant expression approaches reported for allantoinase suggest that functional activity can be tuned and that high-yield production is feasible, providing a practical foundation for protein engineering and device integration.

Overall, the interplay among purine catabolism, redox chemistry, and biomarker detection motivates a systematic investigation of allantoinase at the sequence and structure levels. Understanding how molecular properties govern catalytic function and interfacial behavior is essential for translating a biologically important enzyme into a reliable analytical component.

2.2 Materials and methods

Data collection. Our investigation beings with 19 protein sequences associated with the PuuE and DAL1 genes, encoding the allantoinase enzyme. These sequences were obtained from a comprehensive list reported by Ramazzina *et al.*[117] We expanded the allantoinase dataset using BLAST (Basic Local Alignment Search Tool) analysis, obtaining 304 similar/homologous sequences.[118] Subsequently, we annotated these sequences using the NCBI server. To cross-correlate, we utilized AlphaFold database and retrieved the predicted three-dimensional structural models for these proteins.[119] This resulted in a refined dataset comprising of 86 protein models, which were further analyzed.

Phylogenetic analysis. A phylogenetic tree was constructed to analyze the evolutionary relationships among the datasets using the Molecular Evolutionary Genetics Analysis (MEGA11) software.[120] The parameter utilized include a gap opening of -2.9, hydrophobicity multiplier of 1.2, with the clustering method of unweighted pair group method with arithmetic mean (UPGMA). The process commenced with a multiple sequence alignment using the MUSCLE algorithm, followed by iterative refinement and progressive alignment of sequences to improve the scoring function.[121] This approach facilitated accurate alignments, particularly for divergent sequences. For tree construction, Jones-Taylor-Thornton substitution model with tree interference option of nearest-neighbour interchange were employed. For the phylogeny test, bootstrap analysis with 1000 replicates were used to obtain the branching patterns. Statistical significance was verified using the maximum likelihood score.

Dataset annotation and management. The Interactive Tree of Life (iTOL) algorithm was employed to annotate and generate phylogenetic tree.[122] The datasets were color-coded

and major taxa were labeled based on relevant features to gain insights into the evolutionary history and relatedness within the allantoinase dataset.

Analysis of isoelectric point (pI). To understand solubility properties, we calculated the isoelectric point (pI) and hydropathy index (GRAVY) based on primary sequences. For the pI values, we employed Expasy,[123] Prot pi, Isoelectric point calculator,[124] and Protcal protein calculator. The solubility index of the enzymes was calculated using Soluprot v1.0.[125] The algorithm not only predicts the likelihood of soluble protein expression in *E. coli* but also reflects the solubility and expression of the target proteins. The overall amino acid composition was analysed using the box-plot method and the BioEdit program v.7.2.[126]

Active site residues analysis. The binding site of allantoin in the enzyme's active site was analysed, for which the crystal structure of PuuE allantoinase (pdb code 3CL7) was first analysed to pinpoint the ligand-binding residues. Using AutoDock Vina PyRx0.8, we conducted docking calculations,[127] starting with the 3D-SDF format of allantoin, optimised using Open Babel. With the grid centre fixed at 1.16, -0.34, and -1.14 Å coordinates, we employed Gasteriger-Marsili charges for electrostatic description. The docked complex with lowest binding energy was considered for analysis. The active sites of the remaining AlphaFold-predicted allantoinase models were subsequently identified through sequence and structural alignment with the reference structure (3CL7), and conserved residues corresponding to the binding pocket were used for comparative active-site analysis.

By comparing the spatial distribution of active site residues with probable disordered regions, we obtained the active site residues' information from allantoinase structure. The coordinates of side chain residues within 4 Å of the bound ligand have been considered as the active site residues. This data holds significant potential for tuning the sensitivity of enzyme-based biosensors. After aligning the active site residue lists and processing through COBALT multiple alignment server[128] and WebLogo,[129] we obtained amino acid frequency for comparison across taxonomic group of bacterial, fungal, arthropod, and chordata categories.

Disordered region prediction. The disordered region was estimated using PrDos.[130] A FASTA formatted sequence serves as input to create a position-specific score matrix, and compared to non-redundant structural information from the PDB through a PSI-BLAST search. Amino acid occurrence and weighted based on sequence encoding scheme, enabling the calculation of disorder probability for individual amino acids.

Estimates for instability index and extinction coefficient. The instability indexing for the bacterial allantoinase was determined using the ProtParam tool. The algorithm takes into

account empirical parameters for dipeptides based on statistical analysis from a stable and unstable proteins' dataset, reported elsewhere,[131,132] assigning weight to compute the instability index. For $i = L - 1$, where L is the sequence length and the instability weight for a dipeptide starting at position i, it is denoted as DIWV(x[i]x[i+1]), for which the instability index is calculated using Equation 1.

$$Instability\ Index = (\frac{10}{L}) \times \sum_{i=1}^{L-1} DIWV(x[i]\ x[i+1]) \quad \text{Eqn (1)}$$

If the computed instability index for a protein sequence is <40, it suggests that the protein is likely to be stable. This information aids in selection of suitable host organisms. Another key parameter, is the extinction coefficient, which measures the relative absorption of light in diverse environments. These estimates are based on calculating the molar extinction coefficient for a specific sequence and on correlating the amino acid composition with the spectral signature under native/denaturing solvent conditions.[132] Such estimates are highly beneficial for spectroscopic characterization of a protein, especially during its purification process.

Structural insights from volume calculation. Allantoinase molecular surfaces were analysed using ProteinVolume server to obtain valuable insights into the intrinsic volumes [111]. The algorithm refers as flood-fill, calculate void (V_{void}) and van der Wals volume (V_{vdW}), based on cartesian coordinates, contributing to the total volume ($V_{total} = V_{void} + V_{vdW}$). This algorithm includes energy minimization to avoid steric clashes, employing a volume probe at the protein's centre of mass and extending outward in systematic steps.[133] For correlation analysis, we excluded the allantoinase from *Spathospora* sp., which has the longest sequence with a total residue 758.

Aliphatic index analysis. Theoretical estimates for the volume occupied by the aliphatic side chains (Ala, Val, Ile, Leu) provide insights into thermal stability, a crucial aspects of protein engineering. These calculations, based on Equation 2, demonstrate how the relative volume of hydrophobic amino acids influences a protein's susceptibility to denaturation caused by environmental factors.

$$Aliphatic\ index\ =\ X(Ala) + a * X(Val) + b * [X(Ile) + X(Leu)] \quad \text{Eqn (2)}$$

Where X represents the mole percentage of respective aliphatic amino acids, while the coefficients a and b define the relative volume of the side chain of Val and Ile or Leu, respectively (a = 2.9, b = 3.9).

Solvent Accessible surface area calculation. SASA calculation involves using a probe sphere, typically a water molecule with a radius of 1.4 Å to numerically assess the interaction of individual amino acids and estimate the accessible surface area ($Å^2$).

Surrounding Hydrophobicity and LRO: We also account for surrounding Long Range Order (LRO) and Hydrophobicity (H_p) to gain insights into the enzyme's stability. Using the SRide server,[134] a BLAST search with an E-value threshold of 0.001 was conducted to identify conserved residues crucial for stability. The maximum number of homologous sequences for conservation score is 50 with a threshold value of 6. The parameters for calculations, including threshold for LRO and H_p set at 0.02 and 20, respectively. The surrounding Hydrophobicity (H_p) encapsulates the theoretical summation of the hydrophobic index for residues within an 8 Å radius.[135]

Hydrodynamic properties. Structural properties associated with degrees of freedom include hydrodynamic radii, such as anhydrous – Ro, rotational – R_T, and translational – R_R properties. Our calculations also consider spatial conformational distribution, including the radius of gyration (Rg) and specific volume. We also collected parameters like Dmax, axial ratio, intrinsic viscosity, and asphericity. These calculations were performed using HullRad,[136] which employs a convex hull model to estimate the hydrodynamic properties associated with the physical orientation of macromolecules.

Principal component analysis (PCA). The PCA was performed using an inhouse written matlab program considering the 16 features such as, Total no. of AA, Disorder Ratio, SASA, Total Hp, SUM LRO, Dmax, f/fo, Asphericity, Total Volume (A3), Void Volume, VDW Volume, Aliphatic index, Solubility Index, Extinction Coefficient, Instability Index and Cys Residue count. The features were labelled as F1 to F16 as in the presented order. The species of organisms considered were labelled from 1 to 63. The scores and loadings were obtained for different PCs and the inherent clustering if present within these species will be visibly discernible in the scores plot. The features responsible for the clustering in the score plot can be identified using the loading vectors. If the loading vectors are long (higher magnitude) and directed towards a cluster then, we interpret it as up regulation of the corresponding feature for that cluster. The automated clustering (based on the PCA scores values) was performed using *dbscan* algorithm by setting the *epsilon radii* value to 0.01 and *minimum points in cluster* to 5.

2.3 Results

Our investigation aims to explore the structural attributes of allantoinase enzymes

encoded by DAL1 and PuuE genes. These enzymes share similar catalytic activity and structural features, such as α-β barrel.[117] Notably, DAL1 with a fungal origin, demonstrates broader organism distribution compared to PuuE, which originates from bacteria. PuuE contains specialized domains known as polysaccharide deacetylase and they are involved in maintaining cell wall components.[137] Conversely, DAL1 contains the component amino hydrolase, directly involved in the metabolism of purine components. Significant changes in the protein sequence and structure during the evolution of allantoinase have led to substitutions of amino acids in the active site. These substitutions have enabled the enzyme to function independently of metal ions and adapt to a new substrate, allantoin, departing from its original polysaccharide substrate.

2.3.1 Phylogenetic analysis

Understanding the intricate evolutionary dynamics of enzyme families is vital for comprehending how amino acids govern their structural and functional attributes. Genetic substitutions not only dictate functional shifts but also significantly impact physiochemical outcomes. Using phylogenetic analysis, tracing the divergence/convergence we gained insights into vital role of enzymes in the cellular domain and their corresponding signalling cascade. It also shed light on the factors that contribute to enzymes stability, global folding, and steady protein-protein interacting interfaces.

In Fig. 2.2, the phylogenetic tree shows the distances between clade. The branch lengths provide the scale of separation among the origin of enzymes. Among the 86 species in the phylogeny, the majority, comprising 63 proteins, belongs to bacterial species. Additionally, there are 6 enzymes from fungi, 1 from the plantae kingdom, and a few more from phylum mollusca, chordates, and athropods, totalling 1, 6, and 9, respectively. Consequently, the number of branches is limited to three or less due to a smaller number of proteins in the dataset.

Notably, the bacterial species exhibit divergent branches with more than six major nodes, with dominant species like *Deinococcus* – 7, *Streptomyces* – 14, and *Desulfosporosinus* – 10. Other enzymes from popular species such as *Escherichia*, *Bacillus*, and *Salmonella* account for ≤ 3. Overall, the data indicates that for allantoinase, the functional annotation of bacterial enzymes has intriguingly evolved compared to other taxa. It is important to highlight that a majority of protein expression on the laboratory-scale relies on bacterial plasmid/constructs. Henceforth this analysis holds significant relevance in the selection of specific bacterial strains for downstream processing.[138]

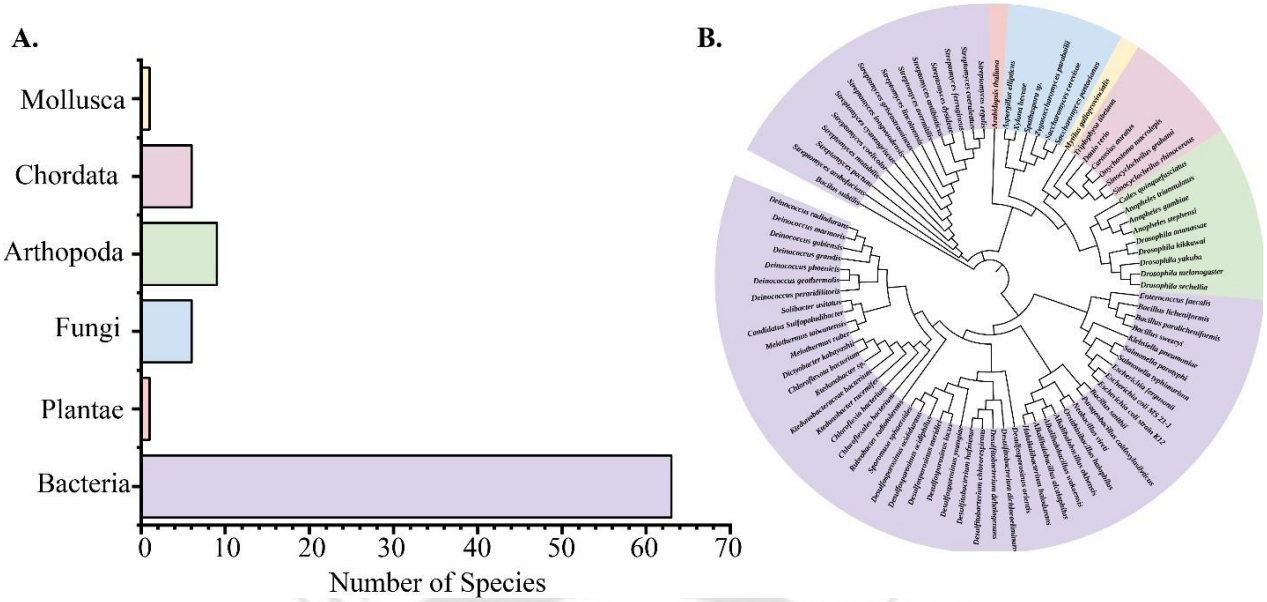

Figure 2.2: Phylogenetic analysis of alantoinase sequences (A) The number of sequences falling under specific clade. (B) Representative phylogenetic tree with clade distances and nodes corresponding to evolutionary related sequences

2.3.2 Isoelectric point analysis.

The isoelectric point (pI) is a critical parameter in protein biochemistry as it determines the pH at which the protein carries no net charge. It provides insight into the overall energy distribution, relevant for protein's physical properties. Accurate pI estimates are essential for protein purification. We computed the theoretical pI values for the 86 protein sequences encoding allantoinase and analyzed their trends using statistical parameters. Fig. 2.3 illustrates the pI values for all sequences, with a mean value of 5.62. The majority of sequences cluster around the mode value of 5.22, suggesting a preference for slightly acidic conditions. However, a few outliers with higher pI indicate a subset of sequences with more alkaline properties. The standard deviation was calculated to be 0.52, signifying a moderate degree of variability among the sequences. The data also revealed positive skewness of 2.21 and a high kurtosis value of 8.57, reflecting that the tail of data (leptokurtic distribution) is towards higher pI. A 99% confidence interval analysis shows that majority of allantoinase lie within a specific pI range. The upper confidence interval (UCI) of 5.77 and a lower confidence interval (LCI) of 5.47 were found.

Detailed analysis across the biological kingdoms (Eubacteria, Fungi, Plantae) and Phyla (Chordata, Mollusca, Arthropoda), provides a comparative outlook. Within the fungi kingdom (n=6), an average pI of 5.67 was observed, indicating a propensity towards slightly acidic to neutral properties. In the Arthropoda phylum (n=9), the pI values range from 5.16 to 6.09, suggesting moderately acidic to neutral charge distribution. Conversely, Chordata

exhibits an extensive pI range from 5.22 to 6.88, with an average of 6.02 (n=6), indicating a shift from slightly acidic through to marginally basic properties. This demonstrates a broader variability in pI within Chordata species as opposed to Fungi and Arthropoda.

The larger segment representing bacterial allantoinase (n=63), displaying a pI spectrum from 4.93 to 8.35 (average 5.54). This extensive distribution underscores a significant diversity in charge properties. The mean pI places bacterial allantoinase between Fungi and Arthropoda in terms of charge distribution, with *Zygomycces parabaili* presenting an outlier pI of 8.35, markedly alkaline. Additionally, *Streptomyces* species (n=14) unveils a pI range from 5.05 to 5.81, indicating a potential difference in the charge characteristics of allantoinase within the phylum. These variabilities in isoelectric points underscore their profound significance in experimental settings, particularly in elucidating the implications on enzyme function, stability, and potential applications.

We further observed that algorithms for predicting pI values vary in results. By comparing outcomes from different sources (Prot Cal, ProtpI, and IPC with the Expasy tool), we can assess reliability and accuracy in pI values reporting. Specifically, Prot Cal and Prot pI tend to underestimate pI values, while IPC overestimates them, as visualized in Fig. 2.3(C). Likewise, Expasy, shows significant differences. Nevertheless, they show relatively similar trend in the pI values.

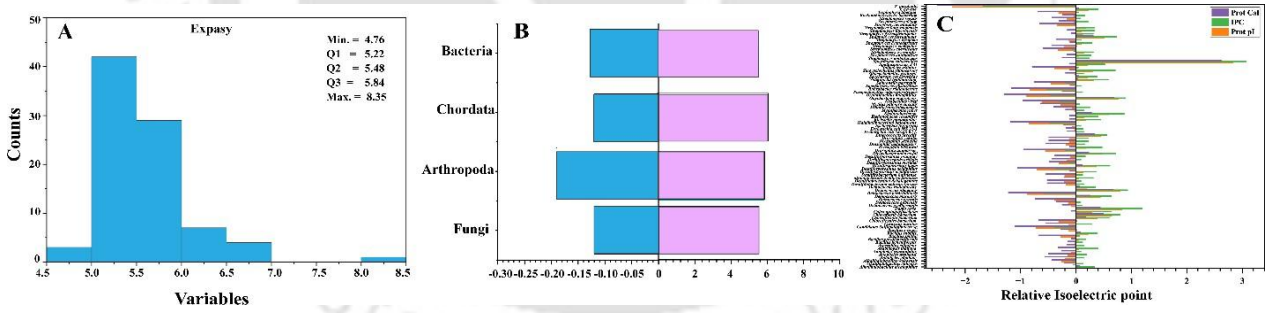

Figure 2.3: (A) Histogram for Isoelectric point and (B) Comparison of mean value of pI and GRAVY value for different taxa. (C) Box plot showing the amino acid frequency (%) information for the 84 allantoinase sequences

2.3.2 Analysis of GRAVY.

The analysis of GRAVY (Grand Average of Hydropathicity) for allantoinase offers valuable insights into protein's hydrophobic and hydrophilic property, which are based on the Kyte-Doolite and Hopp-Woods scale for individual amino acids. The extent of hydrophobicity is indicated by a positive score and for our dataset (**Fig. 2.4**), GRAVY value ranges from -0.33 to 0.17, with the most hydrophilic and hydrophobic enzymes corresponding

to *Anopheles triannulatus* and *Chloroflexales bacterium*, respectively. Though the mode GRAVY value corresponds to -0.15, the mean value is -0.13 indicating the overlap in distributed data. The GRAVY value peaks at -0.19 for arthropod allantoinase, aligning closely with the pI value. inclining towards the hydrophilic range. Interestingly, for fungi, chordata, and bacteria, the average values are similar, that is -0.12. However, a weak correlation is observed between the distribution of pI and GRAVY values for the allantoinase dataset, highlighting the complexity of protein behavior.[139]

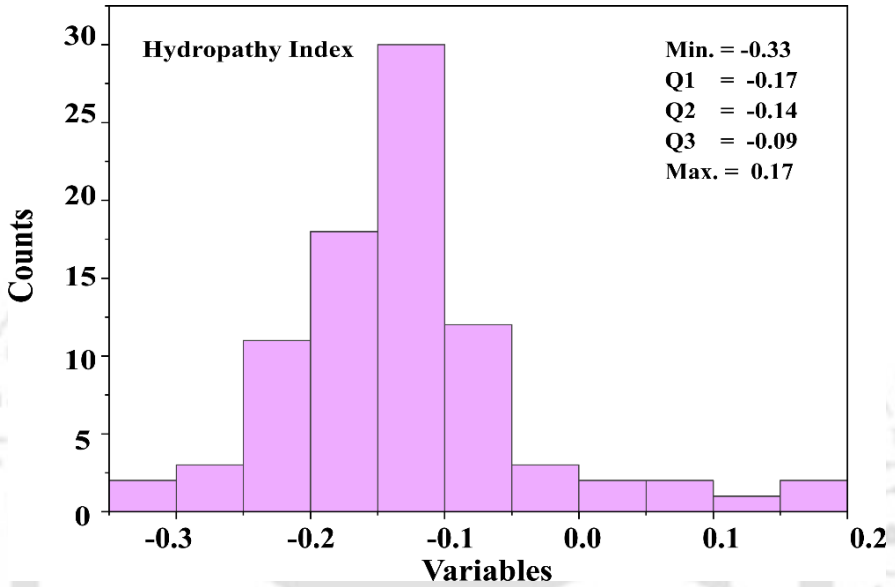

Figure 2.4: Histogram plot for GRAVY value for all species

2.3.3 Analysis of protein solubility parameters.

Maintaining proteins in a soluble state is a critical aspects of protein biophysics. Majority of allantoinase solubility parameter are at the concentrations at which they are marginally soluble. This limited solubility can decrease protein yield, whereas achieving optimum solubility can help preserve the protein in its native state with a stable conformation. The soluble state of allantoinase protein is essential for ensuring optimal enzymatic activity, critical for detecting allantoin in a biosensor prototype. This stable state can significantly enhance performance and efficacy, allowing the analyte to be detected even at low concentrations. The information holds value as it streamlines the enzyme immobilization process, thereby simplifying fabrication processes.[125]

Through SoluProt program, the gradient boosting machine learning technique was employed to reveal an intricate relationship between solubility and insolubility of these proteins, to access their potential for overexpression in *E. coli*.[140] Nearly 62 % of sequences exhibited a solubility index below 0.5, indicating high propensity for insolubility during expression (Fig. 2.5). It also indicates challenges associated with expressing and purifying

these proteins. Furthermore, *Streptomyces* species (n=14), displayed solubility index ranging from 0.32 to 0.47, with an average of 0.39. These figures cast doubt on efficacy of expressing and purifying enzymes from this species without any side-directed mutagenesis. Similarly, enzymes from *Deinoccocus* (n=7) exhibited lower solubility tendencies. On the contrary, 33.4 % of the allantoinase enzymes are lying above 0.5 solubility index, hinting their potential for soluble expression. The species set of *Desulfosporosinus* (n=6) and *Desulfitobacterium* species (n=4) hovered over borderline solubility with an average of 0.49 and 0.53. Species from *Escherichia coli* (strain MS21 and K12), *Salmonella species, E. faecalis, H. halodurans* and *K. pneumoniae* showcased remarkable solubility index of ca. 0.8.

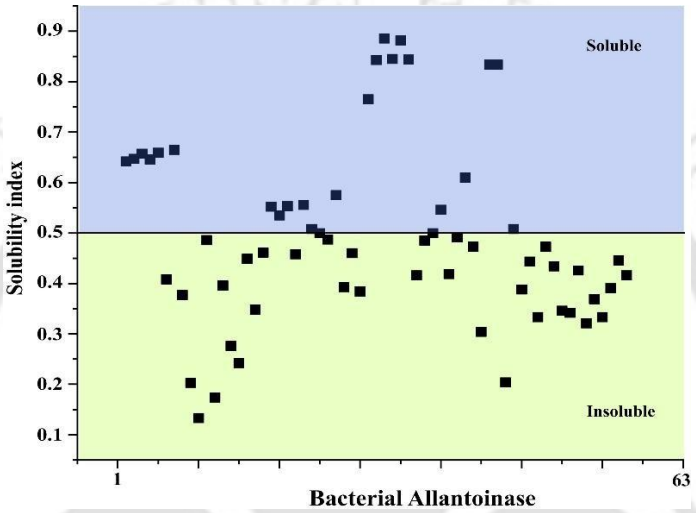

Figure 2.5*:* Solubility index generated for bacterial allantoinase

2.3.4 Insights from amino acid composition.

Box plot visually summarises the amino acid composition and identifies hidden patterns. In Fig. 2.6, the population statistics are depicted, exhibiting a substantial degree of variability and high dispersion for each individual amino acid. The maximum variability was observed in the case of Ala, which imparts minimal steric constraints in the three-dimensional framework. Rare occurrence amino acids (frequency range 0-1) are sulphur containing residues like Cys and Met, and the aromatic residues Trp and Tyr. Hydrophobic amino acids dominant, as indicated by the box-position of Ile, Leu, Asn, and Glu. Non-polar amino acids in high frequency such as Ala, Leu, Gly and Val indicate compactness of the native structure of protein. The distribution of Leu, Glu, and Val in the enzyme sequences features several outliers.

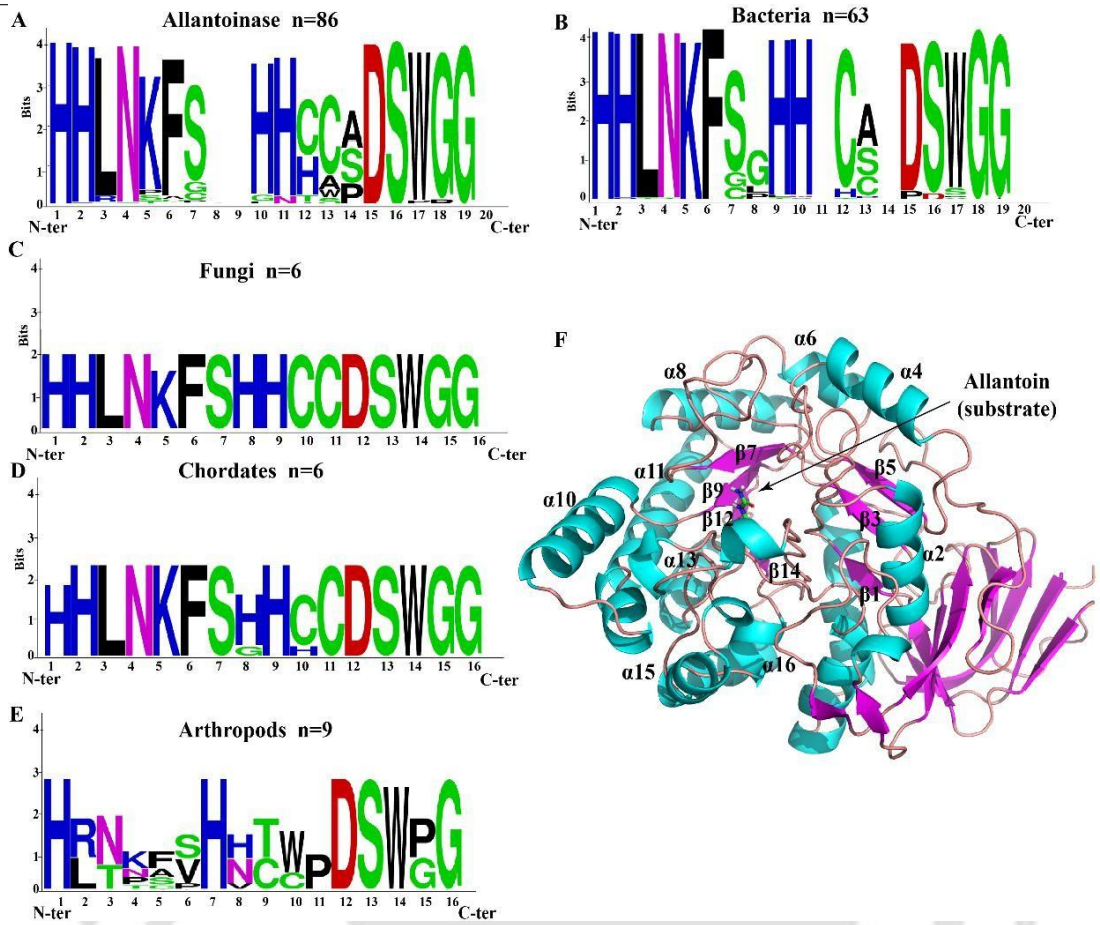

Figure 2.6: Weblogo representing the frequency of amnio acids in the active site of allantoinase. The stack height is indicative of the sequence conservation and frequency of occurrence at the specified position. Representation is shown for (A) allantoinase complete dataset, (B) bacterial (C) fungi (D) chordates and (E) arthropods with 'n' denoting the number of sequences in each clade/taxa. (F) A representative three-dimensional structure of allantoinase (*E. coli* Strain K12) is shown for its secondary structural arrangement, α-helices in cyan and β-strands in magenta.

2.3.5 Sequence-structure analysis focusing on allantoin binding site.

The reported allantoinase structures are typically found in tetramer.[114] However, for the purpose of our three-dimensional architecture analysis, we have chosen to consider only monomers. According to Kim et al. the active site is commonly referred to as TIM-barrel structure due to the arrangement of helices-loop-sheet secondary structures.[110] The substrate allantoin binds to a large cavity in the enzyme consists β-strands, α-helices, and loops. In Fig. 2.6 F, the arrangement of secondary structural patterns in *E. coli* strain K12 is illustrated. The spatial distribution of secondary structures highlights the inner region (active site) containing β-sheets, which are radially covered by the α-helices.

The active site has been further elucidated interpreted through its sequential composition. The frequency of amino acids is delineated on a comparative basis across varying taxa, subsequently visualized through weblogo representation. The empty positions indicate the gap penalty used for the multiple sequence alignment algorithm. The complexity

and diversity of a sequence motif are closely correlated with the size of the amino acid character bins.[141] Fig. 2.6 shows the weblogo for entire dataset, where His and Asn at the N-ter and Gly, Asp, and Ser at the C-ter are conserved, ascribing a common structural/functional role. Gly, in particular, is pivotal as β-strand breaker and involved in providing conformational flexibility to the enzyme active site.[142] Positions 5-7 and 10-14 are partially buried, and populated by Phe, Ala, Thr and Cys, indicating dynamic conservation level across the alignment. The acidic residue Asp, red remains conserved across all the dataset, except in a few bacterial allantoinase (Fig. 2.6 B). Stacking of multiple amino acids, in the 7-8 and 12-13 position, shows its critical role in maintaing flexibility within the active sites, which is pronounced in case of arthopods (Fig. 2.6 E). The least variation in the active site residues were found in case of chordates and fungi, showing high divergence and no strong preference for any particular amino acid. Collectively, all allantoinase contain a conserved aromatic residue Trp, at position 14 or 17, which underscores its criticality in facilitating crucial interactions.

2.3.6 Accounts of allantoinase disorder characteristics

Disordered regions refer to the structural regions that lack a well-defined and stable three-dimensional structure. These regions are often flexible and unstable due to the absence of any specific conformation.[130] This analysis helps estimate the challenges during purification and crystallisation, and also impacts the protein-adsorption process. Focusing on critical regions when stabilizing protein adherence for biosensing applications can significantly extend the protein's functional lifetime and enhance sensing proficiency (Fig. 2.7).

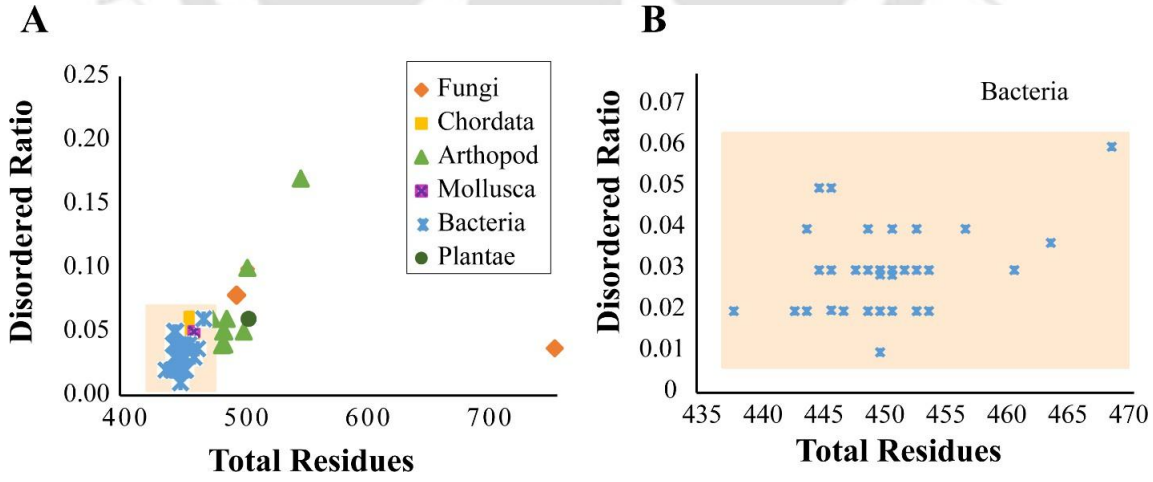

Figure 2.7: Disordered characteristics of all species (b) bacterial species

Bacterial species have the lowest number of disordered regions, likely due to their streamlined genetic material and low sequence complexity (Figure 2.8 A). The disordered ratio for the bacteria ranges from 0.02 to 0.06, with 23 species having a disordered ratio of 0.02 (Fig. 2.7 B). Notably, the highest ratio for disorder is observed for *E. coli* MS 21-1, *Chlorofexota*

bacterium, and *E. fergusonii*, with a value of 0.06.

The extent of disordered regions in allantoinase proteins varies among different taxonomic groups due to several biological and evolutionary factors. Arthropods have the highest average ratio of disordered regions (7%), followed by fungi (6%). While bacterial allantoinase have the lowest average (3%), it highlights the compact three-dimensional structure and thus is a good candidate for immobilization purposes. Interestingly, when correlated with the length of the proteome, the overall percentage and average disorder ratio were also found to be lowest for bacterial origin (Table 2). The difference arises due to specific amino acid sequence features, such as a greater frequency of charged and hydrophilic residues, or low sequence complexity, which are specific to protein disordered areas. Further discussion will focus on the analysis of bacterial proteins with insights from instability index and extinction coefficient.

Table 2: Average disorder ratio in different phylogenetic taxa of allantoinase

	Average disorder	Average ratio (Disorder region/ Proteome size)	Percentage (%) of Disorder region
Fungi	32	0.06	6
Chordates	26	0.06	6
Bacteria	14	0.03	3
Arthropoda	35	0.07	7
All	19	0.04	4

2.3.7 Accessing the stability parameters of bacterial allantoinase.

Instability index is an indicator of protein stability *in vitro*, based on empirical index of amino acids in the sequence.[131] The average instability index estimated for bacterial allantoinase is 36.33, pointing to notable stable. Specifically, 50 bacterial allantoinase sequences with values <40 is considered stable, while the remaining 13 show values >40 (Fig. 2.8 A). *Escherichia* and *Streptomyces* species emerge as promising candidates for developing allantoinase-based sensor due to their high acceptance rate in laboratory-scale expression yield. Evaluation from *Streptomyces* species, reveals an average index of 37, with a marginal exception of *S. ferrugineus* (value 41). Conversely, the enzyme from *Escherichia* species yields a slightly higher average instability index of 42. Despite exceeding the 40 thresholds, the associated instability can be effectively controlled during routine protein purification and isolation protocol.[143]

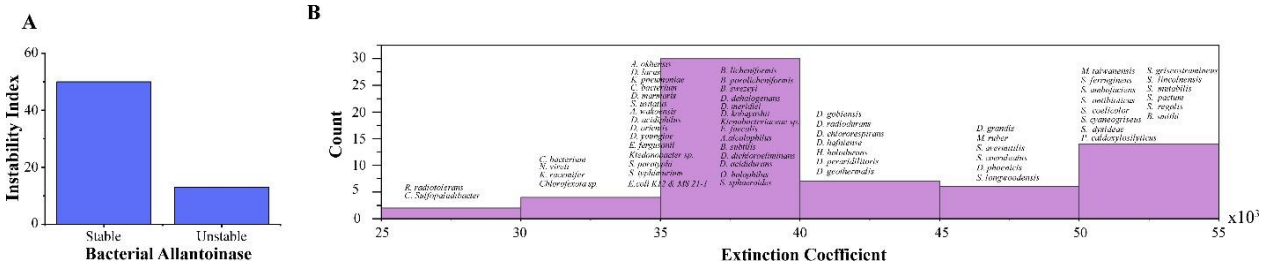

Figure 2.8 (A) Instability Index (B) Extinction Coefficient

2.3.8 Representation of allantoinase's structural models

Structural ensembles from diverse taxonomic groups are overlaid to obtain insights into secondary structural content and resemblance. Notably, a distinct demarcation between potential disordered regions (blue) and the active site (green) of the protein is evident in Figure 2.9. Of particular interest is the qualitative alignment between bacterial and chordate taxa. The disordered regions are mostly conserved in the central segment of primary sequences, but are also confined to a distinct peripheral region of the enzyme, with an exposed surface. Furthermore, additional disordered regions located on the C-ter region are clearly separated from the active site. This crucial insight aids to our understanding that the presence of disordered regions or the associated conformational alternation does not hinder the enzyme's ability to adsorb on surfaces. Importantly, the specificity and sensitivity of the protein upon adsorption remain unaffected, given the spatial separation of the active site from the disordered region.

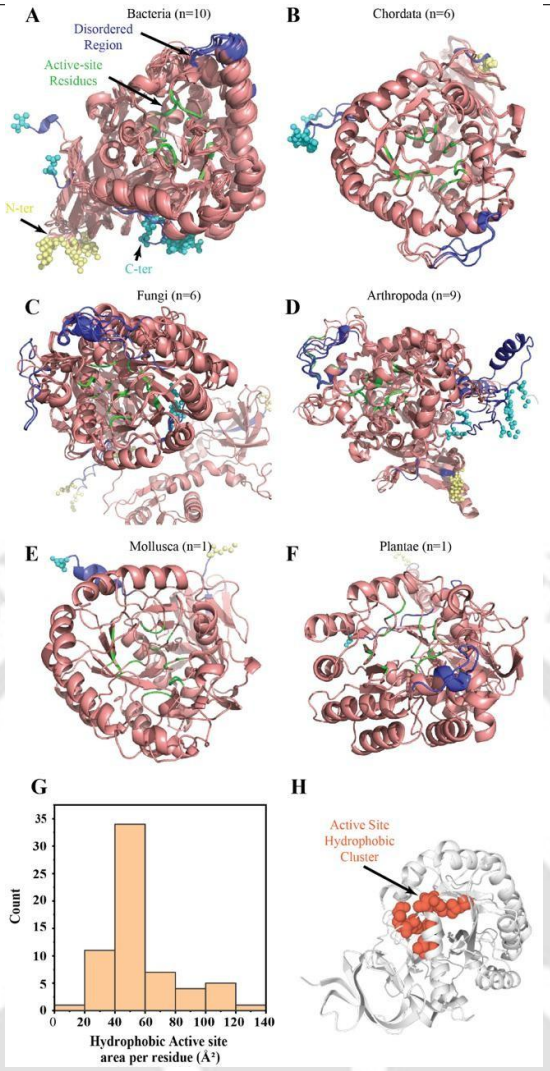

Figure 2.9: structural models of allantoinase showing the disorder regions (blue) and active binding sites (green). The N-ter (pale yellow) and C-ter (cyan colour) of the structures are represented as sphere. The number of structural models used in this representation are denoted as 'n'. The indicative structural models represent (A) Bacteria (n=10) (B) Chordates (n=6) (C) Fungi (n=6) (D) Athropoda (n=9) (E) Mollusca (n=1) (F) Plantae (n=1). (G) Histogram representing area of hydrophobic active site. (H) Visual representation of 3D structure of allantoinase showing hydrophobic cluster in the active site region

In Fig. 2.9 G, we presented a statistical analysis of the hydrophobic patches present on the surface of the allantoinase, offering significant insights into enzyme stability. Certain bacterial species, such as *Desulfitobacterium* sp., *Streptomyces* and *R. radiotolerans*, exhibit pronounced hydrophobic residues-rich areas near the active site. The occurrence of these hydrophobic amino acid residues near the active site significantly impacts substrates and products accessibility, potentially influencing the catalytic activity. These hydrophobic regions can create intricate pockets and channels, thereby affecting molecules access to the catalytic center [130]. Utilizing these interactions through immobilization methods holds promise for preserving the enzyme's catalytic activity across various conditions. Additionally, visual

representation of the hydrophobic clusters near the active site region can be found in Fig. 2.9 H.

2.3.9 Insights into the intrinsic volume.

Protein folding is the fundamental aspect that regulates the structure-function relationship. We focused on analyzing the packing pattern of allantoinase and identified correlations between the driving forces essential for the enzyme's conformational stability, thermostability, and ligand binding. This information could also underpin our understanding of effects of mutations and prediction of stability parameters. In Fig. 2.11 (C), various regression analysis for the V_{vdW} and V_{void}, which together constitute the total intrinsic (V_{total}) volume are presented as explained in Fig. 2.10. In Fig. 2.11 A, the analysis of V_{total} in relation to the protein length displayed a strong regression (Pearson's R and R^2 as 0.94 and 0.89). However, when focusing solely on bacterial allantoinase, no significant correlation was observed, suggesting that the enzymes from other taxa with extended and flexible regions demonstrate a strong correlation with the increased sequence length. The regression for V_{total} with V_{vdW} and V_{void} is significant for the data set. Pearson's R value for V_{total} vs V_{vdW} remains 0.99 when calculated for all the proteins and bacteria Fig. 2.11 B. For V_{total} vs V_{void} Pearson's R changes slightly from 0.97 (all dataset) to 0.92 for bacterial (Fig. 2.11 D). This implies that bacterial allantoinase exhibit variation in intrinsic volume due to differences in V_{void}. Additionally, the regression between V_{vdW} and V_{void} for all proteins with R^2 value of 0.91, while for bacteria it reduced to 0.74.

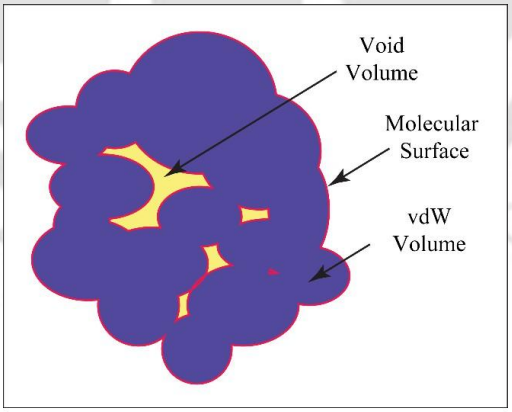

Total Volume = vdW + Void volume

Figure 2.10: Visual representation of the intrinsic volume parametersVarious factors influence how protein adsorb to a substrate surface, including the chemical and physical properties of both the protein and the material surface. Van der Waals forces are considered to be significantly involved in the adsorption of proteins onto materials such as graphene, Silica, or other low-dimensional materials.[144] Unfolded proteins are more susceptible to

changes in ionic strength and, therefore, are more influenced by vdW forces than folded proteins. Therefore, understanding the intrinsic volume parameters influencing the folding state of allantoinase is crucial. It has also been suggested that a combination of electrostatic interaction, counterion release, and vdW forces are necessary to explain the binding behaviour of Proteins.

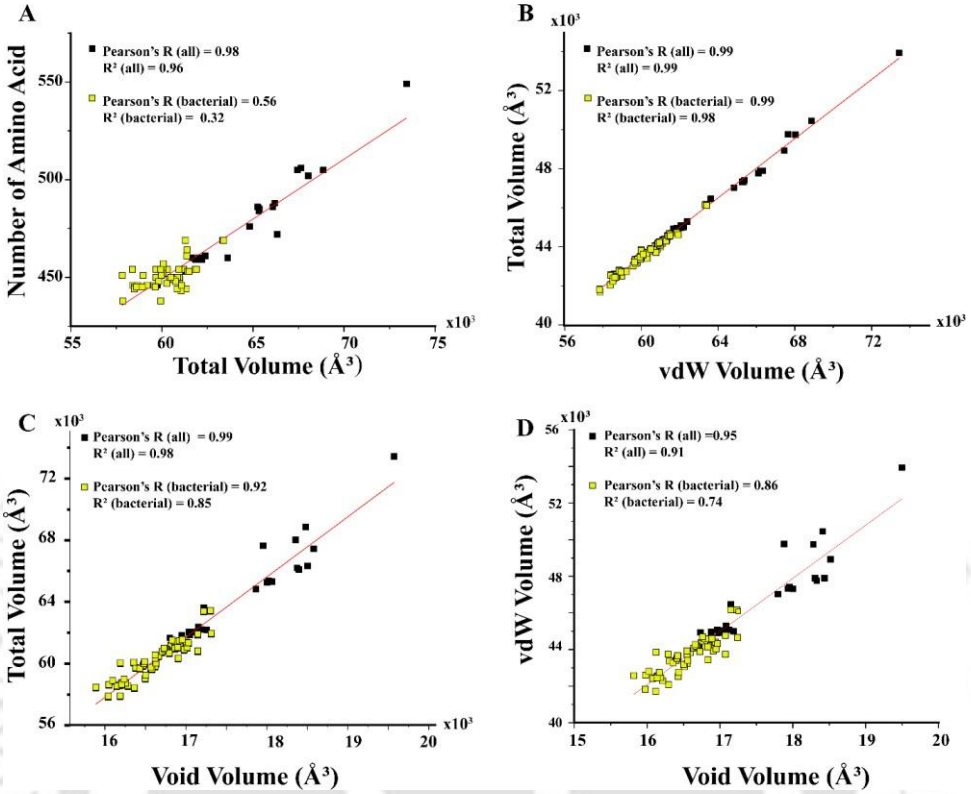

Figure 2.11: Volume-based parameter analysis of allantoinase. (A) Correlation between V_{total} and Proteome size. (B) Correlation between V_{total} vs V_{vdW} (C) Correlation between V_{total} vs V_{void} (D) Correlation between V_{vdW} and V_{void}

2.3.10 Structural characteristics based on solvent accessibility.

SASA analysis, essential for understanding the surface-proximal regions and estimating the sensor's stability, particularly after its adsorption to the surface. A strong correlation between SASA and proteome size for all proteins (R=0.95), and for bacterial allantoinase (R=0.74) in Fig. 2.12(A-C) is shown. Specifically, bacterial allantoinase has a SASA volume range of ca. 15500 and 18700 $Å^2$ (Fig. 2.12 B), the lowest across different taxa, with *Streptomyces* sp. showing the lowest extrinsic SASA. This indicates better residue burial, enhancing stability by lowering hydrophobic residue exposure. As discussed in the work by Marsh, SASA denotes the extrinsic area property, closely linked with the intrinsic properties like V_{vdW}, V_{void}, and hydrophobic surface.[145] Furthermore, strong regression values with R^2 of 0.94 and 0.91 for V_{vdW} and V_{void}, respectively (Fig. 2.11), underscores the protein's adaptability to environmental changes without perturbing enzyme's performance.

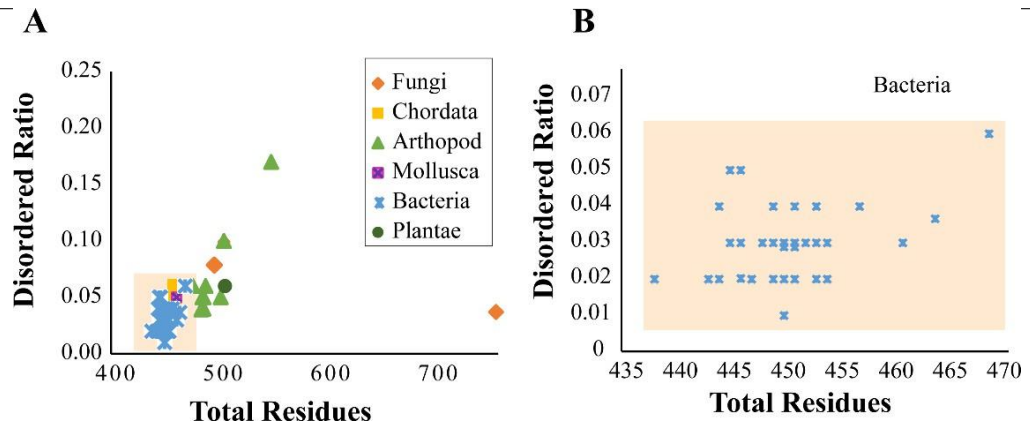

Figure 2.12: Stability analysis of allantoinase. (A) SASA of all clades. (B) SASA of bacterial allantoinase

2.3.11 Estimates of hydrophobicity and structural compactness

To elucidate the determinants of protein stability and function, we consider critical metrics like Hydrophobic indices to characterize a protein's hydrophobic,[134] and Long Range Order (LRO) to estimate the spatial arrangement of distally located residues that stabilize the protein 3D shape.[146] The calculations are based on pairs of residues that are 12 or more residues in sequence but within a spatial distance of 8 Å.[147] LROs are relevant for understanding the extent of local perturbation resulting in an unfolded conformation. Our analysis reveals that *O. halophilus* exhibits the highest Hp value at 35.27, which indicates its higher propensity for hydrophobic interactions (Fig. 2.13 A), integral to minimize the solvent-induced structural perturbations. In contrast, *R. radiotolerans* displays markedly lower Hp at 22.97. Among the bacterial allantoinase, *Alkalihalobacillus sp.* has the highest total LRO of 0.38 and *R. radiotolerans* has the lowest at 0.073 (Fig. 7E). A robust correlation between LRO and Hp (Pearson R=0.94) (Fig. 2.13), underscores the interdependence between protein's hydrophobic profile and compactness. Other strong correlations have been established between the hydrodynamic parameters of allantoinase, indicating compactness and structural stability

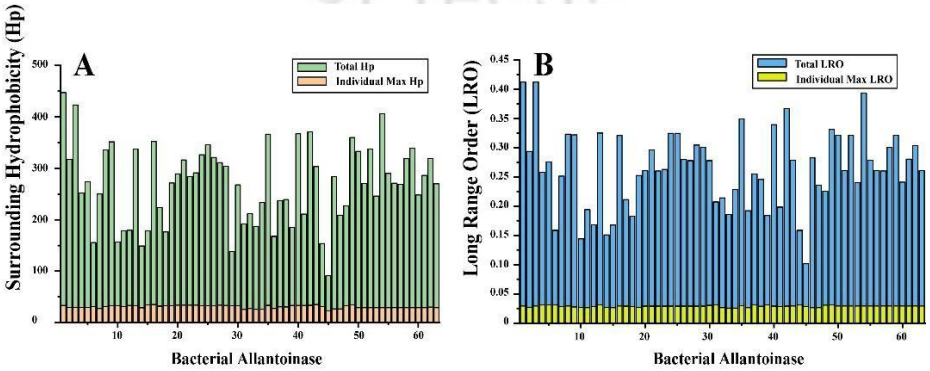

Figure 2.13: (A) LRO of bacterial allantoinase (B) Correlation between LRO and Hp

2.3.12 Spatial conformational distribution and degree of freedom.

The distribution of protein fold across the center of mass provides insight into its compactness and overall dynamics.[148] It was also foundn that the average value of Rg for the entire dataset is ca. 21, indicating that the overall spatial conformational distribution is assymmetric. The findings are visually depicted in the box plot in Fig. 2.14 B, where median values of 24.3 for Ro and 21.3 for Rg, indicates the tightly packed 3D structure (Rg < Ro). Notably, an outlier for Rg at 24.2 was observed, associated with *E. coli* MS21 allantoinase.

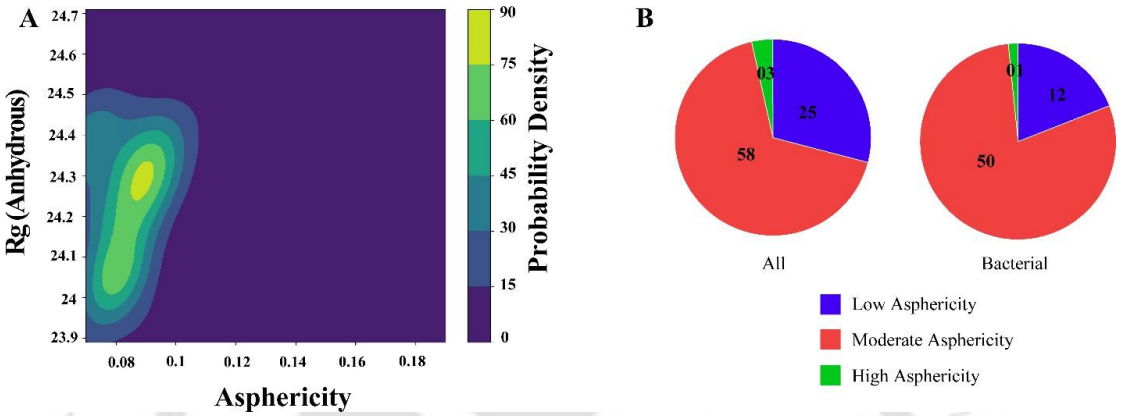

Figure 2.14: (A)Two-dimensional density plot between Asphericity and Rg (B)) Pie chart of Asphericity of complete and bacterial allantoinase

Protein's asphericity indicates how its shape deviates from a perfect sphere, which is vital in determining the functional and stability. Asphericity values range from 0 for a perfectly spherical shape to 1 for an irregular shape. Through a 2D density map correlating Rg and asphericity, we pinpoint proteins sharing similar size properties. A large portion of the dataset shows density >60% and indicates that the majority of allantoinases demonstrate close to zero asphericity. To obtain deeper insights, as shown in Fig. 2.14 B, notably, 97 % of allantoinase in the dataset ranges between low to moderately (up to 0.11) asphericity, indicating minimal deviation from a perfect sphere. Interestingly, all bacterial allantoinases (except *S. paratyphi*), show low asphericity, which demonstrates they are less susceptible to structural perturbations caused by solvent interactions, rendering more stable during adsorption.

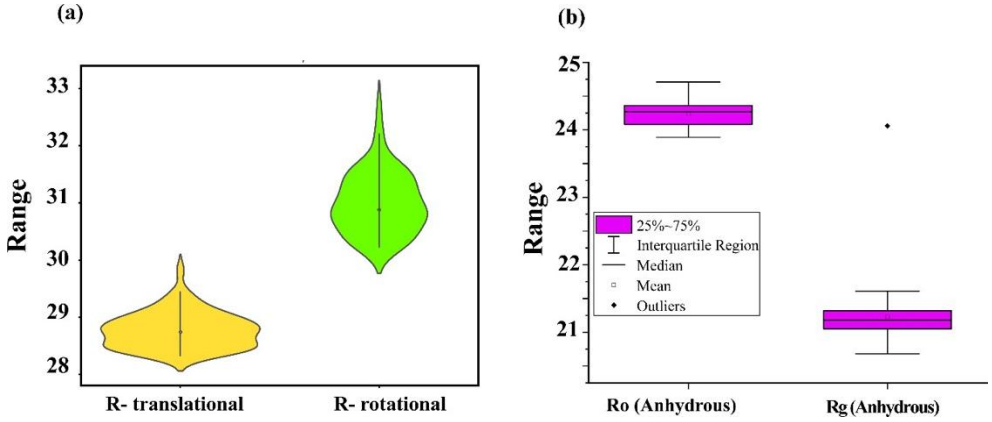

Figure 2.15: (a) Violin plot of Rtranslational and Rrotational parameters among the bacterial allantoinase. (b) Box plot to show the range of Ro and Rg

We also elucidated the translational and rotational radii of allantoinase, to gain insights on the protein dynamics that governs its interaction property. In highly diluted solutions, the rotational and translational diffusion coefficient and the Ro of the biomolecule, temperature and the solution's viscosity (η), are related through the Stokes-Einstein-Debye and Stokes-Einstein (SE) equations. Physically the phenomenon of Brownian or stochastic motion in solvents, depict the interplay of frictional forces and torque captured by the translational and rotational radii, respectively. Our findings are illustrated in violin box plots in Figure 2.14 A, highlighting the variation in R-rotational ranging from 30-32, while the R-translational demonstrates relative stability from 28-30. One key realization from this analysis is that although the allantoinase globular-folded size remains compact, its susceptibility to mass distribution leads to notable variance in the R-translational radii. This observation sheds light on the protein's propensity to spread out, which is uncovered during Brownian motion, as indicative by relatively higher R-rotational radii. Additional parameters such as translational diffusion coefficient (Dt) and frictional coefficient (f/fo). These critical estimates ensures that the immobilized enzyme maintains its structural integrity, preserving catalytic efficiency.[149]

2.3.13 Multivariate analysis on the derived features from different species.

The PCA performed on 16 features derived for 63 species producing allantoinase, resulted in the following scores and the loading obtained for the first two principal components (PC) as shown in Biplot (Fig. 2.16). The clustering based on scores of PC I & II, resulted in 5 distinct clusters and some individual species that could not be clustered were represented as outliers (Table 3). Though many of the species from same genus are grouped together such as *Streptomyces* in group V, we also see distribution of same genus into different groups, e.g. Bacillus into group I, II; *Deinococcus* into group III, IV and VI. Another interesting aspect of the Biplot is that the features responsible for the clustering of group I such as Asphericity (F8), Total Volume (F9), Void Volume (F10), exhibited higher value compared to other species. Similarly, we also note that, Total Hp (F4) seems to be down regulated in Group III, which is the reason why its corresponding loading vector is pointed away (opposite direction) from its cluster. The implication of PCA is that, it provides multiple options to choose a species with desired feature characteristics from a pool of clustered species.

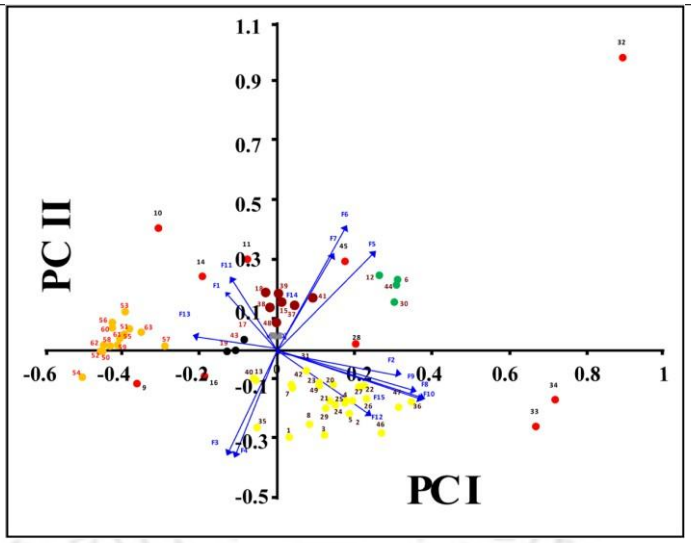

Figure 2.16: Principal Component Analysis of allantoinase species. The scores are shown in filled circles, and the loading vectors are shown in blue arrows. The clustering of the score plot was performed using dbscan algorithm. The resulting clusters were named as, Group I (•), Group II (•), Group III (•), Group IV (•), Group V (•) and Group VI (•)

Table 3: The species present within each cluster or group obtained from the dbscan clustering based on the score values of PCA

Group I	Group II	Group III
A. alcalophilus *A. okhensis* *A. wakoensis* *B. licheniformis* *B. paralicheniformis* *B. swezeyi* *B. subtilis* *D. geothermalis*	*B. smithi* *C. bacterium* *D. kobayashii* *P. caldoxylosilyticus*	*D. grandis* *D. phoenicis* *K. racemifer* *Ktedonobacter sp.* *K. bacterium* *M. taiwanensis* *S. usitatus*
D. chlororespirans *D. dehalogenans* *D. dichloroeliminans* *D. hafniense* *D. acididurans* *D. acidiphilus* *D. lacus* *D. meridiei* *D. youngiae* *E. faecalis* *H. halodurans* *K. pneumoniae* *M. ruber* *N. vireti* *S. paratyphi* *S. typhimurium* *S. sphaeroides*		
Group IV	Group V	Group VI (outliers)
D. peraridilitoris *D. radiodurans* *O. halophilus*	*S. ambofaciens* *S. antibioticus* *S. avermitilis*	*C. Sulfopaludibacter* *C. bacterium* *C. bacterium*

	S. caeruleatus *S. coelicolor* *S. cyaneogriseus* *S. dysideae* *S. ferrugineus* *S. griseostramineus* *S. lincolnensis* *S. longwoodensis* *S. mutabilis* *S. pactum* *S. regalis*	*D. gobiensis* *D. marmoris* *D. orientis* *E. coli MS 21-1* *E. coli strain K12* *E. fergusonii* *R. radiotolerans*

2.4 Conclusion

In this comprehensive study, allantoinase enzymes from 86 different sources were thoroughly evaluated to determine their biochemical and biophysical properties, with aim of ranking their suitability for immobilization. Notably, a significant majority (73%) were originating from bacterial origin. When it comes to developing enzyme-based sensors, properties such as solubility, structural compactness, hydrophobic area, and hydrodynamic attributes must be thoroughly considered. The information is essential for precise engineering of enzymes with specific mechanical, biochemical, and kinetic properties to achieve unparalleled sensitivity for analyte detection and long-term sensor stability against environmental perturbations.

Our analysis elucidates the relationship between environmental pH and its propensity to enhance adsorption to counter-charged substates. It sheds light on properties of allantoinase, where its intrinsic hydrophilic nature, underscored by a negative hydropathy index. Notably, bacterial allantoinase reveals diminished disorder ratio alongside high stability, primarily due to the Cys residue which favour disulfide bonds with substrates. However, only 40% of the bacterial allantoinase was observed to meet predefined solubility threshold.

The active site of the enzyme, characterized by conserved titratable residues such as His and Asp, plays a pivotal role in retaining enzymatic activity through pH dependent (de)ionization, within the specific buffer range. Moreover, bacterial allantoinase is least prone to environmental perturbations attributed to its stable tertiary structure. This stability is further enhanced by significant hydrophobic active site area per residue and lower SASA. Further, *Escherichia* and *Streptomyces* show superior values for stability index and extinction coefficient, suggesting them as strong candidates for adsorption suitability. Similar compelling correlation between intrinsic volume and protein length for bacterial allantoinase indicate its compact folding pattern in contrast to other taxa. Based on analysis of hydrodynamic parameters such as Rg, Ro, asphericity, Dmax, and frictional coefficient, bacterial allantoinase shows a more uniform and spherical shape, which is highly desirable for optimal adsorption

onto surfaces. The theoretical estimates offer significant advantage, providing a cost-effective and readily accessible alternative to traditional experimental validations such as Analytical Ultracentrifugation (AUC), Size-Exclusion Chromatography (SEC), Nuclear Magnetic Resonance (NMR), and Small-Angle X-ray Scattering (SAXS), which may be limited in their applicability to polydisperse samples.[150]

Enzyme-based sensors face challenges like sensitivity to process conditions and reduced stability. Improving enzyme stability and simplifying recycling and processing are critical for enzyme immobilization. This study provides valuable insights by analyzing structural parameters, aiding in selecting the promising species for the physical adsorption and immobilization methods. These parameters are crucial for developing effective sensors in various settings

Chapter 3

Analysis of Agarose Gel Electrophoresis and Pore Size Characterization

Abstract

Agarose gel electrophoresis is a fundamental technique used for the separation and analysis of nucleic acids based on their size and conformation. This separation mechanism relies on the porous network formed by agarose polymers, which acts as a molecular sieve under an applied electric field. Understanding the relationship between gel microstructure and DNA migration behavior is essential for accurate interpretation of electrophoretic results. In this chapter, agarose gel electrophoresis data were quantitatively analyzed using image-based methods, and the pore size characteristics of the agarose gel matrix were examined using scanning electron microscopy (SEM). The combined analysis provides insight into how gel microstructure correlates with DNA band mobility and intensity. The quantitative relationship established between agarose pore morphology and DNA migration provides broader insight into biomolecular transport in porous hydrogel matrices. Such understanding is directly relevant to the design of hydrogel-based biosensing platforms, where analyte diffusion, binding interactions, and signal generation are strongly governed by the underlying network microstructure.

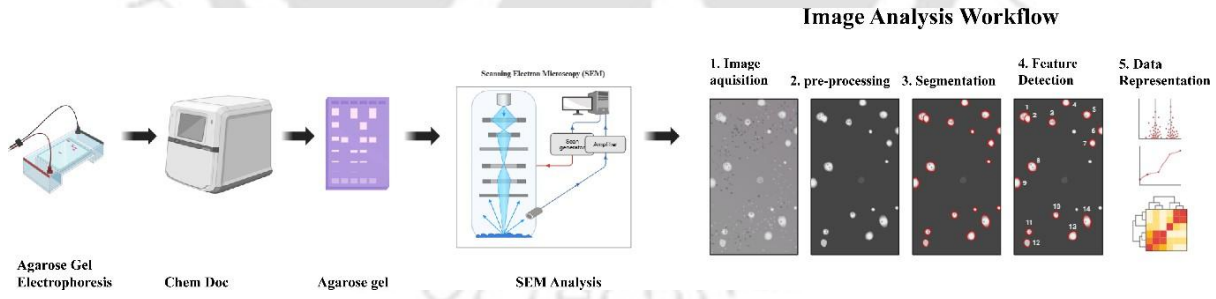

Figure 3.1: Schematic of agarose gel imaging and SEM analysis followed by image processing and quantitative feature extraction workflow. This work has been published in:

Kotal, A., **Das, S.**, Sarangi, S., Das, N., & Kar, R. K. (2025). Image Analysis for Analytical and Microbial Studies. Journal of Chemical Education, 102(4), 1684-1693.

3.1 Introduction

Agarose gel electrophoresis is one of the most widely used analytical techniques in molecular biology for the separation, visualization, and semi-quantitative analysis of nucleic acids. Its popularity originates from its operational simplicity, low cost, and high resolving power for DNA fragments across a broad size range. In an applied electric field, negatively charged DNA molecules migrate through a hydrated network of agarose fibers, and their mobility is primarily governed by size, conformation, and the physicochemical properties of the gel matrix.[151] Agarose gels are often used as routine lab tools without much thought, but their internal structure, especially the size and distribution of pores, strongly influences how molecules move during electrophoresis and therefore affects the accuracy of results.[152]

The gel matrix formed by agarose is a physically crosslinked porous network created upon cooling of hot agarose solutions. Linear agarose polymers self-associate via hydrogen bonding and hydrophobic interactions to generate double helices, which further aggregate into superhelical bundles and three-dimensional networks.[153] The interstitial voids within this network constitute the pores through which hydrated DNA molecules must traverse under an applied electric field. These pores act as a molecular sieve that imposes steric constraints and solid friction on migrating DNA. As a result, larger DNA fragments experience greater hindrance and migrate more slowly, while smaller fragments can navigate the porous network more efficiently, leading to size-dependent separation. The effective sieving characteristics of an agarose gel therefore depend critically on parameters such as pore diameter, pore connectivity, tortuosity, and heterogeneity of the microstructure.

In practical terms, the performance of agarose gel electrophoresis is typically evaluated in terms of resolution, band sharpness, migration reproducibility, and the accuracy of size estimation relative to known standards. These macroscopic performance indicators are influenced by several experimental variables, including agarose concentration, buffer composition, ionic strength, applied voltage, gel thickness, and temperature. Among these, the concentration and microstructure of the agarose matrix are especially important because they directly modulate the pore size distribution and mechanical rigidity of the gel. Higher agarose concentrations generally yield smaller pores and increased gel stiffness, improving resolution for small DNA fragments but simultaneously impeding the migration of larger molecules. [146]Conversely, lower agarose concentrations generate larger pores, facilitating the migration of high-molecular-weight DNA at the expense of resolving power for smaller fragments. A rigorous understanding of the relationship between gel microstructure and DNA migration behavior is therefore essential for the rational design and optimization of electrophoretic

separations.[154]

The characterization of agarose gel microarchitecture has historically lagged behind standard electrophoretic applications, despite the crucial role that pore structure plays. Instead of using quantitative structural data, agarose concentration and buffer conditions are chosen empirically in many labs using empirical charts or acquired experience. These methods are less effective when high resolution separations, reliable quantitative interpretation, or technique transferability are needed, even if they frequently function well for typical diagnostic or cloning procedures. For instance, minute changes in the polymer batch, gel aging, or gel casting circumstances might change the effective pore network, resulting in variability in DNA migration from gel to gel or lane to lane.[155] It is challenging to determine whether variations in band mobility or intensity are due to biological variation, mistakes in sample preparation, or inherent heterogeneities in the gel matrix without direct knowledge of the underlying microstructure.

At the same time, with the right sample preparation, electron microscopy techniques, especially scanning electron microscopy (SEM), can be used to directly visualize the agarose network. High resolution imaging of the dried network is made possible by freeze drying or critical point drying agarose gels, which is followed by conductive coating.[156] This allows for the visualization of the fiber architecture and the distribution of pores at the nanoscale. Through systematic image analysis of SEM micrographs, quantitative parameters such as pore diameter and pore area distributions can be extracted. These structural metrics, when coupled with electrophoretic performance data, provide a powerful framework for establishing structure–function relationships in agarose gels. In particular, they enable direct assessment of how mean pore size, distribution width, and the presence of rare larger voids influence DNA mobility, band separation, and lane-to-lane reproducibility.[157]

The present chapter adopts such a combined electrophoretic and microstructural approach to investigate the role of agarose gel pore morphology in governing DNA migration behavior. Agarose gels of defined composition are prepared under controlled conditions, and DNA fragments are separated using standard horizontal electrophoresis. High-resolution gel images are acquired and analyzed using ImageJ to extract band positions, calculate percentage relative mobility, and quantify band intensities in different lanes.[158] These metrics provide an objective measure of the extent and reproducibility of size-dependent separation, as well as the consistency of DNA loading and the degree of diffusion-related losses.[159] Particular attention is given to comparing relative mobility and intensity profiles between lanes containing identical DNA mixtures, thereby probing the uniformity of the gel

matrix and the applied electric field.

It was mmobilized immediately after preparation, rapidly frozen, and subjected to freeze-drying under vacuum to minimize structural collapse and preserve the native network architecture as closely as possible. The dried gels are then sputter-coated with a thin conductive layer and imaged at high magnification to resolve the fiber network and pore morphology. Image analysis software is used to identify individual pores, measure their diameters, and calculate their areas, yielding statistical distributions of pore size and pore area. The resulting histograms are further analyzed using Gaussian fitting to estimate mean pore diameters and assess the width and symmetry of the size distribution. These data enable characterization of the gel matrix in terms of both its predominant pore scale and the degree of heterogeneity arising from the presence of smaller and larger pores.[153]

This work attempts to clarify how microscopic characteristics of the agarose network translate into macroscopic electrophoretic performance by combining these two complimentary datasets: quantitative pore structure metrics from SEM and quantitative DNA migration metrics from gel electrophoresis. The mean pore size determined from SEM is interpreted in the context of the observed range of DNA fragment mobilities, providing physical justification for the size-dependent separation. At the same time, deviations from ideal, perfectly uniform pore structures, as reflected in skewed pore area distributions and occasional larger voids, are related to the minor variations observed in band mobility and intensity between identically loaded lanes. In this way, the chapter establishes a direct correlation between pore size distribution characteristics and the reproducibility and resolution of DNA separation.[153]

This integrated perspective is not only of fundamental interest for understanding molecular sieving mechanisms in agarose gels, but also has practical implications for method optimization and standardization. Reliable knowledge of pore size scales and heterogeneity can guide the rational selection of agarose concentration for specific size ranges of DNA, inform the choice of buffer conditions and applied fields, and aid in diagnosing unexpected changes in electrophoretic behavior. Furthermore, the quantitative framework developed here combines image based electrophoretic analysis with SEM derived microstructural characterization and can serve as a useful approach for studying other gel systems, including polyacrylamide, composite gels, and emerging polymer matrices used in microfluidic and lab on a chip platforms.

A broader implication of this work lies in the growing reliance on imaging as a

quantitative analytical tool rather than a purely descriptive technique. Understanding gel microstructure and electrophoretic behavior ultimately depends on extracting reliable numerical information from visual datasets, linking structural characterization with functional performance. This highlights the central role of systematic image acquisition, processing, and analysis in modern scientific workflows, where translating visual observations into reproducible metrics enables deeper interpretation across biological, chemical, and materials research contexts.

Image-based information is vital in the scientific domain, providing a valuable perspective for understanding and analyzing complex phenomena. Deriving quantitative conclusions from visual data is essential. Key features of images such as size, shape, intensity, and spatial distribution contain important insights that significantly enhance our scientific understanding of various problems.[157] However, effective interpretation often requires thorough processing, including enhancing image contrast, improving resolution, segmenting specific areas, and highlighting regions of interest. Herein, it is important to track these processes, maintain transparency, and accurately reproduce the information extracted from multidimensional imaging data. Ultimately, achieving a high level of accuracy, sensitivity, and precision in image interpretation is crucial for advancing scientific knowledge.

The significance of image-based analysis in biological fields is undeniable, particularly for electrophoresis gel images and fluorescence images obtained from confocal microscopy.[160] These techniques are crucial in phase-contrast microscopy and immuno-histopathological contexts, where aspects such as staining, cell density, and spatiotemporal location play vital roles in accurate assessment.[161] Furthermore, insights gained from imaging methods extend to interdisciplinary areas such as nanotechnology and biomedical engineering. For instance, FE-SEM (field emission scanning electron microscopy) and FE-TEM (field emission transmission electron microscopy) for material characterization are essential in determining size distribution, aspect ratio, and morphological features.[162] Additionally, while less commonly employed, analyses of pore sizes and surface morphology through methods like profilometers and metallography are equally significant. Thus, the concept of image processing is critical for advancing research and innovation across disciplines.

ImageJ is a leading open-source program based on the Java platform, specifically created for scientific image analysis, which was originally developed by NIH.[163] The algorithm provides remarkable capabilities such as intuitive image visualization, segmentation, tracking, and statistical results.[153] The software is continuously updated with new processing protocols,

analysis macros, and plug-ins being integrated routinely.[164] Each update undergoes rigorous validation through peer-reviewed publications, ensuring a high level of accuracy and reliability across fields, including biology,[165] chemistry,[166] and materials science.

In summary, this chapter focuses on the analysis of agarose gel electrophoresis and pore size characterization to uncover the structure–function relationship between gel microarchitecture and DNA migration. The first part of the chapter describes the preparation of agarose gels, the electrophoretic separation of DNA, and the quantitative image-based analysis of band mobility and intensity. The second part presents the preparation of agarose gels for SEM, the acquisition of high-resolution micrographs, and the quantitative extraction of pore size and pore area distributions. Finally, the electrophoretic and morphological results are correlated to demonstrate how the nanometer-scale porous network of agarose underlies the observed macroscopic electrophoretic performance. Through this comprehensive approach, the chapter provides a robust framework for understanding and ultimately controlling DNA transport in agarose-based separation systems.

3.2 Methodology

3.2.1 Preparation of Agarose Gel

Agarose gel was prepared by dissolving analytical-grade agarose powder in 1× electrophoresis buffer (TAE) to obtain the desired gel concentration. The solution was heated until complete dissolution, yielding a clear and homogeneous melt. The molten agarose was cooled to approximately 55–60 °C and poured into a gel casting tray fitted with a comb to form wells. The gel was allowed to polymerize at room temperature for 30–40 min before use as well mentioned in the paper.

3.2.2 DNA Sample Preparation and Electrophoresis

DNA samples were mixed with loading dye prior to electrophoresis. The solidified gel was placed in an electrophoresis chamber filled with 1× running buffer, ensuring complete submersion. Samples were carefully loaded into the wells, and electrophoresis was performed under a constant DC voltage. Negatively charged DNA fragments migrated toward the anode through the agarose gel matrix according to their size and conformation. Following electrophoresis, the gel was stained using an appropriate nucleic acid stain and visualized using a gel documentation system. High-resolution images were acquired for quantitative analysis.

3.2.3 Image-Based Quantification of DNA Bands

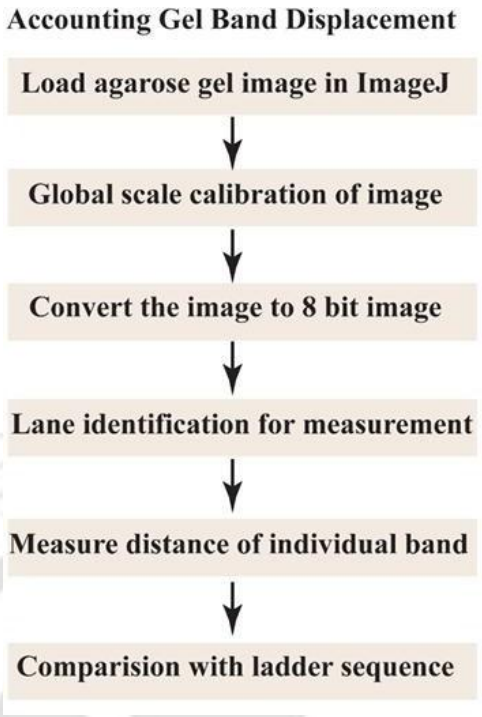

Figure 3.2: Stepwise approach to assess gel band displacement.

After loading the image into the ImageJ software, the image was calibrated using a known scale. This calibration was applied to the entire image. "Set Scale" was selected under the "Analyze" menu, and the known distance was input to establish the pixel-to-length ratio. This step standardized the image for accurate distance and size measurements. The image was then converted to 8-bit to reduce memory usage. The length from each well to the bands was measured, recording the distance for each band by starting from the same reference point for consistency. This step was repeated for all bands in the gel, and the data were saved simultaneously for comparison.

DNA band migration and intensity were quantified using ImageJ software. The Gel Analyzer tool was used to define individual lanes and detect band positions. Migration distance for each band was measured from the loading well to the band center. Relative mobility (Rf) was calculated by normalizing each migration distance to the dye-front migration distance and expressed as percentage relative mobility. Band intensity was determined by integrating the pixel intensity within each band area after background subtraction. These values were used to compare relative DNA abundance between lanes and assess experimental reproducibility.

3.2.4 Analysis of gel band intensity

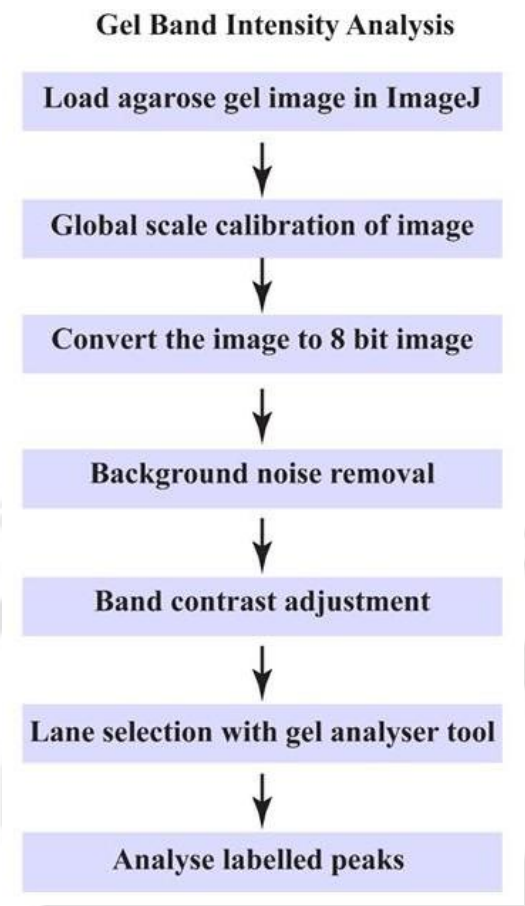

Figure 3.3: Sequential process for analyzing gel band intensity

To calculate the gel band intensity, after loading the agarose gel image, the image was converted into an 8-bit type to reduce the file size. One of the critical steps was the removal of background noise by using the "subtract background" function under the "Process" menu. The rolling ball radius or other parameters were adjusted accordingly to reduce noise while effectively preserving the bands. Alternatively, manual thresholding was performed to eliminate background noise. The gel analyzer tool in ImageJ was used to specifically analyze bands in the gel, helping to select lanes and analyze their gel intensity areas. This created a graph where the peaks corresponded to the bands on the gel. Each peak represented a band and was labeled accordingly. Then, the area under the peaks was determined to measure the intensity of each band, reflecting the concentration of DNA in that band.

3.3 Results and discussion

3.3.1 Quantification of Relative Mobility

To quantify DNA migration, the Gel Analyzer tool of ImageJ was employed to measure the displacement of individual DNA bands from the loading well. The relative mobility (Rf) was calculated and expressed as a percentage of the total migration distance. In

Fig. 3.4 (A), the gel documentation (gel doc) image clearly shows four distinct lanes, each approximately 1 mm in width.[167] Among these, lanes 2 and 3 display ten well-resolved DNA fragments of varying sizes. These visible banding patterns represent the separated DNA fragments that have migrated different distances through the agarose matrix under the influence of the electric field. The clarity of the bands indicates a well-optimized gel concentration and electrophoresis condition, ensuring effective separation and minimal smearing. Such well-defined bands are essential for quantitative analysis, as they directly correspond to discrete DNA fragment populations present in the sample.

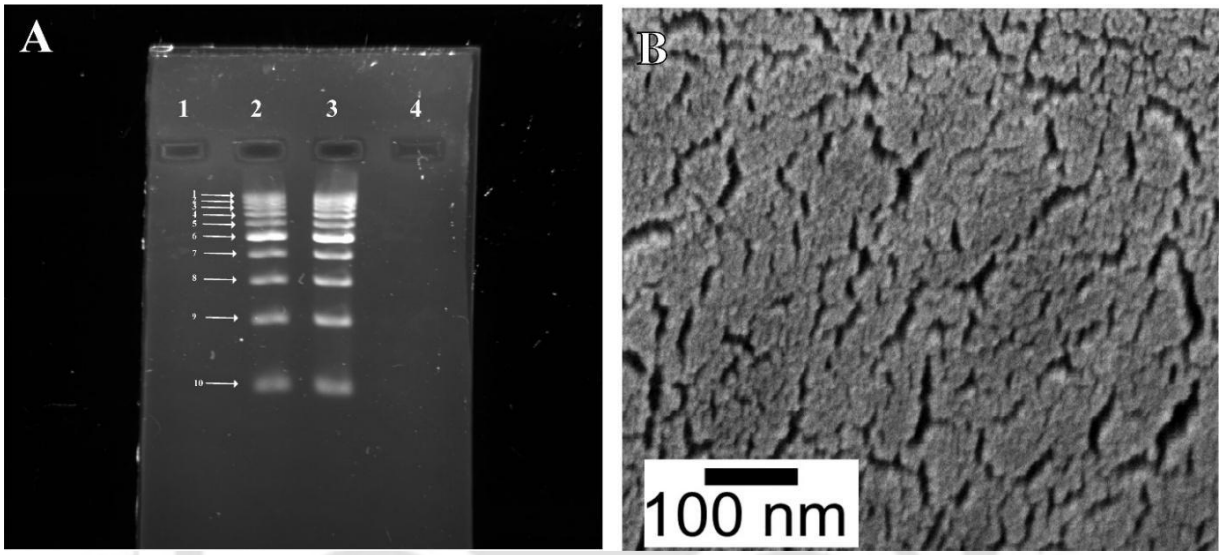

Figure 3.4: (A) shows the gel documentation image of an agarose gel containing four lanes, each with a width of approximately 1 mm. Lanes 2 and 3 display ten well-resolved DNA fragments, which were selected for detailed quantitative analysis. (B) SEM image of 0.8 % of agarose gel (adapted with reference from [167])

To characterize the migration pattern more precisely, the Gel Analyzer tool integrated within ImageJ software was employed. This digital tool converts the gel image into a density profile plot, allowing extraction of key parameters such as band intensity (reflecting DNA fragment abundance) and migration distance (representing molecular size-dependent mobility). Through this analysis, the relative mobility of DNA fragments in lane 2 was determined to range between 20 and 118 mm. Similarly, lane 3 displayed a corresponding range of 22 to 117 mm, revealing a closely matched migration behavior between the two lanes. This systematic displacement pattern suggests uniform electrophoretic conditions across the gel, ensuring that the observed differences are inherent to the sample composition rather than experimental variations.

Interestingly, a minor deviation in the relative mobility of bands 1 through 7 between lanes 2 and 3 was observed. Such slight mobility differences may arise from subtle variations in DNA conformation, sample loading volume, or local gel inconsistencies. In molecular terms,

factors such as sequence composition (e.g., GC content), DNA topology (linear vs. supercoiled), and salt residue carryover can also affect migration. Nevertheless, the near-identical pattern between the two lanes indicates reproducible separation and validates the robustness of the electrophoresis process used in this experiment.

Beyond migration distance, the intensity of each DNA band provides valuable quantitative information about the relative abundance of individual fragments within each sample. Band intensity is directly proportional to the amount of DNA present in that zone, brighter bands correspond to larger quantities of DNA, while fainter bands represent less abundant fragments. By analyzing the integrated intensity (in square pixels) using ImageJ's Gel Analyzer, we obtained values ranging from 12,325.26 to 62,649.34 sq. pixels. These quantitative data can be used to infer relative DNA concentrations and assess sample loading uniformity across lanes.

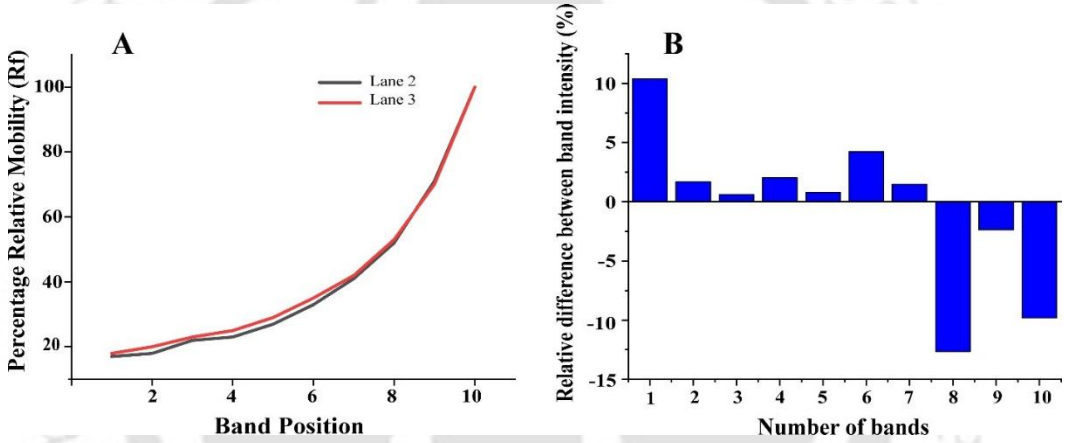

Figure 3.5: Comparative band mobility and intensity analysis. (A) Percentage relative mobility (Rf) plotted against band position for Lane 2 (black) and Lane 3 (red), showing closely overlapping migration profiles with a progressive increase in mobility at higher band positions. (B) Bar graph representing the relative percentage difference in band intensity between the two lanes across ten bands, highlighting minor variations at lower band numbers and pronounced negative deviations for bands 8–10.

Collectively, these findings not only elucidate the migration dynamics of DNA fragments under electrophoresis but also underscore the value of digital image analysis in enhancing the interpretative depth of classical gel-based techniques. The observed correspondence of migration patterns between lanes 2 and 3, accompanied by slight but measurable intensity variations, provides a detailed picture of DNA mobility and abundance. This understanding forms the basis for more advanced molecular biology applications, including size estimation of unknown fragments, restriction mapping, verification of PCR products, and genotyping workflows.

In summary, Fig. 3.5(A) provides a visual and quantitative assessment of DNA

migration behaviour under standardised electrophoretic conditions. The systematic analysis of mobility and intensity parameters enhances the reliability and reproducibility of electrophoretic measurements, enabling accurate characterisation of DNA fragment separation. These results validate the analytical approach and demonstrate the relationship between DNA molecular properties and migration behaviour, thereby supporting the robustness of the methodology for molecular analysis and experimental applications.

3.3.2 Quantitative Analysis of DNA Band Intensity and Relative Abundance

Band intensity is essentially a reflection of the amount of DNA present in a given fragment population; thus, analyzing intensity enables semi-quantitative estimation of sample concentration. In the current study, this intensity-based quantitative assessment was critical for comparing the DNA content between two experimental lanes. Fig. 3.2 (B) presents the relative difference in band intensity between lanes 2 and 3 across ten distinct DNA fragments. By calculating the relative difference (i.e., intensity in lane 2 minus intensity in lane 3), positive values correspond to higher intensity in lane 2, whereas negative values indicate higher intensity in lane 3. This approach provides a visual and numerical framework to assess the uniformity of DNA loading and the reproducibility of electrophoresis outcomes.

The results reveal that the intensity differences between these two lanes are generally small for most bands, signifying that both samples were loaded with nearly identical quantities of DNA. This similarity indicates consistency in the pipetting process, gel composition, and electrophoretic conditions. Minimal variation also implies that diffusion of DNA within the gel matrix was effectively controlled, reflecting well-optimized electrophoresis parameters such as buffer composition, voltage, and run time.

Slightly larger deviations in intensity occur in the higher band numbers (corresponding to smaller DNA fragments). Such differences can arise from several factors: (i) increased diffusion rates of smaller DNA molecules during electrophoresis, leading to fainter or slightly dispersed bands; (ii) imperfections in well loading or sample pipetting; and (iii) potential saturation effects in fluorescent detection for high-concentration regions. These parameters, although minor, highlight the delicate nature of electrophoretic separations, where physical effects like diffusion and molecular sieving subtly influence the measured fluorescence profile.

To further quantify this phenomenon, the Gel Analyzer function in ImageJ was used to obtain integrated intensity values for each band. The computed values spanned from 12,325.26 to 62,649.34 square pixels, corresponding to the lower and upper limits of fluorescence density among the ten fragments. These intensity values provide a direct measure

of relative DNA quantity within each fragment population. The resulting profile offers a semi-quantitative calibration that can be correlated with DNA standard markers to estimate fragment yield or purity.

Such analyses are valuable not only for interpreting experimental reproducibility but also for the principles of quantitative data interpretation in molecular biology. By measuring relative band intensities, the learning includes connecting visual electrophoretic patterns with quantitative representations of molecular abundance. This insight builds foundational understanding of how measurement, normalisation, and error analysis guide biotechnological applications ranging from genetic profiling to PCR-based diagnostics.

Moreover, the relationship between band intensity and DNA concentration has practical relevance in assessing sample quality across different experimental steps. High- or low-intensity bands can serve as indicators of yield efficiency in DNA extraction or as markers of successful PCR amplification.

In conclusion, the intensity analysis presented in Figures 3.5 (A) and (B) reinforces the reliability and reproducibility of the electrophoretic procedure, demonstrating near-identical quantitative DNA distributions between the two lanes. Subtle variations among specific bands offer insights into molecular diffusion dynamics and experimental precision. These findings collectively highlight the dual significance of electrophoretic analysis—both as a research technique for examining DNA composition and as a pedagogical tool that deepens understanding of molecular quantification and data-driven interpretation in the biological sciences.

3.3.3 Morphological Characterization of Agarose Gel Pore Structure

3.3.4.1 SEM Imaging of Agarose Gel Matrix

To directly visualize the internal microstructure of the agarose gel, SEM imaging was performed after appropriate sample preparation involving freezing and overnight drying. Fig. 2.1(A) shows a representative SEM micrograph of the agarose gel surface at high magnification. The image reveals an interconnected porous network formed by agarose fibers, with irregularly shaped pores distributed throughout the matrix.

3.3.4.2 Pore Size Distribution

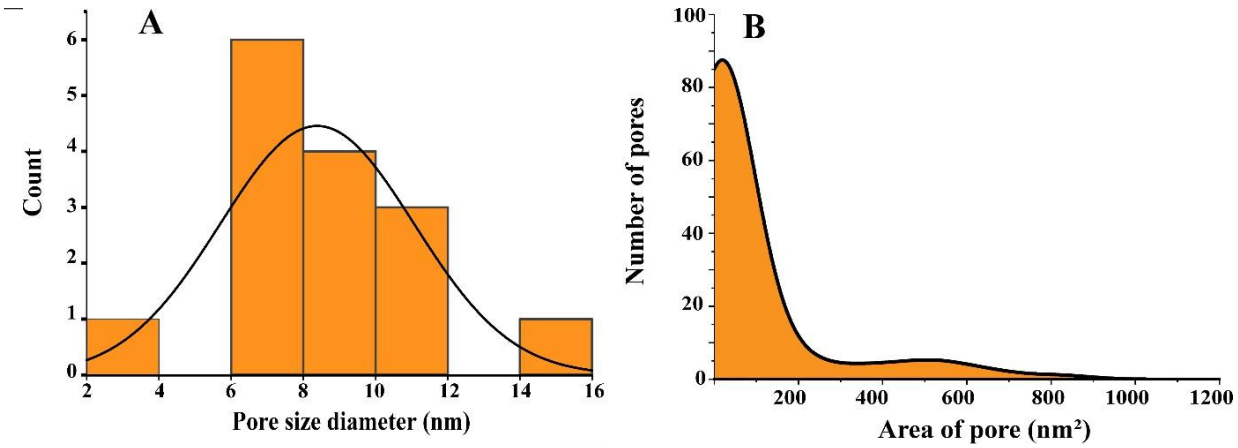

Figure 3.6: Histogram showing the distribution of pore size diameters (nm) with a fitted Gaussian curve, indicating the predominant pore size range of the sample. (B) Distribution of pore area (nm²) illustrating the frequency of pores as a function of their surface area, highlighting a higher population of smaller pores with a long tail toward larger pore areas.

Quantitative analysis of pore size was carried out by measuring pore diameters from SEM images using image analysis software. Fig. 3.6 represents a histogram of pore size diameter distribution, overlaid with a Gaussian fit. The pore diameters are primarily distributed in the range of approximately 5–12 nm, with a mean pore size centered around 8–9 nm. The relatively narrow distribution suggests a reasonably homogeneous gel matrix, which is consistent with the reproducible DNA migration observed in electrophoretic experiments.

3.3.4.3 Pore Area Distribution

In addition to pore diameter, pore area was analyzed to capture the variability in pore geometry. **Fig. 3.6 B** shows the distribution of pore area as a function of pore count. The distribution is highly skewed, with a large number of small-area pores (<200 nm²) and a progressively decreasing number of larger pores extending up to ~1200 nm². This long-tailed distribution indicates the presence of occasional larger voids within the gel matrix, which may locally facilitate faster migration of smaller DNA fragments.

3.3.5 Correlation Between Pore Structure and DNA Migration

The combined electrophoretic and SEM analyses provide a coherent picture of DNA transport through the agarose gel. The average pore sizes determined from SEM imaging are consistent with the size-dependent separation observed in gel electrophoresis, where larger DNA fragments experience greater hindrance and exhibit lower relative mobility. The presence of a heterogeneous pore area distribution explains the minor variations in band mobility and intensity between lanes. These results highlight the critical role of gel microstructure in determining electrophoretic performance. Accurate estimation of pore size distribution is therefore essential for optimizing gel concentration, predicting resolution, and interpreting

DNA migration behavior in analytical and preparative electrophoresis.

3.4 Conclusion

In this work, a combined electrophoretic and morphological approach was employed to elucidate the role of agarose gel microstructure in governing DNA band migration and intensity behavior. Quantitative image-based analysis of agarose gel electrophoresis demonstrated highly reproducible DNA band mobility and intensity across multiple lanes, indicating uniform electric field distribution and consistent gel architecture. Complementary SEM characterization revealed a nanometer-scale porous network with a moderately narrow pore size distribution, which directly correlates with the observed size-dependent separation of DNA fragments. The presence of a heterogeneous pore area distribution further explains minor variations in band mobility and intensity, particularly for smaller DNA fragments. Collectively, these results establish a direct structure–function relationship between agarose gel pore morphology and electrophoretic performance, providing a framework for understanding molecular sieving mechanisms in agarose-based separations. This study is also employed to interpret the relationship between band intensity and DNA concentration, thereby gaining hands-on experience in gel image analysis and understanding DNA quantification principles. Such training provides them insight into experimental reproducibility, data normalization, and semi-quantitative molecular analysis, skills foundational for genetic analysis, DNA fingerprinting, and diagnostic applications.

Overall, the intersection of electrophoresis, image analysis, and biosensing will likely be shaped by advances in quantitative bioimage analysis. As open-source tools and pipelines mature, they increasingly support robust extraction of intensity, size, and mobility metrics from gel images and hydrogel-based assays. Future work can couple these image-derived features with machine learning and uncertainty quantification frameworks developed for biosensors, enabling automated, statistically grounded interpretation of gel-based experiments that directly inform sensor design, optimization, and validation.

Chapter 4

Comparative Adsorption and Plasmonic Response of Functionalized AuNPs

Abstract

Gold nanoparticles (AuNPs) are widely employed in colorimetric biosensing due to their localized surface plasmon resonance (LSPR), which is highly sensitive to surface chemistry and interparticle spacing. However, the choice of surface linkers is often empirical, with limited understanding of how small structural differences influence adsorption behaviour and optical response. In this study, we present a comparative investigation of citrate-stabilized AuNP functionalization using two structurally related NHS-ester crosslinkers, 3,3′-dithiobis(sulfosuccinimidyl propionate) (DTSSP) and dithiobis(succinimidyl propionate) (DSP). Although both linkers possess disulfide moieties that enable Au–S chemisorption and terminal amine-reactive groups for bioconjugation, they differ in hydrophilicity and charge, which significantly influence their adsorption behaviour and optical response. DTSSP caused strong red shifts and aggregation, whereas DSP maintained stability with minimal spectral change; adsorption analysis showed higher, multilayer adsorption for DTSSP and more uniform adsorption for DSP. Overall, the results establish a direct correlation between linker chemistry, adsorption thermodynamics, surface mobility, and plasmonic response. The anionic and hydrophilic nature of DTSSP promotes dynamic surface reorganization and aggregation-driven red shifts, while DSP forms a more compact and stable interfacial layer that preserves colloidal dispersion. The insights obtained in this work provide fundamental design principles for controlling nanoparticle stability, aggregation, and plasmonic response through linker chemistry. Such understanding can accelerate the development of nanoparticle-based biosensors by reducing trial-and-error in surface functionalization. These findings are also relevant to nanomedicine, where stable nanoparticle coatings are essential for drug delivery, imaging, and therapeutic applications. In addition, improved control over nanoparticle interfaces can support the development of sensitive environmental sensors for detecting pollutants and toxins. More broadly, the study advances the fundamental understanding of nano–bio interfaces, enabling rational design of functional nanomaterials

for diverse technological applications.

Keywords: Gold nanoparticles (AuNPs); DTSSP; DSP; Surface plasmon resonance (SPR); Adsorption isotherm modeling; Colorimetric biosensing.

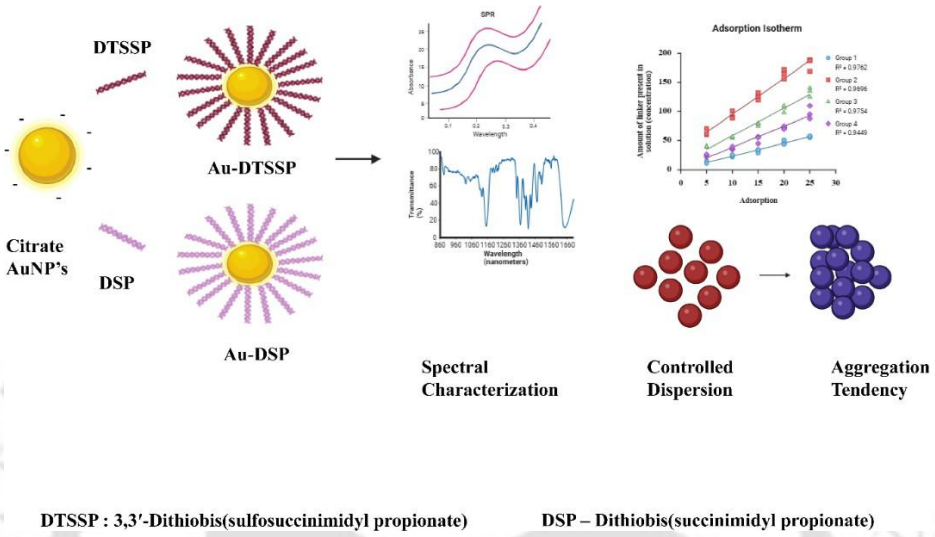

Figure 4.1: Schematic of DTSSP and DSP functionalization of citrate AuNPs and their basic characterization along with SPR change

4.1 Introduction

Gold nanoparticles (AuNPs) have emerged as one of the most versatile and promising nanomaterials in biomedical research, primarily due to their unique physicochemical properties that enable diverse therapeutic and diagnostic applications.[168] Their exceptional characteristics including tunable optical properties, high surface-area-to-volume ratios, biocompatibility, and facile surface functionalization—position them at the forefront of modern nanomedicine.[169]

The distinctive properties of gold nanoparticles arise from their nanoscale dimensions, typically ranging from 1 to 150 nm. At this scale, AuNPs exhibit quantum size effects and unique electronic configurations that differ markedly from bulk gold.[170] The high surface-area-to-volume ratio facilitates enhanced reactivity and molecular interactions, making them exceptionally suitable for conjugation with various biomolecules. This property is particularly advantageous for drug delivery and biosensing applications, where maximizing surface interactions is critical for therapeutic efficacy.[168]

AuNPs demonstrate remarkable chemical stability under varying pH, temperature, and ionic conditions, ensuring consistent performance and long-term reliability across diverse biological environments.[171] Their inert nature minimizes non-specific interactions with

biological systems, while their gold-thiol chemistry provides a robust platform for selective surface functionalization. The ease of synthesis through both chemical and physical methods, combined with precise control over size and shape, further enhances their versatility.[172]

The most distinctive feature of gold nanoparticles is their localized surface plasmon resonance (LSPR), a phenomenon that underpins many of their biomedical applications. LSPR occurs when incident electromagnetic radiation, typically in the visible to near-infrared spectrum interacts with the conduction band electrons in the metallic nanoparticle. This interaction causes the free electrons to oscillate collectively at a specific resonance frequency, creating an intense, localized electromagnetic field confined to the nanoparticle surface.[22] The resonance frequency is exquisitely sensitive to the nanoparticle's size, shape, and the dielectric properties of the surrounding medium. For spherical gold nanoparticles, the LSPR peak typically occurs between 500-600 nm, appearing as a characteristic ruby-red color in solution. However, anisotropic structures such as nanorods, nanostars, and nanotriangles exhibit multiple plasmon bands, including longitudinal modes that can be tuned into the near-infrared region (650-1000 nm), where tissue penetration is optimal.[173]

AuNPs are highly effective for surface functionalization, providing a valuable platform for the development of colorimetric biosensors. Their properties, like absorption, scattering, and fluorescence is critical for such applications. As the size of these spherical nanoparticles increases from 20 nm to 80 nm, the absorption spectra demonstrate a significant shift from 520 nm to 550 nm. The red-shift, as related to the size of the nanoparticles, progressively increases with larger gold nanoparticles. Additionally, the formation of complexes with ligand or macromolecule alters the local dielectric environment. This interaction exposes the nanoparticles to solvents that affect the refractive index at the interface, thereby enhancing their functionality. The plasmon resonance creates an electromagnetic field enhancement that can be 10^3-10^6 times stronger than the incident field in localized "hot spots".[174] This field is confined to within a few nanometers of the nanoparticle surface—the so-called near-field region—effectively concentrating light energy into volumes far smaller than the diffraction limit. This property forms the basis for surface-enhanced spectroscopic techniques and highly sensitive biosensing platforms.

The ability to functionalize AuNP surfaces with diverse molecular entities is central to their biomedical utility. Gold's strong affinity for sulfur-containing compounds, particularly thiols, provides a straightforward conjugation strategy. Molecules bearing thiol (-SH),

disulfide (-S-S-), or thioether groups spontaneously form stable Au-S bonds with nanoparticle surfaces, creating robust, covalent attachments that withstand physiological conditions.[175]

To enhance the sensitivity and specificity of the colorimetric sensors, attaching linker molecules onto the surface of the gold nanoparticles is the appropriate strategy. Conventionally, bio-conjugate methods, like passive adsorption and random covalent bonding for bifunctional linkers attachment were widely used. Efficient choice of linkers for surface modification includes polyethylene glycol (PEG), biotin-avidin, N-hydroxysuccinimide (NHS) esters, 1-ethyl-3-(3-dimethylaminopropyl)carbodiimide (EDC), and 11-mercaptoundecanoic acid (MUA). 23,24 Among these linkers, thiol functional groups are critical for attachment to gold surfaces. DTSSP -3,3'-Dithiobis(sulfosuccinimidyl propionate) and DSP -Dithiobis(succinimidyl propionate) are two such widely-used linkers that leverage this property by covalently binding to the AuNPs. 25,26 Importantly, both of these probes contain a central disulfide bond, readily cleaved in situ for thiol-based binding with the Au core, while their N-hydroxysuccinimide (NHS) ester termini covalently couple to primary amines on biomolecules.[176]

The key chemical difference between the two linkers is the presence of an additional sulfonate group in DTSSP. The functional moiety aids in dispersibility in the aqueous environments compared to the DSP. This quality enables the DTSSP linker to maintain the native conditions of biomolecules, making it ideal for applications in drug delivery, protein-protein crosslinking and interaction studies where minimal interference is crucial. Due to their ability to covalently bind with the gold nanoparticles both these linkers are used in biosensing.

4.1.1 Functional and mechanistic insights of DTSSP and DSP probes

DTSSP and DSP are chemical cross-linkers that are used in biosensors, drug delivery, and protein studies. Their utility lies in attachment to gold particles through cleavable thiol groups. Additionally, they also form stable amide bonds through sulfo-NHS esters by linking amine-containing molecules. The main difference between them is that DTSSP is water-soluble because it has sulfonate groups, while DSP is not water-soluble due to lack of charged groups, and thus dissolves in organic solvents like DMSO and DMF. This makes DTSSP more useful for experiments in water or outside cells, whereas DSP is better for experiments inside cells, for detecting neurotransmitters,[177] or for working with membrane proteins.[186] In this section, we summarized the strategies adopted for linking DTSSP and DSP linkers for

biosensing application.

DTSSP has also proven particularly useful for linking proteins and lipids due to its water solubility and compatibility with physiological pH. Chung et al. immobilized Myoglobin on a gold surface through a chemical bond formed between the amine groups of myoglobin and the sulfo-NHS ester groups of DTSSP.[178] Importantly, the DTSSP fragment retains its redox property even after immobilization, which is confirmed through the oxidation and reduction peak characterization. Oliverio et al. have demonstrated the strategies of chemical functionalization of plasmonic surface biosensors, in which DTSSP is demonstrated to couple with Cys or Lys residues of self-assembled monolayers of Au surfaces.[179] Maity et al., reported the attachment of DTSSP linkers with the AuNPs to design POCT prototype to detect for β2-microglobulin (B2M) detection in human tears.[180] The mechanism involves, DTSSP's covalent attachment with AuNPs to form N-succinimidyl-3-thuipropionate via gold-sulphur bond. This bond has active NHS groups, which further can react with the primary amines present in the antibodies. Following this reaction step, one end of the antibody remains free to bind with the antigen, present in analyte. This attachment leads to a change in AuNPs size, causing agglomeration. The subsequent variation in AuNP color and intensity of transmitted rays thus forms the primary sensing principle. Ngo et al. further optimized a DTSSP based SERS assay, achieving superior sensitivity compared to conventional methods and successfully detected small extracellular vesicles (biomarkers) derived from ovarian cancer cell lines.[181] In their sandwich SERS immunoassay, the AuNPs were coated with Raman active molecules, followed by conjugation with target antibodies using DTSSP. The free surface-ends of these SERS nanotags were blocked with bovine serum albumin to prevent non-specific binding. The hydrodynamic radius of these nanotags were characterized to ~56 nm. The overall surface charge of these nanotags were negative, indicating its stability after conjugation with antibodies. Cordina et al. use DTSSP to attach lectins to AuNPs, enabling the formation of lectin-SERS nanotags for glycan (sugar) detection on proteins and cells. Here, the disulfide linkage chemisorbs on the AuNP surface and links the lectins to the AuNPs, while the N-hydroxysuccinimide (NHS) esters react with primary amines on the lectin.[182] The role of DTSSP is that lectin is stably displayed on AuNP surface, minimizing desorption during labelling and washing steps. Silva et al. have utilized DTSSP to attach antibodies to gold nanoparticles, enabling highly specific biosensing for the SARS-CoV-2 spike protein.[183] The characteristics Raman spectrum of free DTSSP were reported in this work, which shows marked difference with DTSSP conjugated AuNP due to SERS effects. The spectral results

indicate the disulfide bonds of DTSSP were broken when adsorbed on AuNPs. In another work done by D'Amato et al. DTSSP is used for the detection of a protein associated with Zika virus.[184] During antibody immobilization, DTSSP adsorbs onto the AuNP surface through its disulfide moiety, forming a stable linker layer on the nanoparticles. The sulfo-NHS ester groups of DTSSP remain available for bioconjugation and subsequently react with primary amine groups present on the antibody molecules. This nucleophilic substitution results in the formation of stable amide bonds, accompanied by the release of N-hydroxysulfosuccinimide, thereby covalently anchoring the antibody to the DTSSP-functionalized AuNP surface.

Ayankojo et al. used DTSSP to modify electrode surface, which allowed binding of ncovS1 proteins through its NHS groups. Here also, the S–S bond of DTSSP cleaves for further reaction and attachment with thin film, gold-modified electrode.[185] In another work by Chavan et al., a novel approach to detect serotonin through formation of its dimeric complex by catalytic oxidation, which binds with DTSSP coated AuNPs.[186] The final complex tends to aggregate which in turn changes color from wine red to blue for colorimetric assay. The aggregation tends to mediate through surface-functionalized DTSSP, where the succinimidyl ester binds with primary amine and allow the dimeric scaffold formation. Such linker-analyte-linker sensing system brings a unique strategy for immunoassay-based detection of serotonin.

DSP has also been widely used in sensors targeting macromolecules through the amine-reactive NHS ester groups, enabling specific and stable conjugation. Using this principle, Wang et al. developed a colorimetric sensor, in which DSP react with amino moiety of serotonin and another probe N-acetyl-l-cysteine (NALC) bind non-covalently through hydrogen bonding and electrostatic interaction to the hydroxyl moiety of serotonin. Henceforth, the Au-S bond is used to combine DSP and NALC, which leads to crosslinking aggregation and results in plasmon coupling. The double reaction mechanism effectively reduces the interference of other biomolecules in sensing mechanism. In another work by Liu et al, uses DSP-AuNPs prepared by ligand-exchange reaction, onto while dopamine was assembled via standard amine-coupling reaction between amino group of dopamine and carboxyl group of DSP. Fe^{3+} acts as a cross-linker in this case to induce aggregation of AuNPs via coordination to dopamine, which offers rapid colorimetric-based detection. Likewise, Ling et al., uses DSP-coated AuNPs probes to detect histamine. DSP reacts with aliphatic amino group of histamine, and imidazole ring of histamine selectively binds with AuNPs via π-π* conjugation. The reaction induces

aggregation of AuNPs, leading to colorimetric detection for red to blue color change. Jayeoye et al explored the DSP attachment with AuNPs, resulting in significant stability of nanoparticles compared to normal citrate-based stabilization approach. DSP-modified AuNPs tends to acquire capacity to resist facile aggregation irrespective of the system's ionic strength, while holding its amine conjugation capacity. In their work, they conjugated creatinine with DSP-AuNPs, which was further used for detection of Silver (Ag^{+}) ions in environmental samples. Furthermore, Au nanoprobes are often coated in thiolated polyethylene glycol in order to increase the circulation time and biocompatibility by semi masking probes from proteins found in biological tissues and serum.

While DTSSP and DSP are widely used for AuNP functionalization, there remains a clear gap in addressing comparative colloidal and optical property responsible for interfacial processes. In this work, we compared the linkers - DTSSP and DSP, functionalization with AuNPs, and correlated their concentration-dependent adsorption behavior. This study provides insights into optimizing linker selection for AuNP-based colorimetric biosensing platforms. Herein, we achieved reliable UV-based quantification of surface-bound DSP and DTSSP at concentrations as low as 5 µL from a 0.4 mg/mL stock solution, corresponding to approximately 1,397 µM for DSP and 726 µM for DTSSP (equivalent to 2 µg of linker). The minimum detectable amount for our assay was determined to be 3.32 µL for DSP and 0.87 µL for DTSSP, corresponding to the smallest volumes of linker that could be reliably detected through surface attachment to AuNPs. This study corroborates experimental method and theoretical modelling for monitoring binding kinetics that might prove useful for designing novel probes. The study of the kinetic parameters of gold-thiolate bond on colloidal gold nanoparticles was performed, with the intention of designing parameters necessary to successfully prepare optical nanoprobes for biological sensing applications.

4.2 Materials and methods

Gold(III) chloride trihydrate ($HAuCl_4 \cdot 3H_2O$), sodium citrate tribasic dihydrate, 3,3′-dithiobis(sulfosuccinimidyl propionate) (DTSSP), and dithiobis(succinimidyl propionate) (DSP) were purchased from Sigma-Aldrich. All chemicals were of analytical grade and used as received without further purification.

4.2.1 Synthesis of Gold Nanoparticles (AuNPs)

AuNPs were synthesised via the modified Turkevich reduction method under highly controlled physiological conditions.[187] The citrate to gold chloride precursor was set to

1.5:1(trisodium citrate dihydrate: $HAuCl_4$). Initially, 195 ml of water was boiled in a round-bottom Erlenmeyer flask on a hot plate. A cylindrical magnetic stir bar was placed inside to stir the solution vigorously, ensuring uniform temperature. Separately, 20 mg of $HAuCl_4$ was suspended in 0.7 mL of Milli-Q water, and this was gradually added to the boiling water. In parallel, 30 mg of trisodium citrate dihydrate was dissolved in 3 ml of Milli-Q water. This reaction mixture was maintained at a boil with continuous stirring until the colour of the solution slowly changed from pale yellow to wine red. Aliquots of the solution were collected every 10 minutes for a total of 80 minutes to monitor the growth of nanoparticles.

4.2.2 Optimization of DTSSP and DSP conjugation on AuNPs

The DTSSP stock solution was prepared at an approximate concentration of 657 µM, while the DSP stock solution was maintained at ~989 µM. For concentration-dependent functionalization studies, DTSSP was added to AuNP dispersions at 3, 6, 14, 20, 26, 33, 40, 46, 55, 60, and 66 µM. Similarly, DSP concentrations were varied at 5, 10, 20, 30, 40, 50, 60, 70, 80, 90, and 100 µM. Defined aliquots from the respective stock solutions were introduced into the nanoparticle suspensions and vortexed to ensure homogeneous mixing, followed by overnight incubation at 4 °C to facilitate surface functionalization. The samples were then centrifuged at 11 000 rpm to remove unbound linker molecules, and the resulting AuNP–linker conjugates were resuspended in deionized water for subsequent analysis.

4.2.3 Physicochemical Characterization of AuNP–Linker Conjugates

The UV–visible absorbance spectra of AuNP–DTSSP and AuNP–DSP dispersions were recorded using a Shimadzu UV–vis spectrophotometer. All measurements were performed in triplicate using quartz cuvettes with a 1 cm optical path length at 25 °C. Deionized water was used as the reference blank. The absorbance spectra were collected over a wavelength range of 250–700 nm. For absorption measurements, 1 mL of AuNP–DTSSP and AuNP–DSP dispersions was directly withdrawn from the respective stock solutions and used for UV–vis spectral readings. To investigate the rate kinetics of linker binding and subsequent stabilization of AuNPs, the linker solution was added directly to the AuNP dispersion in situ, and UV–vis spectra were recorded immediately after addition and at regular time intervals thereafter.

The functionality and interaction of the synthesized nanoparticles (AuNPs) along with the functionalized nanocomposites (AuNP-DTSSP) and (AuNP-DSP) were inspected using a

PerkinElmer FTIR spectrophotometer (Spectrum Two) at 25 °C in the range of 4000–400 cm^{-1}. The spectral resolution was adjusted to a resolution of 4 cm^{-1} with 36 scans.

4.2.3.1 FE-TEM

For FE-TEM sample preparation, a small aliquot of the AuNP–DTSSP and AuNP–DSP dispersions was drop-cast onto a carbon-coated copper grid (400-mesh) and allowed to dry under ambient conditions before imaging.

4.2.3.2 Energy-Dispersive

Elemental composition and purity of the synthesized AuNPs and linker-functionalized conjugates were analyzed using energy-dispersive X-ray spectroscopy (EDX) coupled with a field-emission transmission electron microscope. For sample preparation, a dilute dispersion of AuNP, AuNP–DTSSP, or AuNP–DSP was drop-cast onto a carbon-coated copper grid and allowed to dry under ambient conditions. The dried grids were introduced into the microscope chamber under high vacuum, and spectra were acquired from multiple regions to ensure representative elemental analysis. The characteristic Au signal was used to confirm nanoparticle composition, while additional peaks corresponding to C, O, N, or S indicated successful surface functionalization.

4.2.3.3 X-ray Diffraction (XRD)

The crystalline phase and structural properties of AuNPs were investigated using powder X-ray diffraction (XRD). For sample preparation, colloidal dispersions were centrifuged to obtain concentrated nanoparticle pellets, which were subsequently drop-cast onto a clean glass substrate and dried to form a thin film. Diffraction patterns were recorded over a 2θ range of 20°–80° using Cu Kα radiation. The obtained diffraction peaks were indexed to evaluate crystallinity, lattice structure, and phase purity of the synthesized nanoparticles.

4.2.3.4 Selected Area Electron Diffraction (SAED)

Selected area electron diffraction (SAED) analysis was performed during TEM imaging to examine the crystallographic structure of individual nanoparticles. A small volume of diluted AuNP dispersion was deposited onto a carbon-coated copper grid and air-dried prior to measurement. Diffraction patterns were collected from localized regions using an appropriately selected-area aperture to isolate individual nanoparticle assemblies. The resulting concentric diffraction rings were analyzed to identify characteristic

crystallographic planes and confirm the polycrystalline face-centered cubic structure of gold.

4.2.4 Adsorption analysis

To monitor linker adsorption over a wide range of concentrations, nanoparticles were conjugated with linkers DSP and DTSSP, and a standard curve was used to determine the number of linker molecules adsorbed per particle at saturation and apparent dissociation constants for each linker-AuNP conjugate.

The adsorption isotherm helps elucidate how the adsorbate interacts with the surface of the adsorbent at equilibrium concentration (Ce). In our study, we studied the following adsorption isotherm fittings - Langmuir, Freundlich, Temkin Isotherms. Initially, the adsorption capacity was calculated using equation 1

$$Qe = \frac{(C_0 - C_e)V}{m} \qquad \text{Equation 1}$$

Where, Co is initial concentration of adsorbate (mg/mL), Ce is equilibrium concentration of adsorbate (mg/mL), V is volume of solution (L), and m is the mass of adsorbent (mg). The Langmuir isotherm linearized as $1/Q_e$ vs $1/C_e$, which represents monolayer adsorption onto a homogeneous adsorbent surface, as per equation 2

$$\frac{1}{Q_e} = \left[\frac{1}{Q_{max}K_L}\right] * \left(\frac{1}{C_e}\right) + \left(\frac{1}{Q_{max}}\right) \qquad \text{Equation 2}$$

Where Q_e is amount of adsorbed NPs in $mg.g^{-1}$, Q_m is maximum adsorption capacity from for monolayer coverage in $mg.g^{-1}$, and C_e is initial concentration of NPs in solution.

Freundlich isotherm linearized as $\log Q_e$ vs $\log C_e$, which is appropriate for multilayer adsorption on heterogeneous surfaces as per equation 3

$$logQ_e = logKF + \frac{1}{n} logC_e \qquad \text{Equation 3}$$

Temkin Isotherm linearized as Q_e vs $\ln C_e$, accounting for adsorbate-adsorbent interactions and a variable heat of adsorption, using equation 4

$$Q_e = BlnCe + BlnA \qquad \text{Equation 4}$$

Parameters for Qmax, K_L, K_F, n, A, B were obtained by a linear curve fitting method, where Qmax represents the maximum adsorption capacity, K_L represents the Langmuir constant, and K_F represents the Freundlich constant.

Goodness-of-fit was evaluated via regression coefficient (R^2) and residual analysis. All data points and fitted curves were plotted for complete comparative visualization.

4.3 Results and Discussion

4.3.1. Characterization of Bare AuNPs

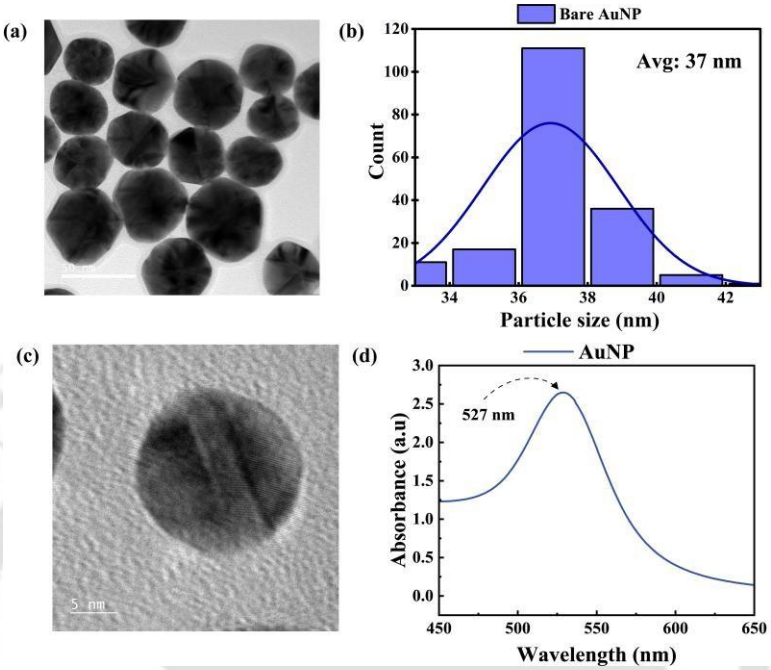

Figure 4.2: Morphological and size distribution analysis of bare AuNPs. (a) TEM image showing spherical gold nanoparticles (scale bar: 50 nm). (b) Particle size distribution histogram (c) High-resolution TEM image of AuNP (5 nm scale bar) (d) UV–Vis absorption spectrum of AuNPs exhibiting a distinct surface plasmon resonance (SPR) band centred at ~527 nm, characteristic of well-dispersed gold nanoparticles

The transmission electron microscopy (TEM) image in Fig. 4.2 (a) reveals that the synthesized bare AuNPs possess a predominantly spherical morphology with relatively uniform size distribution and well-defined particle boundaries, indicating controlled nucleation and growth during synthesis. The particles appear well-dispersed with minimal aggregation, suggesting good colloidal stability. Statistical analysis of particle dimensions, shown in Fig. 4.2 (b), presents a narrow size distribution fitted with a Gaussian profile, yielding an average particle diameter of approximately 37 nm. The limited spread in particle size confirms the monodisperse nature of the nanoparticles, which is critical for achieving consistent optical and plasmonic properties. Such uniform morphology and size homogeneity are expected to contribute to stable surface plasmon resonance behavior and reliable performance in subsequent functionalization and sensing applications.

Selected area electron diffraction (SAED) is a transmission electron microscopy (TEM)-based technique used to investigate the crystalline structure, phase composition, and

lattice ordering of nanomaterials. By collecting diffraction patterns from a localized region of the sample, SAED provides information about crystallinity and atomic arrangement, allowing differentiation between amorphous, single-crystalline, and polycrystalline structures. The SAED pattern shown in Fig. 4.3 (c) has a well-defined concentric ring corresponding to the characteristic (111), (200), (220), and (311) crystallographic planes of fcc gold were observed through the SAED analysis with measured d-spacing values of 2.35, 2.04, 1.44, and 1.23 Å, respectively (Fig. 4.2), indicating the formation of highly crystalline face-centered cubic (fcc) AuNPs with a polycrystalline nature and well-ordered lattice structure. The presence of sharp and continuous diffraction rings further confirms uniform crystallinity and phase purity of the synthesized nanoparticles, consistent with the XRD and HRTEM observations.[191] The UV–Vis spectrum exhibits a distinct SPR band at approximately 527 nm, confirming the formation of gold nanoparticles.[192] The well-defined peak indicates uniform particle distribution and stable optical behavior, which is essential for subsequent functionalization and sensing studies. HRTEM analysis was used to evaluate the morphology of gold nanoparticles. The high-resolution TEM (HRTEM) image of AuNPs showing a well-defined nanoscale particle with clear lattice fringes, indicating crystalline structure and uniform morphology at the nanometer scale (scale bar: 5 nm). The image reveals clear lattice fringes with an interplanar spacing of approximately 0.234 nm, which corresponds to the (111) crystallographic plane of fcc gold.

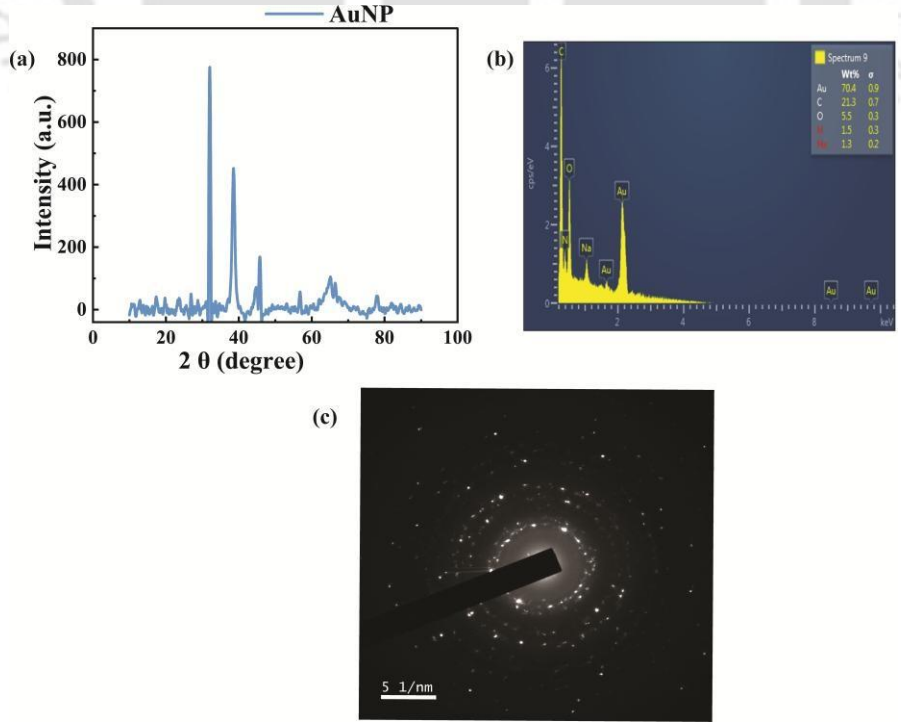

Figure 4.3: (a) X-ray diffraction (XRD) pattern of AuNPs displaying characteristic diffraction peaks

corresponding to the crystalline structure of gold, confirming successful nanoparticle formation and phase purity (b) Energy-dispersive X-ray spectroscopy (EDS) spectrum of AuNPs confirming the elemental composition (c) Selected area electron diffraction (SAED) pattern of AuNPs

The EDX elemental mapping exhibited a characteristic peak at approximately 2.30 keV, corresponding to the Au X-ray emission line, with additional smaller peaks at 8.5, 9.8, 10.4, and 11.5 keV corresponding to higher-order X-ray transitions (**Fig. 4.3**). This further confirmed the uniform distribution of gold throughout the sample. When DTSSP was used to conjugate with AuNPs, it approaches the Au surface, and Au electrons cause the reductive cleavage of the disulfide bond. In the solvent medium, the intact disulfide bond of the DTSSP molecule undergoes hydrolysis, which lets the formation of a covalent bond with Au atoms through the sulfide group.[184] Hydrolysis of the DTSSP-AuNP complex results in surface-bound carboxylates, which give AuNP an overall negative charge.[193] Notably, DTSSP contains two NHS ester groups, which are open for reaction with the terminal Lys residues, which form the basis of AuNP functionalization with biomacromolecules.[194]

4.3.2 Reaction Mechanism

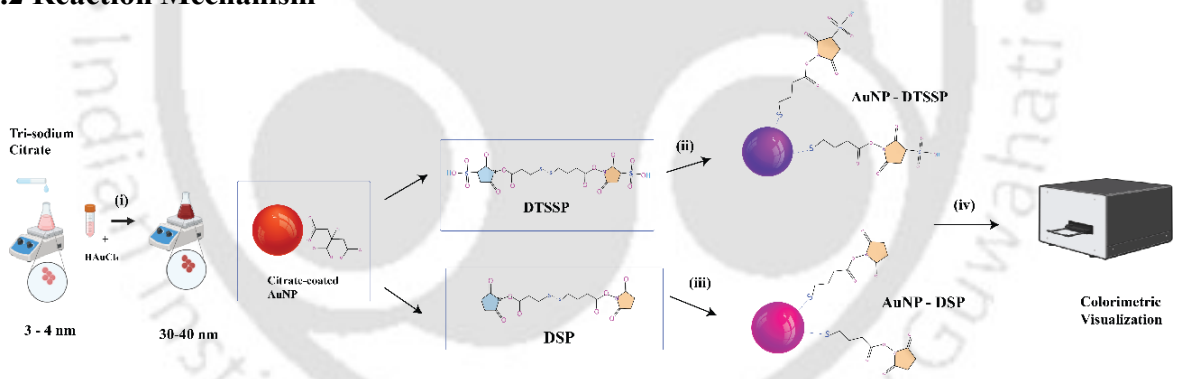

Figure 4.4: Schematic representation of AuNP synthesis followed by surface functionalization with DTSSP and DSP linkers

Fig. 4.4 shows the steps pertaining to the reaction mechanism for the functionalization with the linkers DTSSP and DSP. Firstly, we synthesised AuNPs using modified Turevich Method, followed by covalent attachment of DTSSP and DSP linkers. In the subsequent step a covalent attachment of DTSSP with AuNPs to form N-succinimidyl-3-thiopropionate (NTSP) via gold-sulphur bonds was established. The NSTPs formed in the AuNP-DTSSP reaction composites have an exposed active N-hydroxysuccinimide (NHS) groups, which is active for biomolecules attachment through primary amine groups.[195]

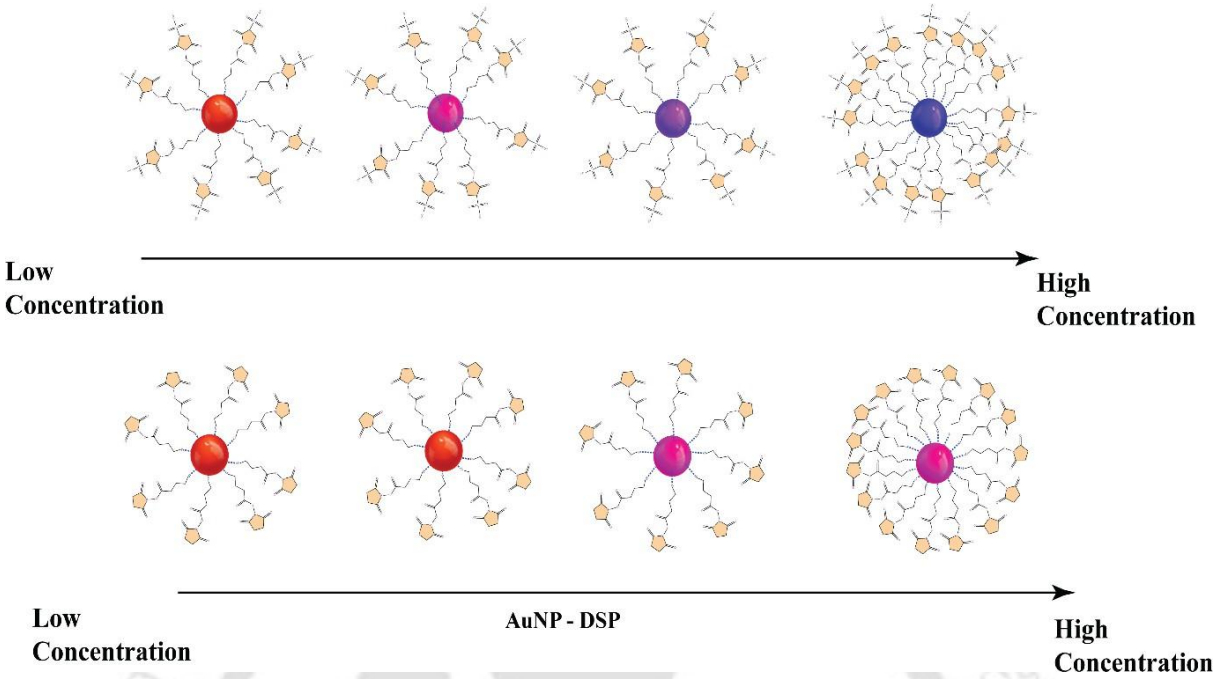

Figure 4.5: Concentration-dependent colorimetric response of AuNP–DTSSP and AuNP–DSP systems, showing progressive linker binding and nanoparticle assembly from low to high concentrations.

The attachment of DTSSP and DSP onto the citrate-capped AuNPs leads to a change in Surface Plasmon Resonance of AuNPs, which accounts for the agglomeration phenomenon. This agglomeration was accompanied by a visible change in the color of the AuNP suspensions, along with variations in the intensity of transmitted light through the colloidal solutions, indicative of altered optical properties upon linker conjugation.[180] This results in a bathochromic shift of the surface plasmon resonance band and a change in the color of the solution from red to blue as shown in Fig. 4.5, which is useful deterministically even at a very low analyte concentration.

4.3.3 Spectral Behavior of AuNP-DTSSP and AuNP-DSP

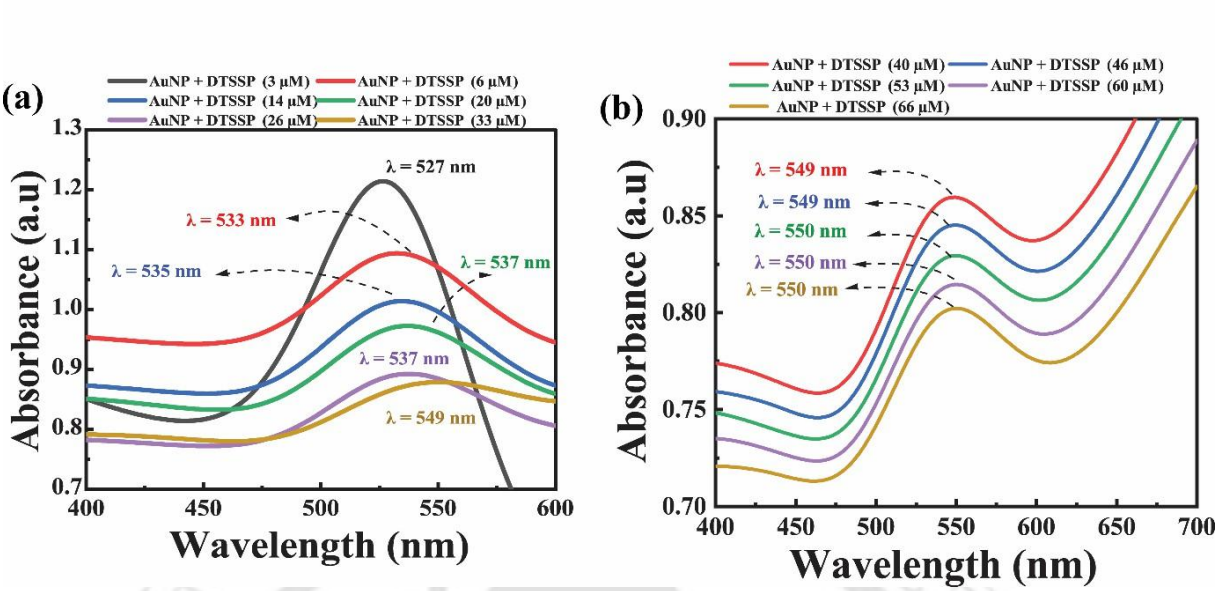

Figure 4.6: UV–Vis absorption spectra of the AuNP–DSP system showing concentration-dependent optical behaviour. (A) Spectral response at low DSP concentrations (5–40 µM) illustrating gradual changes in absorbance intensity. (B) Spectra recorded at higher DSP concentrations (50–100 µM) show further modulation of the plasmonic band

In order to prove the projected mechanism discussed in Fig. 4.5, a series of materials and optical characterizations have been performed. The UV-vis spectra of AuNPs, DTSSP-AuNP conjugates, and DSP-AuNP conjugates have been summarized as shown in Fig 4.6 (a-b) and Fig. 4.9 (a-b), respectively. Bare AuNP samples show a characteristic peak maximum at 527 nm confirming the size to be in the range of 35 – 40 nm. The attachment of the linkers DSP and DTSSP has been confirmed by the red-shift of the AuNP peak to 529 nm and 533 nm, respectively. This can be attributed to a change in the local refractive index around the attached AuNPs after the attachment of linkers and subsequent agglomeration of AuNPs due to the presence of active sites on the linker. In particular, the presence of thiol-derived disulfide moieties and NHS ester groups in DTSSP and DSP facilitates surface binding and interparticle bridging, promoting aggregation of the AuNPs.

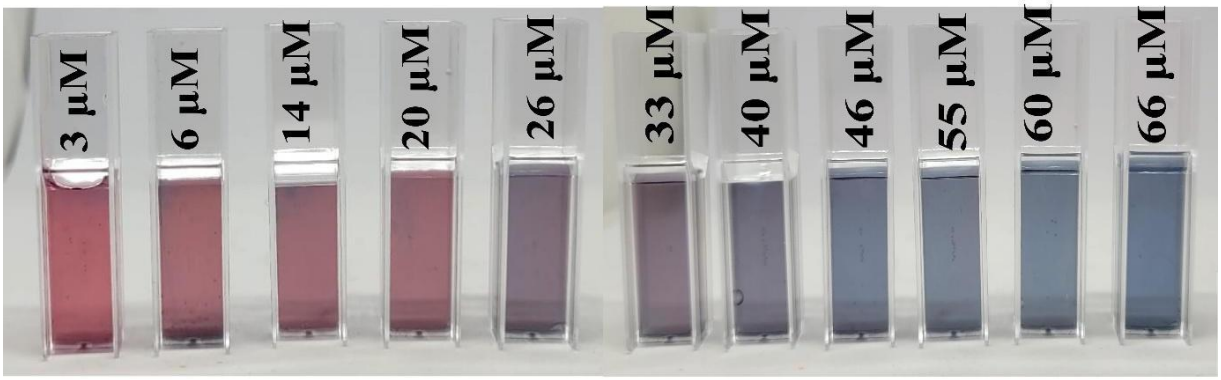

Figure 4.7: Colorimetric sensing response of AuNP–DSP system showing a progressive change in solution colour with gradual increase in DTSSP concentration (5–100 µM)

The addition of the DTSSP linker (6 µM) to AuNPs resulted in a red-shift of the SPR peak from 527 nm to 533nm. As the DTSSP concentration increases, the SPR peak progressively shifts to 535 nm (14 µM), 537 nm (20 µM and 26 µM), 549 nm (33 µM, 40 µM, and 46 µM), and finally reaches 550 nm at 53 µM and 66 µM DTSSP, indicating an intense increase in local refractive index and plasmonic coupling arising from enhanced surface functionalization and concentration-dependent interparticle aggregation, ultimately approaching saturation of linker adsorption on the AuNP surface, which can be seen around 46 µM for DTSSP. The calibration plot for AuNP-DTSSP can be seen in Fig. 4.8.

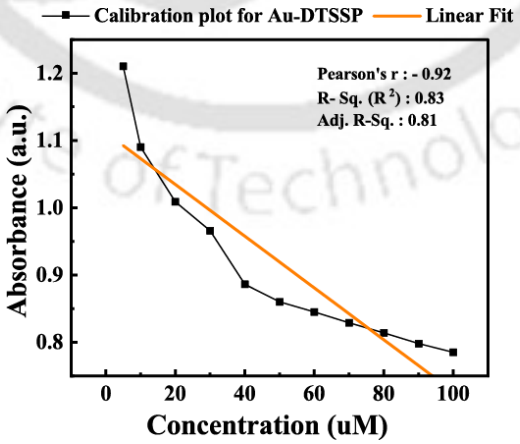

Figure 4.8: UV–Vis calibration curve of the AuNP–DSP system showing the linear relationship between absorbance and DSP concentration.

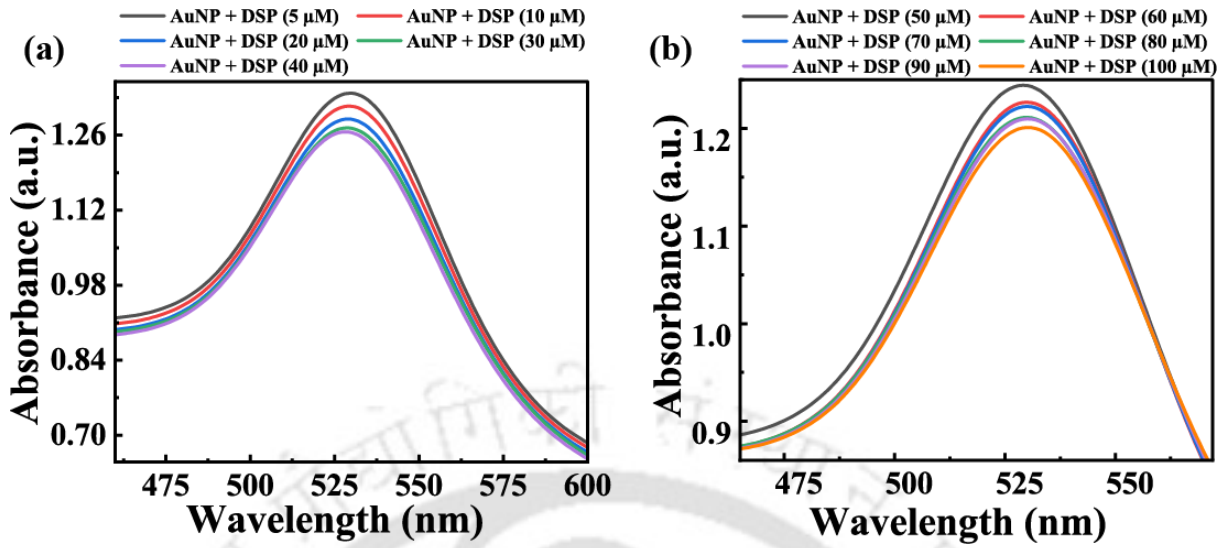

Figure 4.9: UV–Vis absorption spectra of the AuNP–DSP system showing concentration-dependent optical behavior. (A) Spectral response at low DSP concentrations (5–40 µM) illustrating gradual changes in absorbance intensity. (B) Spectra recorded at higher DSP concentrations (50–100 µM) showing further modulation of the plasmonic band

In contrast, DSP-AuNP conjugates showed relatively less red-shift with increasing concentration (Fig. 4.9). For a comparative analysis, the same linker concentrations were maintained. The addition of DSP to AuNPs (5 µM) resulted in an SPR peak at 527 nm. With increasing DSP concentration, only a slight redshift was observed, with the peak appearing at 528 nm (10–40 µM), 529 nm (50–60 µM), and 530 nm (70–100 µM), indicating minimal spectral change and limited surface modification compared to DTSSP, for increased concnetrations.

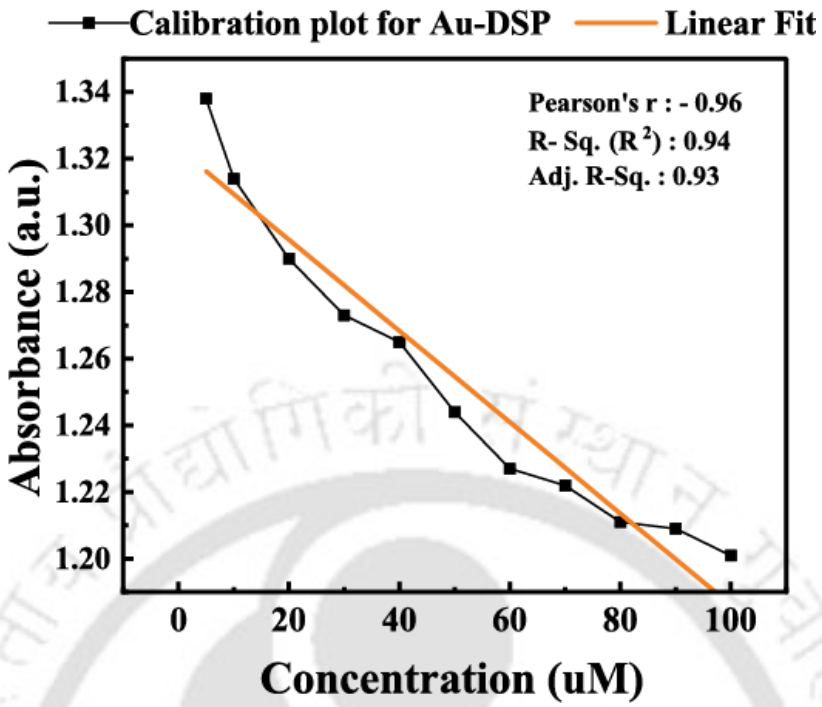

Figure 4.10: UV–Vis calibration curve of the AuNP–DSP system showing the linear relationship between absorbance and DSP concentration.

The linear fit confirms concentration-dependent optical response and demonstrates the suitability of the system for quantitative colorimetric sensing.

Figure 4.11: Colorimetric sensing response of AuNP–DSP system showing a progressive change in solution color with gradual increase in DSP concentration (5–100 µM)

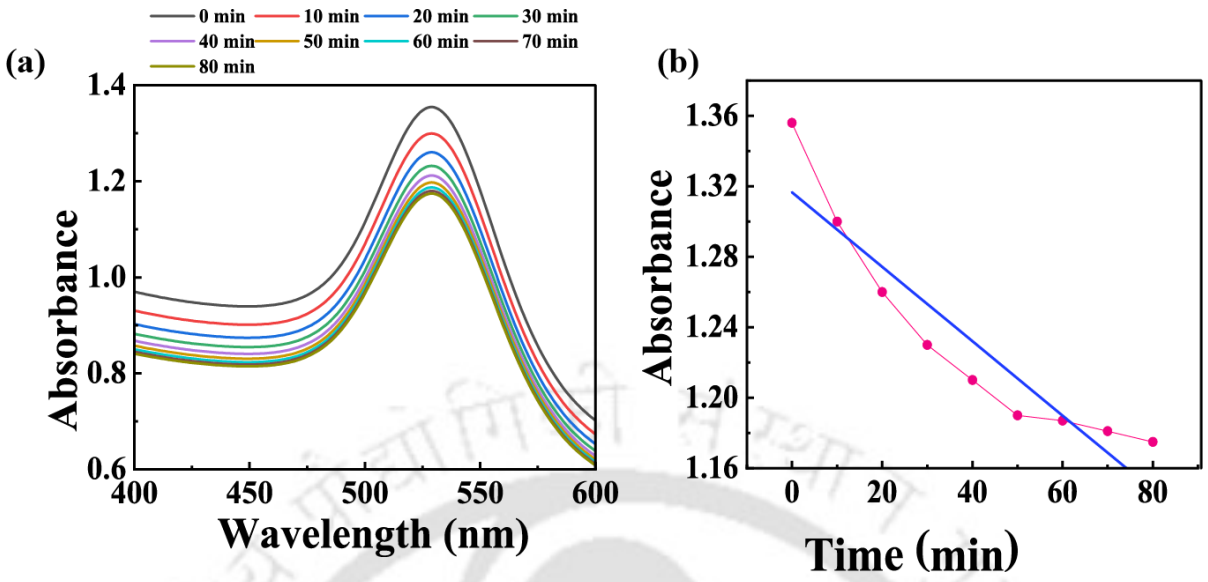

Figure 4.12: Time-dependent UV–Vis spectral evolution and kinetic analysis of linker–AuNP interactions AuNP and DSP

Time-resolved UV vis absorption spectra of AuNP-DTSSP conjugates have been recorded from 0 to 80 min, showing a gradual decrease in SPR peak intensity with time. Figures 4.12 and 4.13 present the evolution of the surface plasmon resonance (SPR) band of AuNPs upon conjugation with DTSSP and DSP, respectively, monitored over a period of 80 min. In both systems, the SPR band centered around ~527–535 nm progressively decreases in intensity with time, indicating changes in the local dielectric environment and nanoparticle surface state following linker adsorption.

For the DTSSP-functionalized AuNPs (Fig. 4.12 b), a pronounced and continuous decrease in SPR intensity is observed with increasing incubation time. This behavior suggests dynamic surface reorganization and progressive interparticle interactions facilitated by DTSSP. The presence of sulfonate groups in DTSSP enhances its aqueous solubility and electrostatic interactions, enabling increased surface mobility and linker-mediated bridging between adjacent nanoparticles. As a result, plasmonic coupling becomes more prominent with time, leading to attenuation of the SPR band.

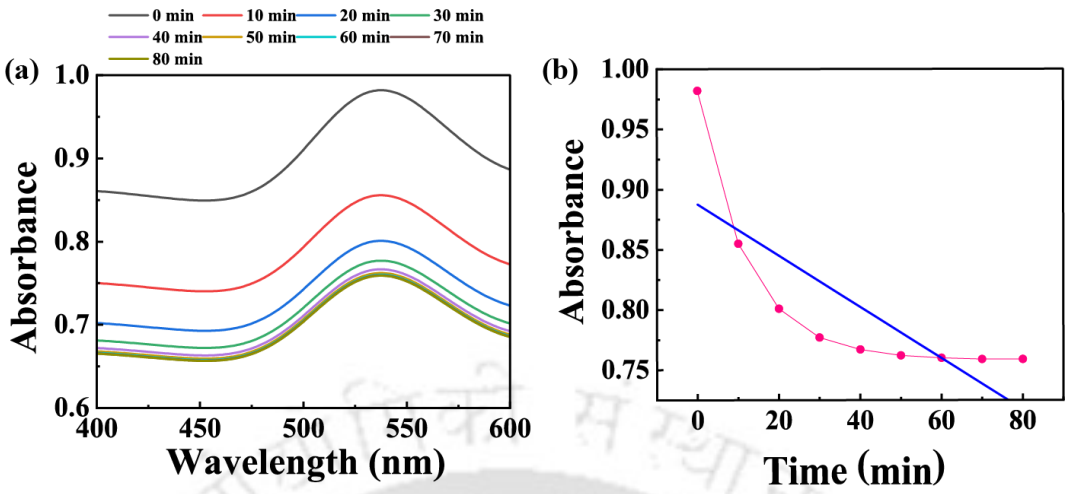

Figure 4.13: Time-dependent UV–Vis spectral evolution and kinetic analysis of linker–AuNP interactions AuNP and DTSSP

In contrast, the DSP-functionalized AuNPs exhibit comparatively smaller spectral changes over the same duration. The SPR intensity decreases at a slower rate, indicating a more stable colloidal system. DSP lacks charged sulfonate groups, which limits electrostatic repulsion and surface mobility, favoring the formation of a relatively compact and immobilized monolayer on the AuNP surface. This behavior is consistent with reduced interparticle bridging and minimal aggregation.

The kinetic trends are further quantified in Figures 4.12 (b) and 4.13(b), where the absorbance at the SPR maximum is plotted as a function of time. The AuNP–DTSSP system shows a steeper decline in absorbance, with linear fitting indicating faster kinetics of surface reorganisation and aggregation. The faster decline in absorbance observed for the AuNP–DTSSP system is attributed to the strong adsorption of DTSSP onto the gold surface, which partially displaces citrate stabilizers and reduces electrostatic repulsion between nanoparticles. The resulting interparticle interactions promote surface reorganization and aggregation, leading to a more rapid decrease in SPR intensity compared to bare AuNPs.

In contrast, the AuNP–DSP system exhibits a more gradual decrease in absorbance, indicating slower surface adsorption and reduced nanoparticle aggregation. The absence of sulfonate groups in DSP results in a less disruptive interaction with the citrate-stabilised AuNP surface, preserving colloidal stability for a longer duration. Consequently, interparticle interactions and surface reorganisation occur more slowly, leading to a lower rate of SPR intensity loss. The difference in absorbance decay rates between the AuNP–DTSSP and AuNP–DSP systems highlights the significant influence of linker chemistry on adsorption

kinetics and nanoparticle stability.

Overall, these results demonstrate that the AuNP-DTSSP system induces faster and more pronounced time-dependent changes in AuNP optical properties compared to the AuNP-DSP system. This behaviour can be attributed to the higher surface mobility, flexible spacer length, and charged nature of DTSSP, which collectively promote dynamic rearrangement and aggregation. Conversely, DSP forms a more stable, less mobile surface layer that preserves nanoparticle dispersion over time.

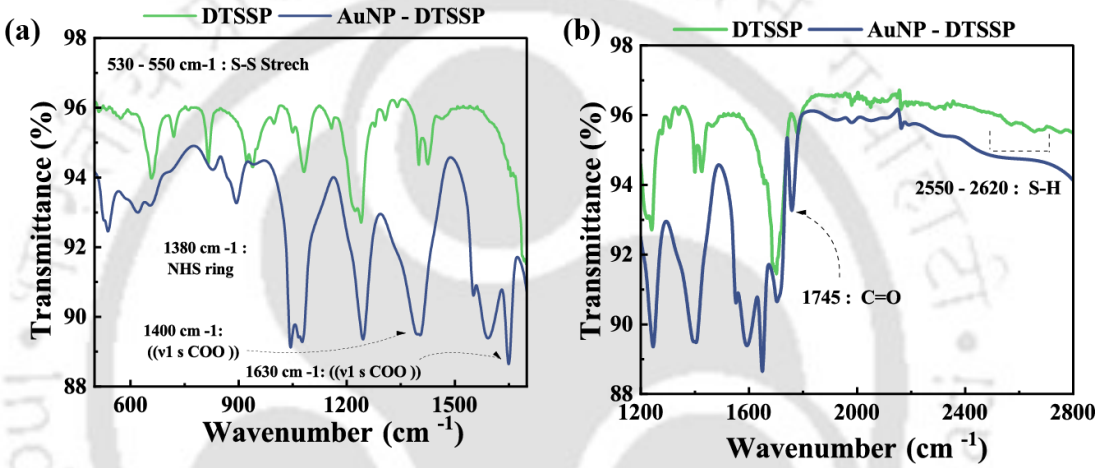

Figure 4.14: FTIR spectra of pure DTSSP and AuNP–DTSSP

The chemisorption of the [3,3′-Dithiobis(sulfosuccinimidyl propionate)] (DTSSP) and [dithiobis (succinimidyl propionate)] (DSP) crosslinker on the AuNP surface was validated using Fourier-transform infrared spectroscopy (FTIR). In Fig. 4.14 The adsorption of citrates on the AuNPs is confirmed by peaks at 1400 cm^{-1} for (vs (COO)) and 1630 cm^{-1} (va (COO-)).[183] Upon functionalization with DTSSP, the appearance of a peak around ~1740 cm^{-1} is associated with the carbonyl (C=O) stretching vibration of the crosslinker.The S-H stretch can be expected between 2550 and 2620 cm, indicating the stretch of the S-H bond binding to the surface of AuNP. This S-H stretch signal is very weak but can be seen at 2600, which shows the disappearance of the peak with the AuNP attachment.[196] The spectrum showed a decrease in the N-H characteristic peak at 3250 – 3300 cm-1 and the disappearance of the C=O peaks at 1720 – 1820 cm^{-1} for the sulfocuccinimidyl group, suggesting the formation of crosslinking bonds between DTSSP and the amino group.[197] HS ester bond peat at 1780 cm^{-1} and free carboxylic acid peak at 1740 cm^{-1}, ready for conjugation.[198]

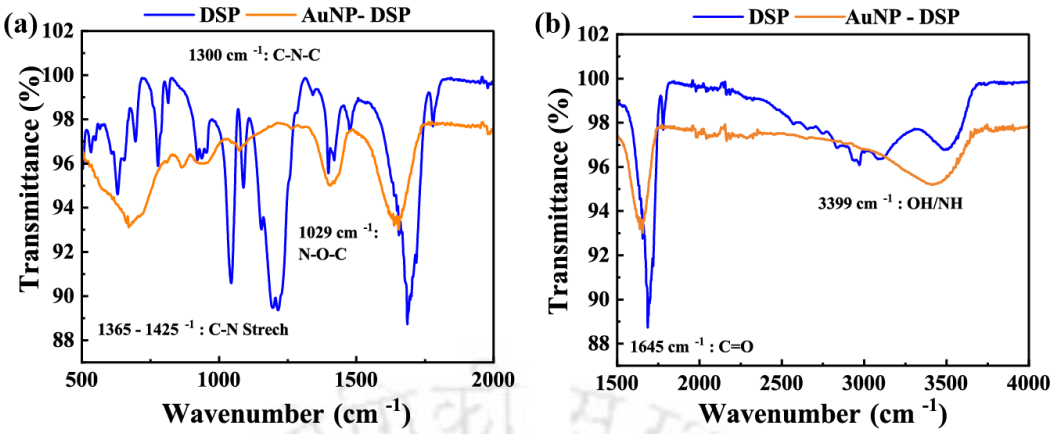

Figure 4.15: FTIR spectra of pure DSP and AuNP–DSP

The FT-IR analysis for surface interaction or chemisorption of the thiolate crosslinker (DSP) to the gold surface shows binding of the crosslinker represented (Fig. 4.15) by the peak at 1029 cm^{-1} which is a characteristic of N-O-V esters in DSO, 1297, 1316, 1345, 1408, 1436 cm^{-1} corresponding to C-N-C stretch of NHS esters and the peak at 1734 cm^{-1} represents the carbonyl stretching of the NHS esters.[199] The FTIR Spectra of DSP functionalized AuNPs shows the following peaks. The appearance of peak at 1718 cm^{-1} corresponds to the presence of C=O functional group. The appearance of a band at 2895 cm^{-1} corresponds to aliphatic C–H stretching, mainly from CH_2 groups.[200]

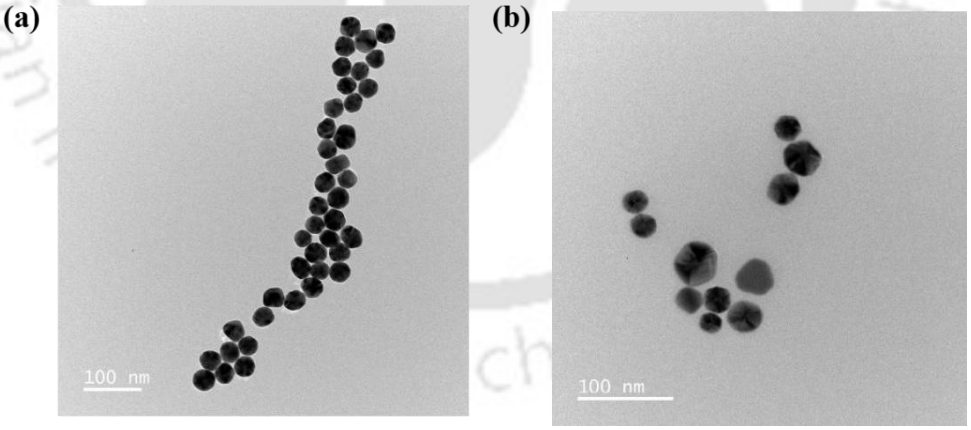

Figure 4.16: Transmission Electron Microscopy micrographs obtained for (a) AuNP conjugated DTSSP (b) AuNP conjugated DSP

The TEM images reveal distinct structural organization depending on the linker chemistry used for surface functionalization. In Fig.4.16 (a), AuNP–DTSSP conjugates form extended chain-like assemblies, suggesting enhanced interparticle interactions mediated by the hydrophilic and charged nature of DTSSP, which promotes dynamic surface rearrangement and aggregation. This structural arrangement is consistent with the pronounced plasmonic red-

shifts observed in UV–Vis analysis. In contrast, **Fig. 4.19 (b)** shows AuNP–DSP conjugates with more isolated and loosely distributed nanoparticles, indicating the formation of a relatively compact surface layer that preserves colloidal stability. The reduced aggregation in the DSP system reflects weaker interparticle bridging compared to DTSSP, supporting the observed minimal spectral shifts and stable optical response.

4.3.4 Thermodynamic Modeling of Linker Adsorption on AuNP Surfaces

Adsorption isotherm analysis provides a thermodynamic framework to understand how linker molecules interact with the gold nanoparticle surface at equilibrium. In AuNP–linker systems, adsorption determines the density, orientation, and uniformity of the surface-bound layer, which directly influences interparticle spacing, colloidal stability, and plasmonic behavior. Thiol-containing crosslinkers such as DTSSP and DSP undergo strong Au–S chemisorption, forming self-assembled interfacial layers whose surface coverage evolves with linker concentration. Modeling this process using adsorption isotherms enables evaluation of binding affinity, surface saturation, and energetic heterogeneity of the nanoparticle interface. In the context of plasmonic biosensing, such parameters are critical because variations in linker adsorption density alter the local refractive index and interparticle coupling, ultimately governing the magnitude of surface plasmon resonance (SPR) shifts and colorimetric response. Therefore, adsorption isotherm modeling serves as a bridge between molecular-level linker chemistry and the macroscopic optical properties observed in AuNP-based sensing systems.

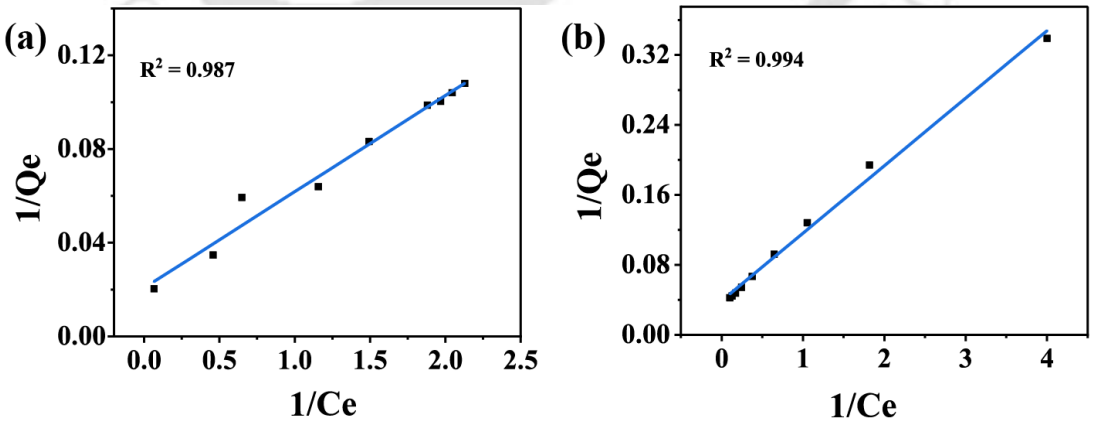

Figure 4.17: Linearized adsorption isotherm plots derived from experimental data. (A) Linear fitting for the DTSSP system showing the Langmuir Adsorption isotherm model. (B) Linear fitting for the DSP system showing the Langmuir Adsorption isotherm model.

To understand the best-fit isotherm equation and associated theory for elucidating

adsorption equilibrium behavior of DTSSP and DSP linkers, Langmuir, Temkin, and the Freundlich were chosen. The Langmuir adsorption isotherm model assumes monolayer adsorption on a homogeneous surface with uniform binding sites and no interaction between adsorbed molecules. It was observed that both linkers follow the Langmuir model. The linearized Langmuir plot of 1/Ce versus 1/Qe exhibited excellent correlation for both linkers, DTSSP and DSP. The former exhibited a maximum monolayer adsorption capacity (Qmax) of 48.3 mg/g, greater than DSP (25.73 mg/g). This indicates a higher adsorption capacity of DTSSP on the AuNP surface. Both linkers exhibited similar adsorption affinity toward the Au surface, with KL values of 0.49 L mg^{-1} and 0.48 L mg^{-1} for DTSSP and DSP, respectively. The high correlation coefficients (R^2 = 0.98 for DTSSP and R^2 = 0.99 for DSP) confirm that the Langmuir model accurately describes the adsorption process. Furthermore, the separation factor (RL) values of 0.26 and 0.28 for DTSSP and DSP, respectively, fall within the range of 0 < RL < 1, indicating favorable adsorption.

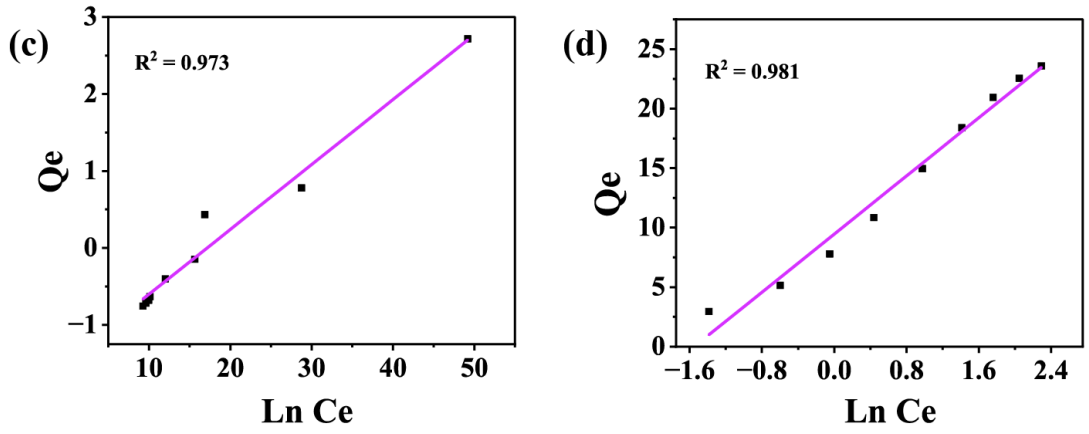

Figure 4.18: Linearized adsorption isotherm plots derived from experimental data. (A) Linear fitting for the DTSSP system showing the Freundlich Adsorption isotherm model. (B) Linear fitting for the DSP system showing the Freundlich Adsorption isotherm model.

The adsorption behavior was further analyzed using the Temkin isotherm model. For DTSSP, the Temkin model showed a strong fit with R^2 = 0.97. The Temkin parameters were determined as A = 3.59 × 10^{-8} and B = 0.084. These values suggest that the adsorption energy changes progressively with increasing DTSSP surface coverage, likely due to linker–linker interactions and occupation of energetically distinct surface sites. For DSP, the Temkin model also provided an excellent fit with R^2 = 0.98. The corresponding parameters were A = 8.54 × 10^{-5} and B = 0.16.

The higher A value suggests a comparatively stronger equilibrium binding parameter, while the larger B value indicates a greater variation in adsorption energy with increasing surface coverage. Overall, DSP exhibited a slightly better agreement with the Temkin model than DTSSP, as shown in (Fig. 4.18 c,d).

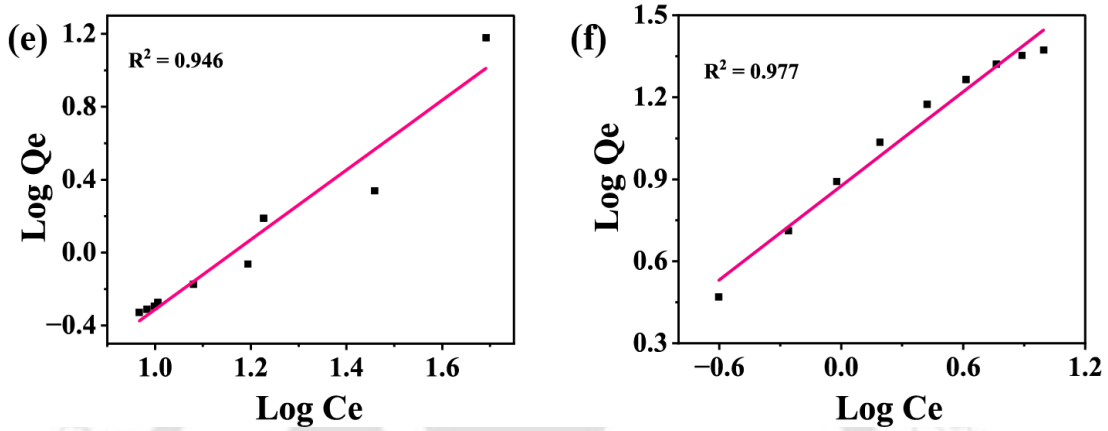

Figure 4.19: Linearized adsorption isotherm plots derived from experimental data. (A) Linear fitting for the DTSSP system showing the Temkin Adsorption isotherm model. (B) Linear fitting for the DSP system showing the Temkin Adsorption isotherm model.

The Freundlich adsorption isotherm, which describes adsorption on heterogeneous surfaces, was also applied to the experimental data. The Freundlich adsorption capacity constant (KF) was determined to be 0.0059 for DTSSP and 7.51 for DSP. The adsorption intensity parameter (n) was found to be 0.52 for DTSSP and 1.74 for DSP. The corresponding correlation coefficients were $R^2 = 0.94$ for DTSSP and $R^2 = 0.97$ for DSP. These results suggest that although both systems show some degree of surface heterogeneity, the Freundlich model provides a weaker fit for DTSSP compared with the Langmuir model. The B parameter, which equals RT/b, reflects the variation in adsorption energy, while the binding constant KT indicates moderate binding affinity. Summary of the values have been mentioned in Table 4.

Table 4: Adsorption isotherm parameters (Langmuir, Freundlich, Temkin) and corresponding R^2 values for DTSSP–AuNP and DSP–AuNP conjugates.

Isotherm Model	Parameter	DTSSP	DSP
Langmuir	Q_{max} (mg g^{-1})	48.3	25.73
	K_L (L mg^{-1})	0.49	0.48
	R_L	0.26	0.28
	R^2	0.98	0.99
Temkin	A	3.59×10^{-8}	8.54×10^{-5}
	B	0.084	0.16
	R^2	0.97	0.98
Freundlich	K_F	0.0059	7.51
	n	0.52	1.74
	R^2	0.94	0.97

Overall, the adsorption parameters clearly establish that both DTSSP and DSP primarily follow Langmuir adsorption behavior. This confirms the monolayer surface functionalization of the AuNPs. DTSSPs exhibit a higher adsorption capacity, whereas DSP demonstrates a more ideal homogeneous monolayer adsorption behavior due to the higher linear fit. Additionally, given the higher correlation coefficients obtained for the Langmuir and Temkin models, the adsorption of both DTSSP and DSP on the AuNP surface can be interpreted in a stepwise manner. Initially, both DTSSP and DSP undergo monolayer adsorption on the AuNP surface, as supported by the strong Langmuir fit, indicating adsorption at a finite number of uniform and equivalent binding sites through Au–S interactions. As the surface becomes progressively occupied, the adsorption process is then followed by changes in binding energy, as evidenced by the good agreement with the Temkin model. This suggests that once the initial monolayer begins to form, the interaction strength gradually changes with increasing surface coverage, likely due to linker–linker interactions, steric crowding, and reduced availability of high-energy binding sites.

4.4 Conclusion

Gold nanoparticles (AuNPs) are among the most widely used nanoprobes for colorimetric sensing due to their sensitive surface plasmon resonance (SPR) response to changes in the local environment. For reliable sensing performance, it is essential to understand the behavior of the bioconjugation linkers that anchor biomolecules such as antibodies and proteins onto the nanoparticle surface. A detailed understanding of linker chemistry and adsorption behavior can significantly improve the accuracy of sensor design and reduce the

time required for empirical optimization of surface functionalization strategies. In this study, two commonly used thiol-based crosslinkers, DTSSP and DSP, were systematically investigated to understand their interaction with gold nanoparticle surfaces. The SPR response of AuNP–linker systems were examined across a range of linker concentrations, enabling the identification of the minimum effective concentrations required for detectable surface modification, which were found to be 3 μM for DTSSP and 6 μM for DSP. Based on the available literature, these concentrations represent the lowest reported linker concentrations at which measurable AuNP surface functionalization and SPR response have been achieved. In addition to the optical characterization, thermodynamic modeling of the adsorption process revealed distinct differences in surface organization between the two linkers. DTSSP exhibited significantly higher surface coverage, indicating dense adsorption and heterogeneous surface organization, whereas DSP displayed behavior closer to ideal monolayer adsorption. These results demonstrate that even subtle structural differences in linker molecules can lead to substantial variations in adsorption density, surface organization, and nanoparticle behavior. Understanding these relationships provides valuable insights for the rational design of nanoparticle–biomolecule interfaces, enabling researchers to select appropriate linkers for biosensing applications and save time more efficiently rather than relying solely on trial-and-error approaches.

Chapter 5

Molecular Dynamics Simulation Insights into Linker-AuNP Interfaces

Abstract

This study presents a comprehensive experimental and molecular dynamics investigation of gold nanoparticle (AuNP) functionalization using two widely employed amine-reactive disulfide crosslinkers, [dithiobis(succinimidyl propionate)] (DSP) and [3,3′-dithiobis(sulfosuccinimidyl propionate)] (DTSSP). The work systematically compares their concentration-dependent adsorption behavior, colloidal stability, surface organization, and optical response to establish mechanistic design principles for AuNP-based colorimetric biosensing platforms. Citrate-reduced AuNPs (~35–40 nm) exhibited a characteristic surface plasmon resonance (SPR) peak at 527 nm. Upon functionalization, it was seen that DTSSP induces aggregation with higher adsorption; DSP maintains colloidal stability. All-atom molecular dynamics simulations (100 ns) provided atomistic insight into these experimental observations. DSP formed a stable, immobilized monolayer characterized by plateau mean square displacement (MSD), homogeneous radial distribution functions (RDFs), and van der Waals-dominated binding energetics. In contrast, DTSSP exhibited enhanced surface mobility, heterogeneous packing, and extended conformations consistent with interparticle bridging. MM/GBSA analysis showed stronger overall binding for DTSSP ($\Delta G \approx -4020$ kcal mol^{-1}) relative to DSP ($\Delta G \approx -2300$ kcal mol^{-1}), driven by favorable solvation and van der Waals interactions; however, the same hydrophilic sulfonate groups that increased binding affinity also facilitated dynamic reorganization and aggregation. The combined computational–experimental framework establishes a direct correlation between linker chemistry, surface mobility, adsorption thermodynamics, and plasmonic behavior. The results demonstrate that subtle structural modifications, especially the introduction of charged sulfonate groups, greatly influence interfacial dynamics and macroscopic optical properties. These findings provide mechanistic guidance for rational linker selection in AuNP-based biosensing, drug delivery, and nano-bio interface engineering.

Keywords: Gold nanoparticles; Molecular dynamics simulation; Linker functionalization

(DSP/DTSSP); Colloidal stability and plasmonic response.

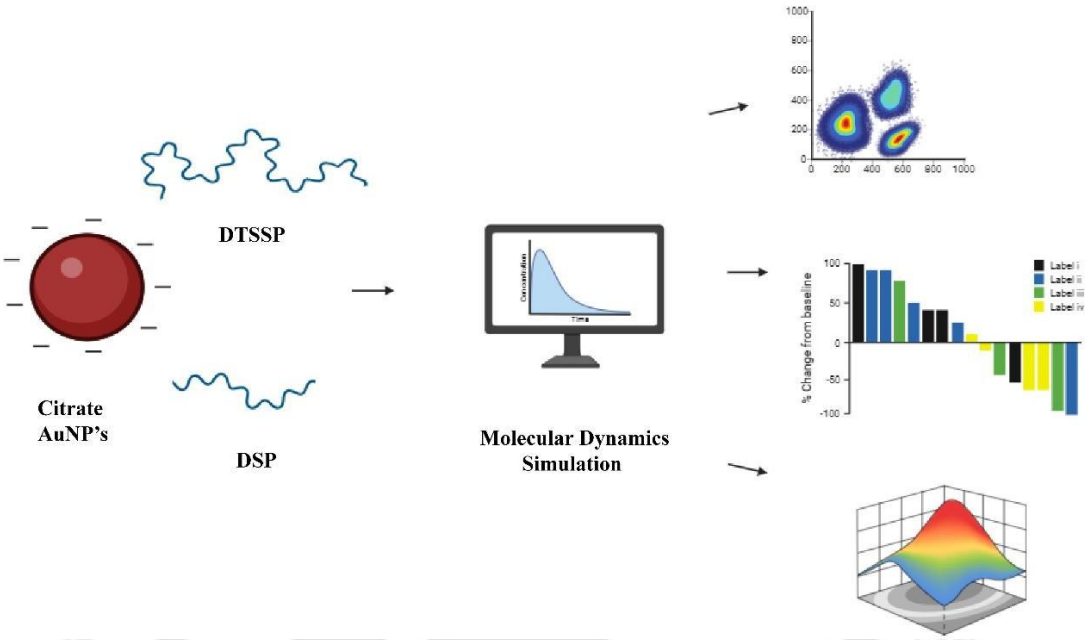

Figure 5.1: Schematic of MD simulation of DTSSP and DSP interactions with citrate-stabilized AuNPs.

5.1 Introduction

The rational design and optimization of functionalized gold nanoparticles for biosensing applications necessitate a fundamental understanding of the molecular-level interactions governing linker–nanoparticle interfaces. While experimental techniques such as transmission electron microscopy, ultraviolet–visible spectroscopy, Fourier-transform infrared spectroscopy, and adsorption isotherm analyses provide macroscopic and ensemble-averaged information about nanoparticle behavior, they often fall short in elucidating the atomistic mechanisms that underlie colloidal stability, surface reorganization, and aggregation phenomena. Computational approaches, particularly all-atom molecular dynamics simulations, have emerged as indispensable tools for bridging this knowledge gap by enabling direct visualization and quantitative analysis of dynamic processes at the nano–bio interface.[201]

Molecular dynamics simulations offer several unique advantages in the study of functionalized metallic nanoparticles. First, they permit the explicit modeling of individual linker molecules, solvent interactions, and surface chemistry at femtosecond temporal resolution and sub-nanometer spatial resolution. Second, simulations allow for the deconstruction of complex energetic phenomena into well-defined components such as van der Waals interactions, electrostatic contributions, and solvation effects, thereby facilitating the interpretation of experimental observables in terms of underlying molecular forces. Third, computational methods enable the systematic exploration of hypothetical scenarios and the prediction of behavior under conditions that may be experimentally inaccessible or prohibitively expensive to investigate.[202]

Despite advances in the experimental characterization of gold nanoparticle functionalization, significant questions remain regarding the mechanistic origins of differential linker behavior. Specifically, the comparative performance of homobifunctional crosslinkers such as dithiobis(succinimidyl propionate) (DSP) and its sulfonated analog 3,3'-dithiobis(sulfosuccinimidyl propionate) (DTSSP) has been documented experimentally, yet the molecular-level phenomena responsible for their contrasting colloidal stability profiles, adsorption kinetics, and plasmonic responses remain incompletely understood. DSP, a lipophilic, membrane-permeable crosslinker with molecular formula $C_{14}H_{16}N_2O_8S_2$ and molecular weight of 404.41 g/mol, features two N-hydroxysuccinimide ester groups connected by an eight-atom spacer arm containing a central disulfide bond. In contrast, DTSSP, with molecular formula $C_{14}H_{14}N_2Na_2O_{14}S_4$ and molecular weight of 608.51 g/mol, incorporates sulfonate groups that confer water solubility and membrane impermeability while maintaining

the disulfide-cleavable architecture.

The present chapter addresses these knowledge gaps by presenting a comprehensive set of all-atom molecular dynamics simulations designed to elucidate the differential behavior of DSP- and DTSSP-functionalized gold nanoparticles. The simulations were undertaken to complement and explain experimental observations of surface plasmon resonance shifts, adsorption isotherm characteristics, colloidal stability, and transmission electron microscopy morphologies reported in previous chapters. By employing a suite of computational analyses including mean residence time calculations, mean square displacement profiling, radial distribution function analysis, and molecular mechanics/generalized Born surface area binding free energy decomposition the simulations provide mechanistic insight into linker retention, surface mobility, spatial organization, and energetic contributions to binding. The rationale for comparing DSP and DTSSP extends beyond their chemical similarity; these linkers represent a model system for understanding how subtle structural modifications, particularly the introduction of charged hydrophilic groups, can profoundly influence nanoscale interfacial dynamics and consequently dictate macroscopic functionality in biosensing platforms.

5.2 Simulation Methodology

5.2.1 Construction of the Gold Nanoparticle Model

The gold nanoparticle model was constructed as a truncated octahedral structure comprising 309 gold atoms, corresponding to an approximate core diameter of 1.0 nm. This particle size was selected to balance computational tractability with experimental relevance, as it falls within the regime where quantum size effects remain moderate yet plasmonic properties are well-developed. The crystallographic structure of the gold core was based on the face-centered cubic lattice of bulk gold, with lattice parameter 4.08 Å. The nanoparticle exposed predominantly (111) facets, consistent with the energetically favorable surface termination observed in experimentally synthesized citrate-reduced gold colloids.[203]

Initial coordinates for the gold nanoparticle were generated using a custom script that carved a truncated octahedron from an extended gold lattice. The particle was subsequently energy-minimized in vacuum using steepest descent minimization followed by conjugate gradient refinement to relax any surface strain induced by truncation. The optimized gold core exhibited a smooth, well-defined surface appropriate for subsequent linker attachment.

5.2.2 Linker Attachment Strategy

DSP and DTSSP linkers were attached to the gold nanoparticle surface via covalent

Au–S coordination bonds, reflecting the well-established chemisorption mechanism by which thiol-containing molecules bind to gold surfaces.[204] The thiol–gold interaction involves oxidative addition of the S–S disulfide bond to the gold surface, yielding thiolate species that coordinate strongly to gold atoms, particularly at undercoordinated surface sites such as step edges and adatoms.[205] The binding energy of thiolate to gold surfaces is approximately 40–50 kcal/mol, sufficient to ensure irreversible adsorption under ambient conditions.

For each system, four linker molecules were symmetrically distributed on the (111) facets of the gold nanoparticle. This surface coverage was chosen to avoid steric crowding while permitting observation of linker–linker interactions and collective reorganization phenomena. The initial linker configurations were generated by manually positioning each molecule with its sulfur atom in proximity to a threefold hollow site on the Au(111) surface, consistent with crystallographic evidence for thiolate adsorption geometry. The alkyl spacer chains connecting the disulfide moiety to the N-hydroxysuccinimide ester groups were initially oriented perpendicular to the surface to facilitate subsequent relaxation into energetically favorable conformations.

For the DSP system, the molecular structure corresponded to 3,3'-dithiobis(succinimidyl propionate) with full atomic detail. For the DTSSP system, sulfonate groups ($–SO_3^-$) were incorporated into the succinimidyl rings, and counterbalancing sodium ions were added to ensure electroneutrality. The inclusion of explicit sulfonate groups and their associated electrostatic interactions constituted a critical structural difference expected to drive differential solvation and mobility behavior.

5.2.3 System Setup, Solvation, and Periodic Boundary Conditions

Each functionalized gold nanoparticle (DSP-AuNP or DTSSP-AuNP) was immersed in a cubic simulation box filled with explicit water molecules, thereby creating a fully solvated system appropriate for studying aqueous-phase interfacial phenomena. The TIP3P water model was employed to represent solvent molecules, consistent with standard practice in biomolecular simulations and previous studies of functionalized gold nanoparticles.[206] TIP3P offers a computationally efficient three-site rigid model that reproduces essential thermodynamic and structural properties of liquid water while maintaining numerical stability during integration of the equations of motion.

The dimensions of the simulation box were chosen such that the minimum distance between the nanoparticle surface and the box boundary was at least 1.5 nm, ensuring that the nanoparticle did not interact with its periodic images under standard cutoff distances for

nonbonded interactions. Periodic boundary conditions were applied in all three Cartesian directions, thereby simulating an infinite system and eliminating spurious surface effects. The water molecules were initially positioned using a pre-equilibrated water box that was overlaid onto the functionalized nanoparticle, with any water molecules overlapping with the solute removed.

To neutralize the net charge of the DTSSP-functionalized system arising from the sulfonate groups, an appropriate number of sodium ions (Na^+) were added to the simulation box, replacing randomly selected water molecules. No additional ions were required for the DSP system, which remained electrically neutral. The ionic strength was maintained at physiologically relevant levels to approximate experimental buffer conditions.

5.2.4 Force Field Parameterization

The force-field parameters for gold atoms were adopted from the model developed by Heinz and co-workers, which provides a consistent description of metallic surfaces and nanoparticle interfaces within classical molecular dynamics simulations. This parameter set is specifically optimized to reproduce experimentally relevant properties of gold, including lattice constants, surface energies, and interfacial interactions with organic ligands. The Heinz force field treats Au–Au interactions using a parameterized Lennard–Jones framework compatible with common biomolecular force fields, enabling accurate representation of gold–thiolate binding environments and ligand–surface adsorption processes. The use of these validated parameters ensures realistic modeling of structural stability and surface energetics of AuNP–linker systems.

5.2.5 Energy Minimization and System Equilibration

Prior to initiating molecular dynamics simulations, each solvated system was subjected to a multistage energy minimization and equilibration protocol designed to relax unfavorable contacts, equilibrate solvent structure, and achieve stable thermodynamic conditions. The minimization phase employed the steepest descent algorithm followed by conjugate gradient minimization until the maximum force on any atom fell below 10 kJ mol^{-1} nm^{-1}. This procedure removed any steric clashes between linker atoms, water molecules, and the gold surface that may have arisen during initial system construction.

Following energy minimization, the system was gradually heated from 0 K to 300 K over a period of 100 ps in the canonical (NVT) ensemble. During this heating phase, position restraints with force constant 1000 kJ mol^{-1} nm^{-2} were applied to the gold core atoms to prevent

structural deformation, while the linker and solvent molecules were allowed to move freely. Temperature control was maintained using the velocity-rescaling (V-rescale) thermostat with a coupling constant of 0.1 ps, which provides efficient and stable temperature regulation without inducing spurious dynamic artifacts.

After reaching the target temperature of 300 K, the system was further equilibrated for 500 ps in the isothermal–isobaric (NPT) ensemble to equilibrate the system density and pressure. Pressure coupling was achieved using the Parrinello–Rahman barostat with a reference pressure of 1 bar, coupling constant of 2.0 ps, and isotropic compressibility of 4.5×10^{-5} bar^{-1}. During NPT equilibration, position restraints on the gold core were maintained to preserve the nanoparticle structure while allowing the simulation box dimensions to adjust in response to thermal expansion and solvent reorganization. The combination of NVT and NPT equilibration ensured that the system attained proper thermodynamic equilibration before data collection commenced.

5.2.6 Production Molecular Dynamics Simulations

Following equilibration, unrestrained molecular dynamics simulations were conducted in the NPT ensemble for a total production time of 100 ns per system. The integration timestep was set to 2 fs, consistent with standard practice for systems employing rigid water models and constraints on bond lengths involving hydrogen atoms. The LINCS algorithm was applied to constrain all bonds, thereby permitting the use of a 2 fs timestep without risk of integration instability.[207]

Temperature and pressure were maintained at 300 K and 1 bar, respectively, throughout the production runs using the V-rescale thermostat and Parrinello–Rahman barostat with the parameters described above. Coordinates were saved every 10 ps, yielding 10,000 snapshots per trajectory for subsequent analysis. Velocities and energies were recorded at the same frequency to enable monitoring of system stability and convergence. The 100 ns production runs provided sufficient sampling to capture linker adsorption dynamics, surface reorganization events, and the establishment of equilibrium distributions for structural and energetic observables. Previous studies of functionalized gold nanoparticles have demonstrated that key dynamic processes such as ligand reorientation and interparticle aggregation occur on timescales ranging from picoseconds to tens of nanoseconds, placing them well within the accessible range of the present simulations.

5.2.7 Trajectory Analysis Methods

The molecular dynamics trajectories were subjected to a comprehensive suite of post-simulation analyses designed to extract mechanistic insights into linker behavior and correlate computational observables with experimental measurements. Four principal analysis techniques were employed: mean residence time (MRT) calculations, mean-square displacement (MSD) profiling, radial distribution function (RDF) analysis, and molecular mechanics/generalized Born surface area (MM/GBSA) binding free-energy decomposition.[208]

Mean Residence Time: The mean residence time quantified the duration for which individual linker molecules remained bound to the gold nanoparticle surface, thereby providing a direct measure of binding stability and surface retention. A linker molecule was defined as bound when the distance between its sulfur atom and the nearest gold surface atom was less than 3.0 Å, corresponding to the first minimum in the sulfur–gold radial distribution function. Residence times were computed by identifying continuous binding events for each linker and averaging over all molecules and over the trajectory. The methodology followed established protocols for residence time calculations from molecular dynamics trajectories, incorporating corrections for transient unbinding events with a duration less than 5 ps.[209]

Mean Square Displacement: The mean square displacement of linker center-of-mass coordinates was computed as a function of lag time to characterize the translational mobility of adsorbed molecules. MSD profiles distinguished between immobilized, diffusive, and dynamic reorganization regimes, with plateau behavior indicative of surface confinement and continuously rising MSD consistent with lateral diffusion or desorption–reabsorption cycles. MSD values were computed using standard ensemble and time averaging procedures to ensure statistical convergence.[201]

Radial Distribution Function: Radial distribution functions were calculated to quantify the spatial organization of linker molecules relative to the gold nanoparticle surface. Two types of RDFs were generated: (i) the center-of-mass radial distribution function, describing the distribution of linker centers of mass as a function of distance from the gold core center, and (ii) the Au–S radial distribution function, describing the distribution of sulfur atoms relative to gold surface atoms. The RDFs provided information on surface packing density, coordination geometry, and the presence of distinct adsorption layers or heterogeneous binding modes.[210]

5.2.8 MM/GBSA Binding Free Energy Decomposition

Binding free energies were estimated using the molecular mechanics/generalized Born surface area approach, which combines molecular mechanics energies with continuum solvation models to approximate the free energy of binding between the linker molecules and

the gold nanoparticle surface. The MM/GBSA method decomposes the total binding free energy, ΔGbind, into contributions from molecular mechanics energy changes (ΔEMM), solvation free energy changes (ΔGsol), and conformational entropy changes (−TΔS):

$$\Delta Gbind = \Delta EMM + \Delta Gsol - T\Delta S \quad \text{Eqn (7)}$$

The molecular mechanics term is further subdivided into bonded, van der Waals, and electrostatic components:

$$\Delta EMM = \Delta Ebonded + \Delta EvdW + \Delta Eelec \quad \text{Eqn (8)}$$

The solvation free energy is partitioned into polar (ΔGGB) and nonpolar (ΔGSA) contributions, with the polar term calculated using the generalized Born model and the nonpolar term estimated from the solvent-accessible surface area:

$$\Delta Gsol = \Delta GGB + \Delta GSA \quad \text{Eqn (9)}$$

Due to the high computational cost of normal mode analysis for entropy estimation and the focus on relative rather than absolute binding affinities, the conformational entropy term was omitted in the present calculations. MM/GBSA calculations were performed on a representative ensemble of snapshots extracted at regular intervals from the production trajectories. This analysis provided quantitative estimates of the energetic driving forces for linker adsorption and enabled direct comparison of DSP and DTSSP binding thermodynamics.[203]

5.3 Results and Discussion

5.3.1 Mean Residence Time and Surface Retention Stability

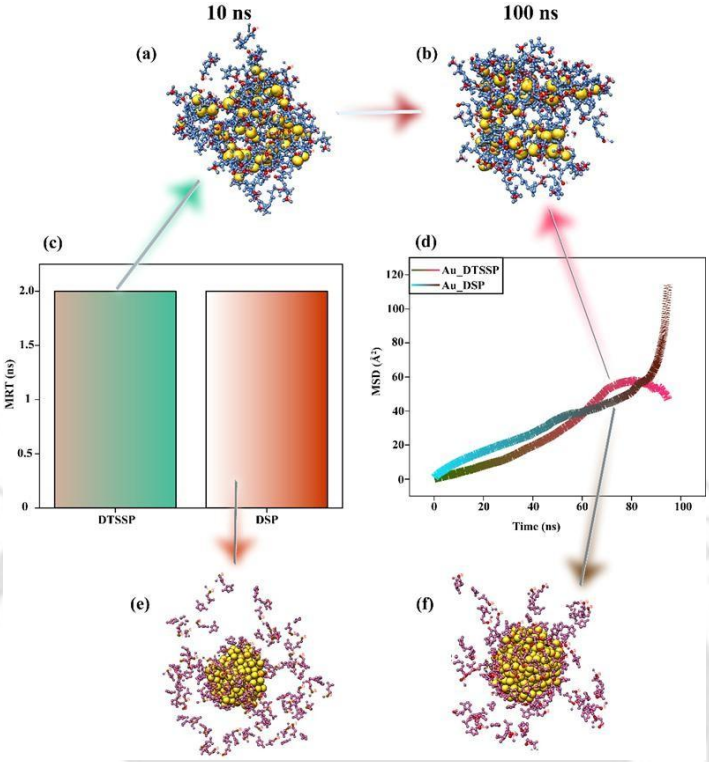

Figure 5.2: Mean residence time, surface mobility, and structural evolution of DSP- and DTSSP-functionalized gold nanoparticles from molecular dynamics simulations.

The mean residence time analysis revealed robust and persistent adsorption of both DSP and DTSSP linkers onto the gold nanoparticle surface, with MRT values approaching 2 ns for both systems. These extended residence times reflected the strength of the chemisorptive Au–S coordination bonds and confirmed that both linkers underwent stable surface binding rather than transient physisorption. The formation of covalent thiolate–gold bonds, characterized experimentally by FTIR spectroscopy through characteristic peaks in the 600–500 cm^{-1} region, ensured that linker molecules remained surface-bound throughout the simulation timescale, consistent with the irreversible adsorption behavior reported in the literature for thiol self-assembled monolayers. The structural evolution and mobility characteristics of the functionalized systems are summarized in Fig. 5.2.

Despite the overall similarity in MRT magnitudes, a subtle but significant difference emerged between the two linkers. DSP exhibited a marginally higher mean residence time relative to DTSSP, suggesting slightly greater retention on the gold nanoparticle surface. This enhanced retention correlated directly with the experimental observation that DSP-functionalized gold nanoparticles maintained stable ultraviolet–visible absorption spectra with

minimal surface plasmon resonance shifts across a wide range of linker concentrations. Specifically, the SPR maximum for DSP-AuNP remained confined to the narrow range of 527–530 nm regardless of DSP concentration, confirming colloidal stability and uniform surface coverage. The stable SPR wavelength indicated that interparticle distances remained sufficiently large to prevent plasmonic coupling, a consequence of the immobilized, spatially homogeneous DSP monolayer that sterically stabilized the colloid.

In contrast, DTSSP displayed a slightly lower mean residence time, which, while still indicative of strong chemisorptive binding, suggested a greater propensity for dynamic surface reorganization relative to DSP. This observation aligned with the experimental observation of concentration-dependent aggregation in DTSSP-functionalized systems, as manifested by pronounced SPR red-shifts from 535 nm at low DTSSP concentrations to 550 nm at elevated concentrations. The red-shift in the SPR maximum is diagnostic of plasmonic coupling between nanoparticles brought into proximity, typically occurring when interparticle separations decrease to distances comparable to or smaller than the particle diameter. The simulation results suggested that the reduced residence time for DTSSP facilitated dynamic surface reorganization and interparticle bridging events, whereby extended DTSSP molecules could span the gap between adjacent nanoparticles, promoting aggregation and the associated optical response. The difference in MRT between DSP and DTSSP, while modest in absolute terms, carried significant mechanistic implications. The marginally reduced retention time for DTSSP likely arose from the presence of the sulfonate groups, which introduced strong electrostatic interactions with the aqueous solvent and enhanced the hydrophilicity of the linker. The favorable solvation of the sulfonate moieties provided a competing energetic contribution that partially offset the stabilization gained from Au–S bonding, thereby facilitating transient unbinding or rearrangement events. Furthermore, the charged character of DTSSP promoted intermolecular electrostatic interactions that could drive linker clustering and heterogeneous surface distributions, contributing to the dynamic character observed in the simulations.

The correlation between mean residence time and experimental adsorption isotherm behavior provided additional mechanistic insight. DSP exhibited excellent agreement with the Langmuir monolayer adsorption isotherm model, yielding a coefficient of determination $R = 0.96$ and Pearson correlation coefficient $r = 0.97$. The Langmuir model assumes adsorption onto a finite number of equivalents, independent surface sites, with each site capable of binding a single adsorbate molecule. The high MRT and uniform surface coverage observed in simulations were consistent with the Langmuir assumption of strong, uniform binding to

discrete sites, with minimal lateral interactions or multilayer formation. The calculated maximum adsorption capacity for DSP, Qmax = 13.34 mg g^{-1} reflected the saturation of available gold surface sites by a monolayer of DSP molecules

Conversely, DTSSP adsorption conformed more closely to the Freundlich isotherm model, with $R^2 = 0.9383$, indicative of heterogeneous adsorption onto a surface with variable binding affinities or the occurrence of multilayer adsorption and aggregation. The Freundlich model accommodates a distribution of binding energies and does not impose a strict saturation limit, consistent with the dynamic reorganization and bridging behavior suggested by the lower mean residence time and elevated mean square displacement observed in DTSSP simulations. The substantially higher maximum adsorption capacity for DTSSP (Qmax = 56.81 mg g^{-1}) reflected the formation of multilayer or bridged structures that extended beyond the monolayer regime accessible to DSP.

5.3.2 Mean Square Displacement and Linker Mobility

The mean square displacement profiles provided a clear mechanistic distinction between the surface mobility regimes of DSP and DTSSP, complementing the residence time analysis with information on lateral diffusion and translational dynamics. For DSP, the MSD exhibited an initial rise to approximately 60 $Å^2$, followed by a pronounced plateau that persisted over the remainder of the simulation trajectory. This plateau behavior was characteristic of molecules that had undergone adsorption onto a surface and subsequently became spatially confined, with their translational motion restricted to localized fluctuations around fixed adsorption sites. The absence of significant long-time growth in the MSD confirmed that DSP linkers remained immobilized on the gold nanoparticle surface following initial binding, with minimal lateral diffusion or desorption–readsorption cycling.

The immobilized monolayer character revealed by the DSP MSD profile correlated directly with experimental evidence of colloidal stability. Transmission electron microscopy images of DSP-functionalized gold nanoparticles displayed well-dispersed, non-aggregated particles even at high DSP concentrations, consistent with the formation of a sterically stabilizing monolayer that prevented interparticle contact. The constant SPR wavelength at 527–530 nm across the concentration range further supported the notion of a stable, immobilized surface layer that maintained uniform interparticle separations and precluded plasmonic coupling. The Langmuir isotherm fit and the moderate adsorption capacity (Qmax=13.34mg/g) reinforced the interpretation of DSP adsorption as a monolayer process wherein molecules occupied available surface sites and became spatially constrained, with

minimal lateral diffusion over extended timescales.

In marked contrast, DTSSP exhibited dramatically different MSD behavior. After an initial rapid rise corresponding to adsorption, the MSD continued to increase, reaching values exceeding 110 Å² before exhibiting fluctuations and a subsequent decline at later simulation frames. This behavior was indicative of transient surface mobility, wherein DTSSP molecules underwent surface rearrangement, potentially including desorption–readsorption cycles, lateral diffusion, and collective reorganization events. The elevated MSD values relative to DSP suggested that DTSSP linkers were not spatially confined to fixed adsorption sites but instead explored a much larger area of the nanoparticle surface or engaged in interparticle bridging configurations.

The dynamic surface reorganization revealed by the DTSSP MSD profile correlated strongly with experimental observations of concentration-dependent aggregation. As DTSSP concentration increased, the progressive SPR red-shift from 535 nm to 550 nm indicated that gold nanoparticles were approaching one another sufficiently closely to allow plasmonic coupling. This aggregation behavior was facilitated by the extended, dynamic DTSSP molecules, which could bridge between neighboring particles and mediate interparticle interactions. Transmission electron microscopy confirmed the formation of linear chain-like assemblies in DTSSP-functionalized systems, a morphology consistent with linker-mediated aggregation wherein mobile, flexible crosslinkers connected discrete nanoparticles into extended networks. The higher adsorption capacity and the superior fit to the Freundlich isotherm supported the interpretation of DTSSP adsorption as a heterogeneous, multilayer, or bridging process in which mobile linkers facilitated extensive surface coverage and interparticle crosslinking.

The mechanistic origin of the differential mobility between DSP and DTSSP resided in their distinct chemical structures and solvation properties. DTSSP incorporated sulfonate groups ($–SO_3^-$) attached to the succinimidyl rings, imparting a substantial negative charge to the molecule and dramatically enhancing its water solubility. The sulfonate moieties engaged in strong electrostatic interactions with water molecules and counterions in the aqueous environment, generating a favorable solvation free energy that partially compensated for the loss of Au–S coordination during transient unbinding events. This enhanced water solubility promoted dynamic surface reorganization by reducing the energetic penalty associated with desorption or rearrangement, thereby facilitating the mobility observed in the MSD profiles. Furthermore, the extended hydration shells surrounding the sulfonate groups introduced steric and electrostatic repulsions between neighboring DTSSP molecules, destabilizing densely

packed monolayer configurations and favoring more heterogeneous, dynamic surface structures.

The flexible spacer arm connecting the disulfide moiety to the succinimidyl ester groups further contributed to the mobility of DTSSP. The propionate chains permitted substantial conformational freedom, allowing DTSSP to adopt extended configurations that could reach across interparticle gaps and mediate aggregation. In contrast, DSP, lacking the charged sulfonate groups, exhibited lower water solubility and stronger association with the hydrophobic regions of the gold–water interface. This hydrophobic character favored immobilization onto the gold surface, with DSP molecules forming a compact, densely packed monolayer stabilized by van der Waals interactions among the alkyl spacer arms and minimal disruption by solvent fluctuations. The combination of reduced solvation energy and favorable lateral packing interactions in DSP resulted in the immobilized, monolayer behavior quantified by the MSD plateau.

5.3.3 Simulation Snapshots and Morphological Evolution

Visual inspection of molecular dynamics trajectory snapshots at early (10 ns) and late (100 ns) simulation timepoints revealed distinct morphological evolution patterns for DSP- and DTSSP-functionalized gold nanoparticles, directly corroborating the quantitative analyses of mean residence time and mean square displacement. For the DSP system, snapshots extracted at both 10 ns and 100 ns exhibited a uniform, densely packed ligand shell with homogeneous surface coverage. The linker molecules remained bound to the gold nanoparticle surface with their alkyl spacer arms oriented approximately perpendicular to the surface, forming a compact monolayer that enveloped the gold core. Minimal interparticle bridging or clustering was observed, consistent with the immobilized, spatially constrained behavior indicated by the MSD plateau.

The stable morphology of the DSP ligand shell persisted throughout the entire simulation timeframe, confirming the immobilized, monolayer character quantified through MRT and MSD profiles. The gold nanoparticle core retained its initial truncated octahedral geometry, with no evidence of surface reconstruction or roughening. The uniform distribution of DSP molecules on the surface, combined with the absence of dynamic reorganization events, supported the interpretation that DSP formed a sterically stabilizing monolayer capable of maintaining colloidal dispersion even at elevated linker concentrations. This morphological observation aligned directly with the experimental TEM images of DSP-conjugated gold nanoparticles, which displayed well-dispersed, spherical particles with uniform size

distribution and no evidence of aggregation or chain formation.

In striking contrast, the DTSSP system exhibited substantial morphological changes over the simulation trajectory. At the early timepoint of 10 ns, the DTSSP-functionalized nanoparticle displayed a relatively uniform surface coverage, with linker molecules distributed across the gold surface in a manner qualitatively similar to the DSP system. However, as the simulation progressed, evidence of linker reorganization, local clustering, and potential interparticle bridging configurations emerged. By 100 ns, the DTSSP ligand shell had adopted a markedly less compact and more heterogeneous structure compared to DSP. Some DTSSP molecules extended further from the gold surface, creating a diffuse, extended corona rather than a densely packed monolayer. Regions of the gold surface exhibited localized aggregation of DTSSP molecules, while other regions displayed reduced coverage, indicative of heterogeneous adsorption and dynamic reorganization.

The extended conformations adopted by DTSSP molecules in the late simulation snapshots were consistent with the elevated MSD values and suggested a mechanism for the interparticle bridging observed experimentally. The flexible propionate spacer arms and the favorable solvation of the sulfonate groups permitted DTSSP molecules to explore extended configurations, wherein one end of the linker remained bound to the original nanoparticle while the other end reached toward neighboring particles or adopted conformations that could facilitate subsequent crosslinking events upon particle approach. This structural heterogeneity and dynamic reorganization provided a molecular-level explanation for the formation of linear chain-like assemblies observed in experimental TEM imaging.

Transmission electron microscopy of DTSSP-conjugated gold nanoparticles confirmed the aggregation behavior predicted by the simulations, revealing linear chain-like assembly's characteristic of linker-mediated interparticle bridging. The chains consisted of individual gold nanoparticles connected in one-dimensional arrays, with interparticle separations consistent with the length of the extended DTSSP linker. The morphological evolution observed in the simulations, from relatively uniform surface coverage at early times to heterogeneous, extended configurations at later times, provided a plausible mechanistic pathway by which DTSSP facilitated aggregation. Initial adsorption of DTSSP onto isolated nanoparticles was followed by dynamic surface reorganization, during which some molecules adopted bridging conformations that could span interparticle gaps. Upon collision or approach of neighboring nanoparticles, these extended DTSSP molecules mediated crosslinking, locking the particles into chain-like assemblies stabilized by multiple linker bridges. The resulting aggregated structures exhibited the pronounced SPR red-shift to 550 nm observed

experimentally, a direct consequence of plasmonic coupling between proximate nanoparticles.

The morphological snapshots thus provided a visual and mechanistic bridge between the quantitative simulation analyses and the macroscopic experimental observables. The stable, densely packed DSP monolayer corresponded to colloidal stability and constant SPR, while the dynamic, heterogeneous DTSSP corona corresponded to aggregation and SPR red-shifts. The simulations captured the early stages of these processes, offering insight into the molecular-level events that preceded and enabled the formation of the extended aggregated structures observed experimentally.

5.3.4 Radial Distribution Function Analysis

Radial distribution function analysis provided quantitative characterization of the spatial organization of linker molecules around the gold nanoparticle surface and elucidated differences in surface packing density and coordination geometry between DSP and DTSSP. The center-of-mass radial distribution function and the Au–S radial distribution function offered complementary perspectives on linker distribution, with the former reflecting the overall spatial extent of the ligand shell and the latter probing the direct coordination environment at the gold–thiolate interface.

For the DTSSP system, the center-of-mass RDF exhibited a sharp, intense peak at approximately 0.6–0.7 nm from the gold core center, followed by smaller features at larger distances. This sharp peak indicated a highly localized population of DTSSP molecules in close proximity to the gold surface, consistent with strong chemisorptive binding and the ability of DTSSP to form dense interfacial layers. The intensity and sharpness of the peak reflected the substantial surface coverage achieved by DTSSP, with multiple molecules adsorbed within a narrow radial shell. The presence of secondary features at larger radial distances suggested the existence of linker molecules in extended conformations or participating in bridging configurations between neighboring particles, consistent with the heterogeneous surface structure observed in simulation snapshots.

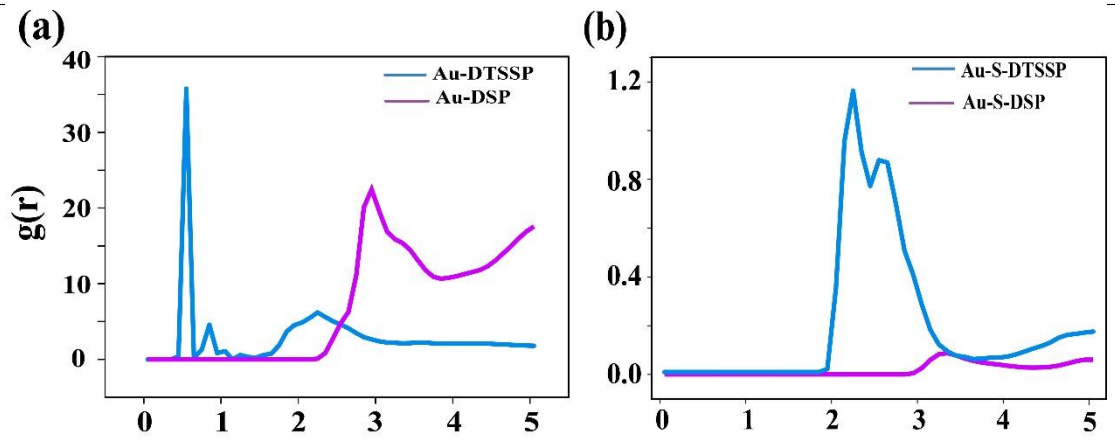

Figure 5.3: (a) Figure 5.3: Radial distribution functions (RDFs) describing (a) linker organization (DTSSP and DSP) at the AuNP interface and (b) chemisorptive anchoring through Au–S contacts.

The corresponding Au–S RDF for DTSSP displayed a broad, high-intensity band between approximately 2.0 and 3.0 Å, confirming the presence of extensive chemisorptive anchoring of DTSSP to the gold nanoparticle surface. The broad peak indicated a distribution of Au–S contact distances rather than a single, well-defined coordination geometry, reflective of the heterogeneous adsorption sites available on the curved nanoparticle surface and the conformational flexibility of the linker molecules. The high intensity of the Au–S peak quantified the large number of closely spaced sulfur–gold contacts, supporting the interpretation that DTSSP formed a densely populated, heterogeneous interfacial structure with multiple linkers simultaneously coordinated to the surface.

These simulation-derived RDF features correlated directly with experimental evidence from Fourier-transform infrared spectroscopy, which demonstrated clear shifts and intensity changes in the carbonyl, amine, and sulfonate vibrational bands upon DTSSP adsorption, along with diagnostic features in the 600–500 cm^{-1} region assigned to Au–S bonding. The presence of the Au–S stretching mode confirmed covalent attachment of DTSSP to gold nanoparticles, while the perturbations in the organic functional group vibrations reflected the constrained environment and altered electronic structure of the surface-bound linker. The dense, heterogeneous interfacial structure revealed by the RDF analysis provided a molecular-level explanation for the pronounced, concentration-dependent SPR red-shifts observed experimentally. The high surface density of DTSSP, combined with the extended conformations and clustering behavior, facilitated interparticle crosslinking and plasmonic coupling, driving the formation of linear chain-like aggregates observed by transmission electron microscopy.

In contrast, the DSP system exhibited markedly different RDF patterns indicative of a more uniformly distributed but less densely packed monolayer. The center-of-mass RDF for

DSP featured a broader, less intense peak centered near 2.8–3.0 nm from the gold core center, with no sharp maxima at shorter distances. The broader peak reflected a wider distribution of linker center-of-mass positions, consistent with a monolayer in which molecules occupied discrete adsorption sites but exhibited conformational variability and lateral separation. The reduced intensity relative to DTSSP indicated a lower surface packing density, consistent with the Langmuir monolayer behavior and the moderate adsorption capacity (Q max = 13.34 mg g^{-1}) determined experimentally further support this interpretation.

The Au–S RDF for DSP was comparatively flat, with only a low-intensity feature emerging at larger distances. This flat profile suggested fewer tightly clustered Au–S contacts and a more homogeneous coverage of isolated thiolate sites. The absence of a sharp, intense Au–S peak indicated that DSP molecules were more spatially dispersed on the gold surface, with each linker occupying a distinct adsorption site and minimal overlap or clustering. This spatial organization was consistent with the immobilized, monolayer character revealed by the MSD plateau and the stable morphology observed in simulation snapshots.

The simulation-derived RDF profiles correlated directly with the experimental ultraviolet–visible spectroscopy and adsorption isotherm data for DSP. The DSP-modified gold nanoparticles displayed nearly constant SPR maxima at approximately 529–530 nm over a wide range of DSP concentrations, indicating that interparticle distances remained large and plasmonic coupling was negligible. The Langmuir-type adsorption behavior, with its characteristic high correlation coefficient and saturation at moderate adsorption capacity, reflected monolayer coverage on equivalent sites, consistent with the homogeneous, sparsely packed Au–S coordination environment revealed by the RDF. Transmission electron microscopy images showing largely dispersed particles with only mild, random aggregation further supported the picture of DSP forming a stable, relatively dilute chemisorbed monolayer that preserved colloidal stability.

Together, the RDF profiles and the experimental data converged on a coherent mechanistic picture: DSP formed a stable, relatively dilute, homogeneous monolayer that preserved colloidal stability through steric repulsion and prevented plasmonic coupling, whereas DTSSP produced a denser, more heterogeneous Au–S coordination environment characterized by extensive chemisorptive binding, local clustering, and extended conformations that promoted interparticle association and the pronounced optical and morphological changes observed experimentally.

5.3.5 MM/GBSA Binding Energy Decomposition

Table 5: MMGBSA binding energy components for DTSSP- and DSP-functionalized AuNP. The total

binding free energy (ΔG) and individual van der Waals, electrostatic, polar solvation (EGB), and nonpolar solvation (SA) terms are reported, highlighting the stronger overall binding of DTSSP compared to DSP and the distinct balance of noncovalent and solvation contributions for each linker.

System	Total ΔG (kcal/mol)	van der Waals (kcal/mol)	Electrostatic (kcal/mol)	Polar solvation, EGB (kcal/mol)	Nonpolar solvation, SA (kcal/mol)
DTSSP	-4020.93	-6807.73	+1,358,040.43	-1,355,185.31	-68.32
DSP	-2300.30	-2430.11	0.00	+177.18	-47.37

Molecular mechanics/generalized Born surface area calculations provided quantitative assessment of the binding free energies and energetic contributions underlying the differential adsorption behavior of DSP and DTSSP on gold nanoparticle surfaces. The MM/GBSA analysis decomposed the total binding free energy into contributions from van der Waals interactions, electrostatic interactions, and solvation effects, thereby elucidating the molecular forces responsible for linker retention, mobility, and surface organization.

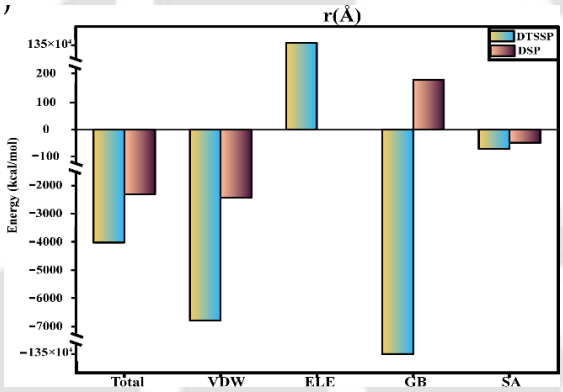

Figure 5.4: (c) Decomposition of MMGBSA binding energies for DTSSP- and DSP-functionalized AuNP. Bar plots compare the total binding free energy (Total) and individual contributions from van der Waals (VDW), electrostatic (ELE), polar solvation (GB), and nonpolar solvation (SA) terms for DTSSP (blue–yellow bars) and DSP (red–purple bars). DTSSP exhibits a more favorable overall binding free energy driven by stronger van der Waals and polar solvation contributions, whereas DSP shows weaker but still favorable binding dominated by van der Waals interactions, consistent with the formation of a stable yet less densely packed monolayer on the AuNP surface.

The total binding free energy for DTSSP was calculated as –4020.93 kcal/mol, substantially more favorable than the corresponding value for DSP of –2300.30 kcal/mol (Fig. 5.4). This nearly twofold enhancement in binding affinity for DTSSP relative to DSP indicated that DTSSP experienced stronger overall interactions with the gold nanoparticle surface. The individual energy components revealed the molecular origins of this enhanced binding; specifically, the interaction is driven by dominant electrostatic and van der Waals contributions, which successfully overcome a substantial unfavorable polar solvation penalty inherent to the highly hydrophilic sulfonate groups of DTSSP.

For DTSSP, the van der Waals contribution amounted to –6807.73 kcal/mol, reflecting extensive favorable dispersive interactions between the linker atoms and the gold surface, as well as among linker molecules themselves in the densely packed interfacial layer. The large magnitude of the van der Waals term was consistent with the high surface coverage and local clustering observed in the RDF analysis and simulation snapshots. The gas-phase electrostatic contribution was calculated at a highly positive +1,358,040.43 kcal/mol; however, in the MM/GBSA framework, this large positive value is strongly coupled with and compensated by the polar solvation term. Rather than indicating net physical repulsion in the bound state, these large opposing values reflect the massive energetic interplay required to desolvate the highly hydrophilic sulfonate groups ($-SO_3^-$) at the interface. Ultimately, the total binding affinity is driven by the combination of these powerful electrostatic interactions and favorable van der Waals forces, which together successfully overcome the high polar solvation penalty associated with shedding the molecule's ordered water shell. These charge-density effects likely contributed to the dynamic reorganization and heterogeneous surface distribution observed in the MSD and morphology analyses, as molecules sought to minimize unfavorable electrostatic contacts through spatial rearrangement.

The polar solvation energy, calculated using the generalized Born model, was strongly negative at –1,355,185.31 kcal mol^{-1}, nearly compensating for the unfavorable electrostatic term. This large favorable solvation energy reflected the strong hydration of the sulfonate groups, which engaged in extensive electrostatic interactions with the aqueous solvent and counterions. The favorable solvation of DTSSP explained the enhanced water solubility and the dynamic surface behavior observed in the simulations: the energetic penalty for desorption or rearrangement was partially offset by the gain in solvation energy as the sulfonate groups became more fully exposed to solvent. The nonpolar solvation term, estimated from solvent-accessible surface area, contributed –68.32 kcal mol^{-1}, reflecting the hydrophobic burial of the alkyl spacer arms upon adsorption. For DSP, the energetic profile differed markedly. The van der Waals contribution was –2430.11 kcal/mol, substantially smaller in magnitude than for DTSSP, consistent with the lower surface coverage and more dispersed monolayer structure revealed by the RDF and MSD analyses. The electrostatic contribution was zero, reflecting the absence of charged functional groups in DSP. The polar solvation term was positive at +177.18 kcal/mol, indicating an unfavorable desolvation penalty upon adsorption, as DSP molecules transitioned from the aqueous phase to the gold surface without the compensating favorable hydration of charged groups. The nonpolar solvation term contributed –47.37 kcal/mol, again reflecting hydrophobic burial of the spacer arms.

The MM/GBSA results explained a critical and initially paradoxical observation: DTSSP exhibited stronger total binding energy yet displayed higher surface mobility and dynamic reorganization relative to DSP. The resolution of this paradox lay in the distinct balance of energetic contributions for the two linkers. For DTSSP, the strong binding energy arose from a combination of extensive van der Waals interactions and highly favorable solvation of the charged sulfonate groups. However, the same structural features that enabled strong binding namely, hydrophilicity, charged character, and conformational flexibility—also facilitated linker reorganization and interparticle bridging. The large favorable solvation energy reduced the energetic barrier for desorption or rearrangement, permitting DTSSP molecules to explore a wide range of surface configurations and extended conformations. Furthermore, the electrostatic repulsions among sulfonate groups destabilized densely packed, uniform monolayers, driving the formation of heterogeneous, dynamic surface structures.

In contrast, DSP exhibited moderate binding energy dominated by van der Waals interactions, with minimal electrostatic contributions and an unfavorable desolvation penalty. The absence of favorable hydration interactions meant that desorption or rearrangement incurred a substantial energetic cost, stabilizing the monolayer configuration and suppressing dynamic reorganization. The hydrophobic character of DSP favored immobilization onto the gold surface, with molecules forming a compact, densely packed monolayer stabilized by lateral van der Waals interactions and minimal disruption by solvent fluctuations. The resulting stable monolayer preserved colloidal stability, as evidenced by constant SPR wavelengths and Langmuir monolayer adsorption behavior.

The MM/GBSA analysis thus provided a molecular-level thermodynamic explanation for the differential behavior of DSP and DTSSP, reconciling the apparently contradictory observations of stronger DTSSP binding yet higher DSP stability. The energetic decomposition highlighted the importance of solvation effects and electrostatic contributions in determining not only binding affinity but also surface mobility, dynamic reorganization, and ultimately the macroscopic colloidal properties of functionalized gold nanoparticles.

5.3.6 Correlation Between Simulation and Experimental Observations

The molecular dynamics simulations presented in this chapter provided a comprehensive mechanistic framework for interpreting the experimental observations reported in Chapter 4. The correlation between computational and experimental observables validated the simulation methodology and demonstrated the utility of molecular dynamics as a tool for elucidating the molecular origins of nanoparticle behavior. In simple terms, DSP forms a stable

protective coating on gold nanoparticles, while DTSSP forms flexible linkers that can connect nanoparticles and cause aggregation.

The mean residence time analysis revealed that DSP exhibited marginally higher surface retention relative to DTSSP, a subtle but mechanistically significant difference that correlated directly with the LSPR behaviour. The stable SPR wavelength at 527–530 nm for DSP-functionalized nanoparticles across a wide concentration range reflected the formation of a stabilizing monolayer that maintained uniform interparticle separations and prevented plasmonic coupling. The high MRT for DSP ensured that linker molecules remained surface-bound and immobilized, preventing dynamic reorganization and bridging events that could mediate aggregation. In contrast, the slightly lower MRT for DTSSP again corresponds to the SPR red-shifts from 535 nm to 550 nm, indicative of progressive aggregation and plasmonic coupling as DTSSP molecules facilitated interparticle bridging.

The mean square displacement profiles provided direct insight into the contrasting colloidal stabilities of the two systems. The MSD plateau observed for DSP quantified the immobilized monolayer character that was visually confirmed by TEM images showing well-dispersed, non-aggregated nanoparticles. The spatial confinement of DSP molecules to fixed adsorption sites prevented the formation of interparticle bridges and preserved colloidal dispersion. Conversely, the elevated and fluctuating MSD for DTSSP correlated with the TEM observations of linear chain-like assemblies, wherein mobile, flexible DTSSP molecules mediated crosslinking between adjacent nanoparticles. The dynamic surface reorganization revealed by the MSD analysis explained the mechanism by which DTSSP facilitated aggregation: transient mobility and extended conformations enabled linker molecules to explore configurations that could span interparticle gaps, locking particles into aggregated structures upon collision.

The radial distribution function analysis quantified the spatial organization of linker molecules and correlated directly with the adsorption isotherm data and FTIR spectroscopy results. For DSP, the broad, low-intensity COM RDF and flat Au–S RDF reflected the formation of a uniform, sparsely packed monolayer consistent with The Langmuir-type adsorption observed for the DSP–AuNP system indicates monolayer coverage on energetically equivalent surface sites. The high correlation coefficient obtained from the Langmuir isotherm fit ($R^2 = 0.9342$), together with the moderate maximum adsorption capacity ($Q_{max} = 13.34$ mg g^{-1}), validates the simulation-based prediction of stable monolayer formation. Furthermore, FTIR spectroscopy confirmed chemisorptive binding of DSP to the AuNP surface through Au–S coordination, providing direct experimental evidence in support of the adsorption model

inferred from both isotherm analysis and molecular dynamics simulations.FTIR spectroscopy confirmed the chemisorptive Au–S bonding through diagnostic peaks in the 600–500 cm^{-1} region, consistent with the RDF evidence for Au–S coordination. For DTSSP, the sharp, intense COM RDF peak and broad, high-intensity Au–S RDF band reflected dense, heterogeneous surface packing, consistent with the Freundlich isotherm behavior ((R^2 = 0.9383) and the elevated adsorption capacity (Qmax=56.81 mg/g). The heterogeneous binding environment captured by the RDF explained the broader applicability of the Freundlich model, which accommodates a distribution of binding affinities rather than assuming a uniform monolayer.

The MM/GBSA binding energy decomposition provided a thermodynamic explanation for the contrasting adsorption behaviors and correlated with the observed differences in colloidal stability and aggregation propensity. The stronger total binding energy for DTSSP (–4020.93 kcal/mol) arose from extensive van der Waals interactions and highly favorable solvation of the sulfonate groups, consistent with the high adsorption capacity and dense surface coverage observed experimentally. However, the same favorable solvation interactions that enhanced binding also facilitated dynamic reorganization and aggregation, as the energetic barrier for desorption or rearrangement was reduced. The moderate binding energy for DSP (–2300.30 kcal/mol), dominated by van der Waals interactions with minimal solvation contributions, stabilized the immobilized monolayer configuration and preserved colloidal stability. This energetic distinction provided a molecular-level rationalization for the experimental observation that DSP maintained stable SPR wavelengths while DTSSP exhibited concentration-dependent aggregation.

The convergence of simulation and experimental results across multiple independent observables residence time and SPR stability, MSD and TEM morphology, RDF and adsorption isotherms, MM/GBSA and aggregation behavior—validated the simulation methodology and established molecular dynamics as a powerful tool for mechanistic interpretation of nanoparticle functionalization. The simulations not only reproduced the qualitative trends observed experimentally but also provided quantitative predictions and molecular-level explanations that were inaccessible to experimental techniques alone. The integrated computational–experimental approach demonstrated in this chapter represents a paradigm for the rational design of functionalized nanoparticles, wherein simulations guide the selection of linker chemistries and surface functionalization strategies to achieve desired macroscopic properties.

5.5 Conclusion

The experimental investigations presented in Chapter 4 demonstrated distinct differences in stability and behavior between various gold nanoparticle–linker systems. To further elucidate the molecular mechanisms underlying these observations, all-atom molecular dynamics simulations were performed on the corresponding AuNP–linker systems. It was revealed that DSP formed a stable, immobilized monolayer characterized by high mean residence time, plateau MSD behavior, homogeneous spatial distribution, and van der Waals-dominated binding. This monolayer architecture conferred colloidal stability by sterically preventing interparticle contact, thereby maintaining constant SPR wavelengths and Langmuir-type adsorption behavior. In contrast, DTSSP exhibited dynamic surface reorganization characterized by slightly lower mean residence time, elevated and fluctuating MSD, dense heterogeneous packing, and strong binding driven by both van der Waals and favorable solvation contributions. The hydrophilic, charged sulfonate groups in DTSSP facilitated dynamic rearrangement and interparticle bridging, driving concentration-dependent aggregation, SPR red-shifts, and Freundlich-type adsorption behavior.

The radial distribution function analysis quantified the spatial organization of the two linkers, revealing sparse, homogeneous monolayer coverage for DSP and dense, heterogeneous multilayer or bridging structures for DTSSP. The MM/GBSA binding energy decomposition explained the apparent paradox of stronger DTSSP binding yet greater DSP stability, demonstrating that favorable solvation interactions in DTSSP both enhanced binding affinity and facilitated dynamic reorganization, while van der Waals-dominated DSP binding stabilized the immobilized monolayer configuration. The simulation results correlated directly with experimental observations from ultraviolet–visible spectroscopy, transmission electron microscopy, Fourier-transform infrared spectroscopy, and adsorption isotherm analyses, establishing molecular dynamics as a validated tool for mechanistic interpretation and predictive design of functionalized gold nanoparticles.

The mechanistic insights obtained from these simulations transcended the specific case of DSP and DTSSP, offering broader principles for understanding nano–bio interfaces. The critical role of hydrophilic functional groups in modulating surface mobility and aggregation propensity, the balance between binding affinity and dynamic reorganization, and the relationship between spatial organization and colloidal stability represent general design principles applicable to a wide range of linker chemistries and nanoparticle systems. The simulations demonstrated that subtle structural modifications such as the introduction of charged sulfonate groups can profoundly influence interfacial dynamics and macroscopic functionality, underscoring the importance of molecular-level design in nanoparticle

engineering.

Chapter 6

Future Scopes and Perspectives

The work presented in Chapter 2 opens several future directions, particularly toward the development of practical allantoin biosensors and broader protein-engineering strategies for immobilized enzymes. The structural and functional data obtained for the allantoinase enzyme can be used to facilitate its effective immobilization on suitable sensing platforms, thereby enabling the translation of this system into a potential point-of-care diagnostic device for allantoin detection. In particular, to develop immediate and experimental directions, express and purify top-ranked bacterial allantoinases (e.g., *Escherichia* and *Streptomyces* candidates with favourable solubility, instability index, and extinction coefficients) and validate the predicted stability and activity experimentally. Optimize immobilization protocols (physisorption, sol–gel entrapment, polymer matrices, low-dimensional nanomaterials) using the identified parameters. Systematic comparison can be done for different supports (e.g., graphene, silica, porous polymers, nitrocellulose) to test how intrinsic volume, sphericity, and hydrophobicity translate into real adsorption efficiency and retained catalytic activity.

Future work can focus on developing prototype allantoin biosensors, either optical or electrochemical, using the shortlisted allantoinase enzymes and evaluating key performance parameters such as limit of detection (LOD), linear detection range, response time, operational stability, storage stability, and reusability in relevant biological fluids, including serum and urine. The active-site residue mapping and identification of conserved titratable residues such as His, Asp, and Trp can further guide rational modifications to tune the pH response and sensitivity of the enzyme, for example through targeted mutagenesis at positions influencing structural flexibility and hydrophobic clustering. In addition, the observed thermostability and high aliphatic index of the enzyme provide opportunities to design sensors capable of functioning under elevated temperatures or harsh environmental conditions, which is advantageous for point-of-care diagnostics in low-resource settings as well as for long-term implantable or wearable biosensing platforms.

In broader biological and diagnostic contexts, this work can serve as a model framework for identifying hidden structural and functional trends within an enzyme or an enzyme family, particularly in cases where simulating hundreds of enzyme variants is computationally impractical. By applying the analytical approach demonstrated here, researchers can extract key structural patterns and gain insight into the conformational behavior, stability, and

functional features of related enzymes, thereby guiding targeted investigations and rational design strategies within large enzyme families.

Future work can also systematically investigate how agarose concentration, buffer composition, and electric field strength modulate pore size evolution and DNA migration dynamics using the combined electrophoretic–SEM workflow established in this chapter. Building on early demonstrations that agarose-gel pore architecture critically governs size-dependent separation[211] and on later mechanistic analyses of DNA transport in gels and free solution.[152] Advanced imaging modalities such as cryo-SEM or confocal laser scanning microscopy could be employed to visualize hydrated gel networks and capture in situ structural changes under an applied field. Coupling these structural insights with theoretical and computational descriptions of polymer networks and polyelectrolyte migration would enable predictive control over gel design, facilitating the optimization of resolution and run time for specific fragment size ranges in both conventional slab gels and miniaturized or microfluidic electrophoresis platforms.

The present study establishes a systematic framework for understanding how DTSSP and DSP linkers interact with citrate-stabilized gold nanoparticles and how these interactions govern colloidal stability and optical response. Building on these findings, future work can focus on translating the optimized AuNP–linker systems into practical biosensing platforms. This includes extending the current proof-of-concept to real biological targets such as small-molecule metabolites, proteins, or clinically relevant biomarkers, and rigorously determining analytical performance parameters such as limit of detection, linear dynamic range, selectivity, and robustness in complex matrices. By directly coupling the observed concentration-dependent SPR shifts and aggregation behaviour with quantifiable sensing metrics, the system can be evolved from a fundamental model into a reliable colorimetric assay suitable for point-of-care or laboratory diagnostics.

In addition, the insights gained into linker-dependent adsorption capacity, surface coverage, and colloidal stability create an opportunity to rationally design new linker architectures. Future studies can systematically vary structural features such as spacer length, charge density, hydrophilicity, and multivalency to establish clear structure–property relationships for Au–thiolate interfaces. These modified linkers could be combined in mixed self-assembled layers, for example, co-adsorbing DTSSP or DSP with polyethylene glycol or zwitterionic thiols, in order to fine-tune the balance between high biofunctional loading and resistance to non-specific adsorption. Such engineered monolayers would help decouple

sensitivity from stability, thereby improving reproducibility of localized surface plasmon resonance responses under high ionic strength and physiologically relevant conditions.

The current all-atom molecular dynamics simulations provide detailed mechanistic insight at the single-particle level, particularly regarding residence time, mobility, and spatial organization of linkers at the AuNP surface. A logical future extension is to expand these simulations toward multi-particle assemblies, enabling the direct visualization of linker-mediated aggregation pathways and hotspot formation that underlie the experimentally observed red shifts and chain-like morphologies. Coupling atomistic simulations with coarse-grained or continuum-scale models will allow prediction of how microscopic parameters such as binding free energy, coverage kinetics, and radial distribution functions propagate to macroscopic observables like aggregation rate, hydrodynamic size, and optical spectra. In this way, simulation can evolve into a predictive design tool for screening linker candidates and optimizing conjugation protocols before experimental implementation.

On the experimental side, further refinement of the adsorption and kinetic models will strengthen the theoretical description of the AuNP–linker system. Temperature-dependent adsorption studies, combined with time-resolved UV–Vis spectroscopy, dynamic light scattering, and nanoparticle tracking analysis, can be used to extract thermodynamic parameters and to directly link the evolution of surface coverage with colloidal aggregation and SPR shift dynamics. Beyond the classical Langmuir, Freundlich, and Temkin approaches, the application of more sophisticated isotherm and kinetic models will help to resolve heterogeneity in binding sites, multilayer formation, and diffusion-controlled processes. This multi-model treatment will provide a more nuanced mechanistic picture, allowing future researchers to choose linker type and conjugation conditions based on quantitative criteria rather than empirical trial-and-error.

Finally, to move toward real-world impact, the optimized DTSSP- and DSP-functionalized AuNPs should be benchmarked against established conjugation chemistries and evaluated under realistic operational conditions. Comparative studies with widely used systems such as MUA/EDC–NHS, maleimide–thiol, and biotin–streptavidin linkages will clarify the advantages and limitations of each linker in terms of stability, signal-to-noise ratio, and ease of fabrication. Parallel efforts should address the scalability of nanoparticle synthesis, batch-to-batch reproducibility, storage stability, and performance in complex clinical samples such as serum or tear fluid. By systematically addressing these translational aspects, the present work can evolve into a robust platform for the development of next-generation

colorimetric and plasmonic biosensors suitable for decentralized diagnostics and other biomedical applications.

References

(1) Elsayed Azab, A.; A Adwas, Almokhtar; Ibrahim Elsayed, A. S.; A Adwas, A.; Ibrahim Elsayed, Ata Sedik; Quwaydir, F. A. Oxidative Stress and Antioxidant Mechanisms in Human Body. *Journal of Applied Biotechnology & Bioengineering* **2019**, *6* (1), 43–47. https://doi.org/10.15406/jabb.2019.06.00173.

(2) Birben, E.; Sahiner, U. M.; Sackesen, C.; Erzurum, S.; Kalayci, O. *Oxidative Stress and Antioxidant Defense*.

(3) Xu, Z.; Yang, S.; Tan, Y.; Zhang, Q.; Wang, H.; Tao, J.; Liu, Q.; Wang, Q.; Feng, W.; Li, Z.; Wang, C.; Cui, L. Inflammation in Cardiovascular-Kidney-Metabolic Syndrome: Key Roles and Underlying Mechanisms–a Comprehensive Review. *Mol. Cell. Biochem.* **2025**, *480* (12), 6039–6075. https://doi.org/10.1007/s11010-025-05379-9.

(4) Purkayastha, S.; Cai, D. Neuroinflammatory Basis of Metabolic Syndrome. *Molecular Metabolism*. Elsevier GmbH 2013, pp 356–363. https://doi.org/10.1016/j.molmet.2013.09.005.

(5) Zhang, J.; Wang, X.; Vikash, V.; Ye, Q.; Wu, D.; Liu, Y.; Dong, W. ROS and ROS-Mediated Cellular Signaling. *Oxidative Medicine and Cellular Longevity*. Hindawi Limited 2016. https://doi.org/10.1155/2016/4350965.

(6) Li, Y. R.; Trush, M. Defining ROS in Biology and Medicine. *Reactive Oxygen Species* **2016**, *1* (1). https://doi.org/10.20455/ros.2016.803.

(7) Milne, G. L.; Musiek, E. S.; Morrow, J. D. F2-Isoprostanes as Markers of Oxidative Stress in Vivo: An Overview. *Biomarkers : biochemical indicators of exposure, response, and susceptibility to chemicals*. 2005, pp 10–23. https://doi.org/10.1080/13547500500216546.

(8) Davies, S. S.; Roberts, L. J. F2-Isoprostanes as an Indicator and Risk Factor for Coronary Heart Disease. *Free Radical Biology and Medicine*. March 1, 2011, pp 559–566. https://doi.org/10.1016/j.freeradbiomed.2010.11.023.

(9) Alguno, A. C.; Capangpangan, R. Y.; Dumancas, G. G.; Lubguban, A. A.; Malaluan, R. M.; Rivera, R. B. P. Synthesis of Gold Nanoparticles. In *Gold Nanoparticles. Engineering Materials*; Springer: Singapore, 2025; pp 13–29. https://doi.org/10.1007/978-981-96-6565-5_2.

(10) Pozzi, M.; Jonak Dutta, S.; Kuntze, M.; Bading, J.; Rüßbült, J. S.; Fabig, C.; Langfeldt, M.; Schulz, F.; Horcajada, P.; Parak, W. J. Visualization of the High Surface-to-Volume Ratio of Nanomaterials and Its Consequences. *J. Chem. Educ.* **2024**, *101* (8), 3146–3155. https://doi.org/10.1021/acs.jchemed.4c00089.

(11) Kumalasari, M. R.; Alfanaar, R.; Andreani, A. S. Gold Nanoparticles (AuNPs): A Versatile Material for Biosensor Application. *Talanta Open* **2024**, *9*, 100327. https://doi.org/10.1016/j.talo.2024.100327.

(12) BarathManiKanth, S.; Kalishwaralal, K.; Sriram, M.; Pandian, S. R. K.; Youn, H.; Eom, S.; Gurunathan, S. Anti-Oxidant Effect of Gold Nanoparticles Restrains Hyperglycemic Conditions in Diabetic Mice. *J. Nanobiotechnology* **2010**, *8* (1), 16. https://doi.org/10.1186/1477-3155-8-16.

(13) Fuentes-Chust, C.; Parolo, C.; Piper, A.; Merkoçi, A. Stability Matters: Evaluating the Long-Term Performance of AuNP–DNA Conjugates in Lateral Flow Assays through Varied Conjugation Methods and Storage Buffers. *Nanoscale* **2025**, *17* (27), 16423–16431. https://doi.org/10.1039/D4NR05328A.

(14) Zhang, P.; Hou, H.; Xu, S.; Wen, Y.; Zhang, Y.; Xing, F. Localized Surface Plasmon Resonance Sensing Based on Monometallic Gold Nanoparticles: From Material Preparation to Detection of Bioanalytes. *Analytical Methods*. Royal Society of Chemistry December 18, 2024. https://doi.org/10.1039/d4ay01509f.

(15) Zeng, L.; Zhou, M.; Jin, R. Evolution of Excited-State Behaviors of Gold Complexes, Nanoclusters and Nanoparticles. *ChemPhysChem* **2024**, *25* (13). https://doi.org/10.1002/cphc.202300687.

(16) Yu, W.; Yang, C.; Min, H.; Liu, H.; Ma, Y.; Yu, Z.; Yuan, S.; Dong, H.; Wang, K.; Song, B.; Feng, J. Cavity Effect of Gold Nanoparticles on Mid-Infrared Light. *ACS Omega* **2025**, *10* (12), 12163–12169. https://doi.org/10.1021/acsomega.4c10454.

(17) Shukla, N.; Chetri, P.; Boruah, R.; Gogoi, A.; Ahmed, G. A. Surface Plasmon Resonance Biosensors Based on Kretschmann Configuration: Basic Instrumentation and Applications. In *Recent Advances in Plasmonic Probes*; Springer, 2022; pp 191–222. https://doi.org/10.1007/978-3-030-99491-4_6.

(18) Bhatia, P.; Verma, S. S. Enhancement of LSPR Properties of Temperature-Dependent Gold Nanoparticles. *Mater. Today Proc.* **2023**, *78*, 871–876. https://doi.org/10.1016/j.matpr.2022.12.020.

(19) Li, Y.; Liu, L.; Xu, Z.; Zhang, J.; Chen, L. Study on AuNPs Size Regulation and AuNPs/BP Photocatalytic Performance. *Opt. Mater. (Amst).* **2022**, *125*, 112133. https://doi.org/10.1016/j.optmat.2022.112133.

(20) Yang, W.; Xia, B.; Wang, L.; Ma, S.; Liang, H.; Wang, D.; Huang, J. Shape Effects of Gold Nanoparticles in Photothermal Cancer Therapy. *Materials Today Sustainability* **2021**, *13*, 100078. https://doi.org/10.1016/j.mtsust.2021.100078.

(21) Zhou, W.; Hu, K.; Kwee, S.; Tang, L.; Wang, Z.; Xia, J.; Li, X. Gold Nanoparticle Aggregation-Induced Quantitative Photothermal Biosensing Using a Thermometer: A Simple and Universal Biosensing Platform.

Anal. Chem. **2020**, *92* (3), 2739–2747. https://doi.org/10.1021/acs.analchem.9b04996.
(22) Li, M.; Yang, K. The Refractive Index Sensing Performance of Au and Ag Nanoparticles Under Different Surrounding Environment. *Particle & Particle Systems Characterization* **2024**, *41* (4). https://doi.org/10.1002/ppsc.202300143.
(23) Sarfraz, N.; Khan, I. Plasmonic Gold Nanoparticles (AuNPs): Properties, Synthesis and Their Advanced Energy, Environmental and Biomedical Applications. *Chemistry - An Asian Journal*. John Wiley and Sons Ltd April 1, 2021, pp 720–742. https://doi.org/10.1002/asia.202001202.
(24) Anjali Devi, J. S.; Madanan Anju, S.; Lekha, G. M.; Aparna, R. S.; George, S. Luminescent Carbon Dots *versus* Quantum Dots and Gold Nanoclusters as Sensors. *Nanoscale Horiz.* **2024**, *9* (10), 1683–1702. https://doi.org/10.1039/D4NH00107A.
(25) Epple, M.; Rotello, V. M.; Dawson, K. The Why and How of Ultrasmall Nanoparticles. *Acc. Chem. Res.* **2023**, *56* (23), 3369–3378. https://doi.org/10.1021/acs.accounts.3c00459.
(26) Yang, Y.; Zhai, S.; Zhang, L.; Wu, Y.; Li, J.; Li, Y.; Li, X.; Zhu, L.; Xu, W.; Wu, G.; Gao, H. A Gold Nanoparticle-Enhanced DCas9-Mediated Fluorescence Resonance Energy Transfer for Nucleic Acid Detection. *Talanta* **2025**, *282*, 126978. https://doi.org/10.1016/j.talanta.2024.126978.
(27) Pajović, J. D.; Dojčilović, R. J.; Kaščáková, S.; Réfrégiers, M.; Božanić, D. K.; Djoković, V. Enhanced Resonance Energy Transfer in Gold Nanoparticles Bifunctionalized by Tryptophan and Riboflavin and Its Application in Fluorescence Bioimaging. *Colloids Surf. B Biointerfaces* **2023**, *227*, 113340. https://doi.org/10.1016/j.colsurfb.2023.113340.
(28) Chaparro, D.; Goudeli, E. Design of Engineered Nanoparticles for Biomedical Applications by Computational Modeling. *Nanoscale* **2025**, *17* (16), 9705–9737. https://doi.org/10.1039/D4NR05199H.
(29) Obijiofor, O. C.; Novikov, A. S. Exploring the Role of Density Functional Theory in the Design of Gold Nanoparticles for Targeted Drug Delivery: A Systematic Review. *J. Mol. Model.* **2025**, *31* (7), 186. https://doi.org/10.1007/s00894-025-06405-9.
(30) Rujiralai, T.; Leelaharat, N.; Cheewasedtham, W. Highly Specific Colorimetric Detection Based on Aggregation of <scp>l</Scp> -Cysteine Functionalized Gold Nanoparticles for Cypermethrin in Water Samples. *RSC Adv.* **2024**, *14* (13), 9175–9183. https://doi.org/10.1039/D3RA07626A.
(31) Onifade, O. A.; Mohamad Azri, D. D.; Abu Bakar, M. H.; Alresheedi, M. T.; Ng, E. K.; Mahdi, M. A.; Muhammad Noor, A. S. Surface Functionalized Plasmonic Sensors for Uric Acid Detection With Gold-Graphene Stacked Nanocomposites. *Photonic Sensors* **2025**, *15* (1), 250132. https://doi.org/10.1007/s13320-024-0751-z.
(32) Wang, W.; Zhang, B.; Zhang, Y.; Ma, P.; Wang, X.; Sun, Y.; Song, D.; Fei, Q. Colorimetry and SERS Dual-Mode Sensing of Serotonin Based on Functionalized Gold Nanoparticles. *Spectrochim. Acta A Mol. Biomol. Spectrosc.* **2021**, *261*, 120057. https://doi.org/10.1016/j.saa.2021.120057.
(33) Kim, S.; Kim, M.-G. Automatically Signal-Enhanced Lateral Flow Immunoassay for Ultrasensitive Salivary Cortisol Detection. *Anal. Chem.* **2025**, *97* (5), 2707–2713. https://doi.org/10.1021/acs.analchem.4c04700.
(34) Ye, Y.; Hou, S.; Wu, X.; Cheng, X.; He, S. Freeze-Driven Adsorption of Poly-A DNA on Gold Nanoparticles: From a Stable Biointerface to Plasmonic Dimers. *Langmuir* **2022**, *38* (15), 4625–4632. https://doi.org/10.1021/acs.langmuir.2c00007.
(35) Ma, X.; Li, X.; Luo, G.; Jiao, J. DNA-Functionalized Gold Nanoparticles: Modification, Characterization, and Biomedical Applications. *Front. Chem.* **2022**, *10*. https://doi.org/10.3389/fchem.2022.1095488.
(36) Qin, Z.; Tao, X.; Pang, Y.; Jiang, M.; Song, Y.; Song, E. Antiprotein Corona-Fouling Effect of the Double-Stranded DNA Coating Layer on the Gold Nanoparticles-Small Molecule Adsorbent Probe. *Anal. Chem.* **2025**, *97* (6), 3773–3780. https://doi.org/10.1021/acs.analchem.5c00260.
(37) Alarcón-Iniesta, H.; de Arana, G.; López-Valls, M.; Pardo, D.; Escalona-Noguero, C.; Rodríguez, C.; Castellanos, M.; Cobelo, S.; Martínez-Ramírez, I.; Camarero, J.; Heras, S. de las; de Vicente, J.; Valera, A.; Smith, W.; Bernardo-Gavito, R.; Cantón, R.; Galán, J. C.; Granados, D.; Miranda, R.; Guerrero, H.; Sot, B. CRISPR-Associated Plasmonic Colorimeter Method (Ca-PCM): A Real-Time RGB Detection System for Gold Nanoparticles-Based Nucleic Acid Biosensors. *Anal. Chim. Acta* **2025**, *1338*, 343601. https://doi.org/10.1016/j.aca.2024.343601.
(38) Ding, Y.; Huang, P.-J. J.; Zandieh, M.; Wang, J.; Liu, J. Gold Nanoparticles Synthesized Using Various Reducing Agents and the Effect of Aging for DNA Sensing. *Langmuir* **2023**, *39* (1), 256–264. https://doi.org/10.1021/acs.langmuir.2c02458.
(39) Ye, H.; Chen, X.; Huang, X.; Li, C.; Yin, X.; Zhao, W.; Wang, T. Patterned Gold Nanoparticle Superlattice Film for Wearable Sweat Sensors. *Nano Lett.* **2024**, *24* (35), 11082–11089. https://doi.org/10.1021/acs.nanolett.4c03254.
(40) Huang, Y.; Montes-García, V.; Stoeckel, M.; Von Holst, M.; Ciesielski, A.; Samorì, P. Highly Sensitive Strain Sensors Based on Molecules–Gold Nanoparticles Networks for High-Resolution Human

Pulse Analysis. *Small* **2021**, *17* (8). https://doi.org/10.1002/smll.202007593.
(41) Ramesh, A. M.; Rajesh, M.; Chandran, A.; Surendran, K. P. Gold-Nanoparticle-Based Flexible Humidity Sensor for Breath Monitoring and Smart Irrigation Systems. *ACS Appl. Nano Mater.* **2024**, *7* (13), 15593–15605. https://doi.org/10.1021/acsanm.4c02603.
(42) Oh, H.-K.; Kim, K.; Park, J.; Im, H.; Maher, S.; Kim, M.-G. Plasmon Color-Preserved Gold Nanoparticle Clusters for High Sensitivity Detection of SARS-CoV-2 Based on Lateral Flow Immunoassay. *Biosens. Bioelectron.* **2022**, *205*, 114094. https://doi.org/10.1016/j.bios.2022.114094.
(43) Olszewska, P.; Spietelun, M.; Syguła, K.; Ossowski, A.; Grygorcewicz, B. Bacteriophages as a Modern Diagnostic Tool: Innovations, Applications and Challenges. *Mol. Biol. Rep.* **2025**, *52* (1), 997. https://doi.org/10.1007/s11033-025-10967-5.
(44) Sekar, V.; Santhanam, A.; Arunkumar, P. A Low-Cost Paper and Solution Based Colorimetric Detection of Bacteria Using Glucose-Functionalized Gold Nanoparticles. *Journal of Water Process Engineering* **2024**, *59*, 105102. https://doi.org/10.1016/j.jwpe.2024.105102.
(45) Mohajeri, S.; Moayedi, S.; Azimi, L.; Akrami, M.; Rad-Malekshahi, M.; Fazeli, M. R.; Fallah, F.; Haririan, I. Nanobiosensor Based on Sugar Code-AuNPs Aggregation: A Key to Opening New Gates in Rapid Diagnosis of Streptococcal Pharyngitis. *Front. Bioeng. Biotechnol.* **2022**, *10*. https://doi.org/10.3389/fbioe.2022.957271.
(46) Rivera, R. B. P.; Unabia, R. B.; Reazo, R. L. D.; Lapening, M. A.; Lumod, R. M.; Ruda, A. G.; Omping, J. L.; Magdadaro, M. R. D.; Sayson, N. L. B.; Latayada, F. S.; Capangpangan, R. Y.; Dumancas, G. G.; Malaluan, R. M.; Lubguban, A. A.; Petalcorin, G. C.; Alguno, A. C. Influence of the Gold Nanoparticle Size on the Colorimetric Detection of Histamine. *ACS Omega* **2024**, *9* (31), 33652–33661. https://doi.org/10.1021/acsomega.4c02023.
(47) Thanunchai, M.; Sangboonruang, S.; Semakul, N.; Kumthip, K.; Maneekarn, N.; Tragoolpua, K. Aptamer-Functionalized Gold Nanoparticle Assay for Rapid Visual Detection of Norovirus in Stool Samples. *Biosensors (Basel).* **2025**, *15* (6), 387. https://doi.org/10.3390/bios15060387.
(48) Peng, H.; Borg, R. E.; Nguyen, A. B. N.; Chen, I. A. Chimeric Phage Nanoparticles for Rapid Characterization of Bacterial Pathogens: Detection in Complex Biological Samples and Determination of Antibiotic Sensitivity. *ACS Sens.* **2020**, *5* (5), 1491–1499. https://doi.org/10.1021/acssensors.0c00654.
(49) Figat, A. M.; Bartosewicz, B.; Liszewska, M.; Budner, B.; Norek, M.; Jankiewicz, B. J. α-Amino Acids as Reducing and Capping Agents in Gold Nanoparticles Synthesis Using the Turkevich Method. *Langmuir* **2023**, *39* (25), 8646–8657. https://doi.org/10.1021/acs.langmuir.3c00507.
(50) Rashid, U.; Bro-Jørgensen, W.; Harilal, K.; Sreelakshmi, P.; Mondal, R. R.; Chittari Pisharam, V.; Parida, K. N.; Geetharani, K.; Hamill, J. M.; Kaliginedi, V. Chemistry of the Au–Thiol Interface through the Lens of Single-Molecule Flicker Noise Measurements. *J. Am. Chem. Soc.* **2024**, *146* (13), 9063–9073. https://doi.org/10.1021/jacs.3c14079.
(51) Okyem, S.; Awotunde, O.; Ogunlusi, T.; Riley, M. B.; Driskell, J. D. Probing the Mechanism of Antibody-Triggered Aggregation of Gold Nanoparticles. *Langmuir* **2021**, *37* (9), 2993–3000. https://doi.org/10.1021/acs.langmuir.1c00100.
(52) Xu, J. X.; Alom, Md. S.; Yadav, R.; Fitzkee, N. C. Predicting Protein Function and Orientation on a Gold Nanoparticle Surface Using a Residue-Based Affinity Scale. *Nat. Commun.* **2022**, *13* (1), 7313. https://doi.org/10.1038/s41467-022-34749-w.
(53) Zhang, S.; Wang, Z.; Miao, T. Tryptophan-Functionalized Gold Nanoclusters Used as a Fluorescence Sensor for Alizarin Determination. *Spectrochim. Acta A Mol. Biomol. Spectrosc.* **2025**, *335*, 125963. https://doi.org/10.1016/j.saa.2025.125963.
(54) Ozaki, M.; Yoshida, S.; Oura, M.; Tsuruoka, T.; Usui, K. Effect of Tryptophan Residues on Gold Mineralization by a Gold Reducing Peptide. *RSC Adv.* **2020**, *10* (66), 40461–40466. https://doi.org/10.1039/D0RA07098J.
(55) Kim, J.; Min, K. Assembly and Biomineralization of Polymorphic Gold–Peptide Superstructures Using Tyrosine-Rich Short Peptides. *Adv. Funct. Mater.* **2023**, *33* (4). https://doi.org/10.1002/adfm.202210196.
(56) Ditta, S. A.; Yaqub, A.; Tanvir, F.; Rashid, M.; Ullah, R.; Zubair, M.; Ali, S.; Anjum, K. M. Gold Nanoparticles Capped with L-Glycine, L-Cystine, and L-Tyrosine: Toxicity Profiling and Antioxidant Potential. *J. Mater. Sci.* **2023**, *58* (6), 2814–2837. https://doi.org/10.1007/s10853-023-08209-9.
(57) Peng, J.; Wang, L.; Wang, P.; Pei, Y. Density Functional Theory Computation and Machine Learning Studies of Interaction between Au_3 Clusters and 20 Natural Amino Acid Molecules. *ACS Omega* **2023**, *8* (25), 23024–23031. https://doi.org/10.1021/acsomega.3c02195.
(58) Mohammadpour, M.; Johnston, K. Investigation of Vibrational Changes Due to Adsorption of Glycine on Gold. *Comput. Theor. Chem.* **2023**, *1227*, 114224. https://doi.org/10.1016/j.comptc.2023.114224.
(59) Vesga, M. J.; McKechnie, D.; Laing, S.; Kearns, H.; Faulds, K.; Johnston, K.; Sefcik, J. Effect of Glycine on Aggregation of Citrate-Functionalised Gold Nanoparticles and SERS Measurements. *Colloids Surf. A*

Physicochem. Eng. Asp. **2021**, *621*, 126523. https://doi.org/10.1016/j.colsurfa.2021.126523.
(60) Hoefling, M.; Iori, F.; Corni, S.; Gottschalk, K.-E. Interaction of Amino Acids with the Au(111) Surface: Adsorption Free Energies from Molecular Dynamics Simulations. *Langmuir* **2010**, *26* (11), 8347–8351. https://doi.org/10.1021/la904765u.
(61) Buglak, A. A.; Kononov, A. I. Comparative Study of Gold and Silver Interactions with Amino Acids and Nucleobases. *RSC Adv.* **2020**, *10* (56), 34149–34160. https://doi.org/10.1039/D0RA06486F.
(62) Bashiri, G.; Padilla, M. S.; Swingle, K. L.; Shepherd, S. J.; Mitchell, M. J.; Wang, K. Nanoparticle Protein Corona: From Structure and Function to Therapeutic Targeting. *Lab Chip* **2023**, *23* (6), 1432–1466. https://doi.org/10.1039/D2LC00799A.
(63) Li, W.; Gao, T.; Lou, C.; Wang, H.; Liu, Y.; Cao, A. Biotinylated Au Nanoparticle-Based Artificial Antibody for Detection of Lysozyme by the Lateral Flow Immunoassay and Enzyme-Linked Immunosorbent Assay. *ACS Appl. Nano Mater.* **2022**, *5* (9), 12571–12581. https://doi.org/10.1021/acsanm.2c02268.
(64) Majdinasab, M.; Azziz, A.; Liu, Q.; Mora-Sanz, V.; Briz, N.; Edely, M.; Lamy de la Chapellea, M. Label-Free SERS for Rapid Identification of Interleukin 6 Based on Intrinsic SERS Fingerprint of Antibody-gold Nanoparticles Conjugate. *Int. J. Biol. Macromol.* **2023**, *253*, 127560. https://doi.org/10.1016/j.ijbiomac.2023.127560.
(65) Ghosh, S. K.; Nath, S.; Kundu, S.; Esumi, K.; Pal, T. Solvent and Ligand Effects on the Localized Surface Plasmon Resonance (LSPR) of Gold Colloids. *Journal of Physical Chemistry B* **2004**, *108* (37), 13963–13971. https://doi.org/10.1021/jp047021q.
(66) Xu, J. X.; Siriwardana, K.; Zhou, Y.; Zou, S.; Zhang, D. Quantification of Gold Nanoparticle Ultraviolet-Visible Extinction, Absorption, and Scattering Cross-Section Spectra and Scattering Depolarization Spectra: The Effects of Nanoparticle Geometry, Solvent Composition, Ligand Functionalization, and Nanoparticle Aggregation. *Anal. Chem.* **2018**, *90* (1), 785–793. https://doi.org/10.1021/acs.analchem.7b03227.
(67) Raghav, R.; Srivastava, S. Immobilization Strategy for Enhancing Sensitivity of Immunosensors: L-Asparagine-AuNPs as a Promising Alternative of EDC-NHS Activated Citrate-AuNPs for Antibody Immobilization. *Biosens. Bioelectron.* **2016**, *78*, 396–403. https://doi.org/10.1016/j.bios.2015.11.066.
(68) Liu, E. Y.; Jung, S.; Yi, H. Improved Protein Conjugation with Uniform, Macroporous Poly(Acrylamide-Co-Acrylic Acid) Hydrogel Microspheres via EDC/NHS Chemistry. *Langmuir* **2016**, *32* (42), 11043–11054. https://doi.org/10.1021/acs.langmuir.6b02591.
(69) Creyer, M. N.; Retout, M.; Jin, Z.; Yim, W.; Jokerst, J. V. Ligation of Gold Nanoparticles with Self-Assembling, Coiled-Coil Peptides. *J. Phys. Chem. B* **2023**, *127* (37), 8009–8018. https://doi.org/10.1021/acs.jpcb.3c02099.
(70) Gao, T.; Liu, Y.-Y.; Lou, C.; Wang, H.; Liu, Y.; Cao, A. PEGylation of Goldbody: PEG-Aided Conformational Engineering of Peptides on Gold Nanoparticles. *RSC Adv.* **2022**, *12* (40), 26123–26133. https://doi.org/10.1039/D2RA03903F.
(71) Du, M.; Zeng, F.; He, H.; Zhang, J.; Jiang, J.; Chen, G.; Wang, Q. Assembly and Function of Multidimensional Gold Nanostructures Based on Functional Protein Templates. *Adv. Funct. Mater.* **2025**. https://doi.org/10.1002/adfm.202503888.
(72) Liu, J.; Toy, R.; Vantucci, C.; Pradhan, P.; Zhang, Z.; Kuo, K. M.; Kubelick, K. P.; Huo, D.; Wen, J.; Kim, J.; Lyu, Z.; Dhal, S.; Atalis, A.; Ghosh-Choudhary, S. K.; Devereaux, E. J.; Gumbart, J. C.; Xia, Y.; Emelianov, S. Y.; Willett, N. J.; Roy, K. Bifunctional Janus Particles as Multivalent Synthetic Nanoparticle Antibodies (SNAbs) for Selective Depletion of Target Cells. *Nano Lett.* **2021**, *21* (1), 875–886. https://doi.org/10.1021/acs.nanolett.0c04833.
(73) Podlesnaia, E.; Stanca, S. E.; Çinçin, B.; Zieger, G.; Csáki, A.; Fritzsche, W. Customizable Ligand Exchange on the Surface of Gold Nanotriangles Enables Their Application in LSPR-Based Sensing. *Nanoscale Adv.* **2024**, *6* (21), 5430–5440. https://doi.org/10.1039/d4na00352g.
(74) Tu, M. H.; Sun, T.; Grattan, K. T. V. LSPR Optical Fibre Sensors Based on Hollow Gold Nanostructures. *Sens. Actuators B Chem.* **2014**, *191*, 37–44. https://doi.org/10.1016/j.snb.2013.09.094.
(75) Bhatia, P.; Verma, S. S. Enhancement of LSPR Properties of Temperature-Dependent Gold Nanoparticles. In *Materials Today: Proceedings*; Elsevier Ltd, 2022; Vol. 78, pp 871–876. https://doi.org/10.1016/j.matpr.2022.12.020.
(76) Yockell-Lelièvre, H.; Lussier, F.; Masson, J. F. Influence of the Particle Shape and Density of Self-Assembled Gold Nanoparticle Sensors on LSPR and SERS. *Journal of Physical Chemistry C* **2015**, *119* (51), 28577–28585. https://doi.org/10.1021/acs.jpcc.5b09570.
(77) Ran, C.; Zhang, J. lin; He, X.; Luo, C.; Zhang, Q.; Shen, Y.; Yin, L. Recent Development of Gold Nanochips in Biosensing and Biodiagnosis Sensibilization Strategies in Vitro Based on SPR, SERS and FRET Optical Properties. *Talanta*. Elsevier B.V. January 1, 2025.

https://doi.org/10.1016/j.talanta.2024.126936.
(78) Maity, S.; Ghosh, S.; Bhuyan, T.; Das, D.; Bandyopadhyay, D. Microfluidic Immunosensor for Point-of-Care-Testing of Beta-2-Microglobulin in Tear. *ACS Sustain. Chem. Eng.* **2020**, *8* (25), 9268–9276. https://doi.org/10.1021/acssuschemeng.0c00289.
(79) Okyem, S.; Awotunde, O.; Ogunlusi, T.; Riley, M. B.; Driskell, J. D. High-Affinity Points of Interaction on Antibody Allow Synthesis of Stable and Highly Functional Antibody-Gold Nanoparticle Conjugates. *Bioconjug. Chem.* **2021**, *32* (8), 1753–1762. https://doi.org/10.1021/acs.bioconjchem.1c00261.
(80) Marques da Silva Filho, J. A.; Costa Souza, A. B.; Carvalho de Mello, C.; D'Amato, D. L.; Ferreira de Carvalho Marques, F.; Martins Gouvêa, M.; Machado Ronconi, C. Linker-Controlled Stability in Gold Nanoparticles Enabling Plasmonic and Aggregation-Based Colorimetric Responses. *Dyes and Pigments* **2026**, *251*. https://doi.org/10.1016/j.dyepig.2026.113719.
(81) Su, H.; Li, S.; Kerman, K. Novel Thiolated-PEG Linker Molecule for Biosensor Development on Gold Surfaces. *Biosens. Bioelectron.* **2019**, *141*. https://doi.org/10.1016/j.bios.2019.111477.
(82) Chung, Y. H.; Lee, T.; Min, J.; Choi, J. W. Fabrication of Biomemory Device Composed of Myoglobin on DTSSP Layer. In *Molecular Crystals and Liquid Crystals*; 2010; Vol. 519, pp 19–26. https://doi.org/10.1080/15421400903579788.
(83) Seaberg, J.; Flynn, N.; Cai, A.; Ramsey, J. D. Effect of Redox-Responsive DTSSP Crosslinking on Poly(l-Lysine)-Grafted-Poly(Ethylene Glycol) Nanoparticles for Delivery of Proteins. *Biotechnol. Bioeng.* **2020**, *117* (8), 2504–2515. https://doi.org/10.1002/bit.27369.
(84) Xue, Y.; Li, X.; Li, H.; Zhang, W. Quantifying Thiol-Gold Interactions towards the Efficient Strength Control. *Nat. Commun.* **2014**, *5*. https://doi.org/10.1038/ncomms5348.
(85) Wang, W.; Wei, Q. Q.; Wang, J.; Wang, B. C.; Zhang, S. hui; Yuan, Z. Role of Thiol-Containing Polyethylene Glycol (Thiol-PEG) in the Modification Process of Gold Nanoparticles (AuNPs): Stabilizer or Coagulant? *J. Colloid Interface Sci.* **2013**, *404*, 223–229. https://doi.org/10.1016/j.jcis.2013.04.020.
(86) Ruiz, G.; Tripathi, K.; Okyem, S.; Driskell, J. D. PH Impacts the Orientation of Antibody Adsorbed onto Gold Nanoparticles. *Bioconjug. Chem.* **2019**, *30* (4), 1182–1191. https://doi.org/10.1021/acs.bioconjchem.9b00123.
(87) Tavanti, F.; Pedone, A.; Menziani, M. C. Competitive Binding of Proteins to Gold Nanoparticles Disclosed by Molecular Dynamics Simulations. *The Journal of Physical Chemistry C* **2015**, *119* (38), 22172–22180. https://doi.org/10.1021/acs.jpcc.5b05796.
(88) Choi, Y. K.; Kern, N. R.; Kim, S.; Kanhaiya, K.; Afshar, Y.; Jeon, S. H.; Jo, S.; Brooks, B. R.; Lee, J.; Tadmor, E. B.; Heinz, H.; Im, W. CHARMM-GUI Nanomaterial Modeler for Modeling and Simulation of Nanomaterial Systems. *J. Chem. Theory Comput.* **2022**, *18* (1). https://doi.org/10.1021/acs.jctc.1c00996.
(89) Duan, X.; Han, Y.; Zhu, B.; Gao, Y. Modelling of Metal Nanoparticles' Structures and Dynamics under Reaction Conditions. *Materials Today Catalysis* **2023**, *3*, 100032. https://doi.org/10.1016/j.mtcata.2023.100032.
(90) Brooks, C. L.; Case, D. A.; Plimpton, S.; Roux, B.; van der Spoel, D.; Tajkhorshid, E. Classical Molecular Dynamics. *J. Chem. Phys.* **2021**, *154* (10). https://doi.org/10.1063/5.0045455.
(91) Kariuki, R.; Penman, R.; Bryant, S. J.; Orrell-Trigg, R.; Meftahi, N.; Crawford, R. J.; McConville, C. F.; Bryant, G.; Voïtchovsky, K.; Conn, C. E.; Christofferson, A. J.; Elbourne, A. Behavior of Citrate-Capped Ultrasmall Gold Nanoparticles on a Supported Lipid Bilayer Interface at Atomic Resolution. *ACS Nano* **2022**, *16* (10), 17179–17196. https://doi.org/10.1021/acsnano.2c07751.
(92) Sun, S.; Zhang, X.; Cui, J.; Liang, S. Identification of the Miller Indices of a Crystallographic Plane: A Tutorial and a Comprehensive Review on Fundamental Theory, Universal Methods Based on Different Case Studies and Matters Needing Attention. *Nanoscale* **2020**, *12* (32), 16657–16677. https://doi.org/10.1039/D0NR03637D.
(93) Kaumbekova, S.; Sakaguchi, N.; Shah, D.; Umezawa, M. Effect of Gold Nanoparticles on the Conformation of Bovine Serum Albumin: Insights from CD Spectroscopic Analysis and Molecular Dynamics Simulations. *ACS Omega* **2024**, *9* (50), 49283–49292. https://doi.org/10.1021/acsomega.4c06409.
(94) Baruah, K.; Singh, A. K.; Kumari, K.; Nongbri, D. L.; Jha, A. N.; Singha Roy, A. Interactions of Turmeric- and Curcumin-Functionalized Gold Nanoparticles with Human Serum Albumin: Exploration of Protein Corona Formation, Binding, Thermodynamics, and Antifibrillation Studies. *Langmuir* **2024**, *40* (2), 1381–1398. https://doi.org/10.1021/acs.langmuir.3c03032.
(95) Zeni, C.; Rossi, K.; Glielmo, A.; Baletto, F. On Machine Learning Force Fields for Metallic Nanoparticles. *Adv. Phys. X* **2019**, *4* (1), 1654919. https://doi.org/10.1080/23746149.2019.1654919.
(96) Zeni, C.; Rossi, K.; Pavloudis, T.; Kioseoglou, J.; de Gironcoli, S.; Palmer, R. E.; Baletto, F. Data-Driven Simulation and Characterisation of Gold Nanoparticle Melting. *Nat. Commun.* **2021**, *12* (1), 6056. https://doi.org/10.1038/s41467-021-26199-7.

(97) Li, Z.; Ruiz, V. G.; Kanduč, M.; Dzubiella, J. Highly Heterogeneous Polarization and Solvation of Gold Nanoparticles in Aqueous Electrolytes. *ACS Nano* **2021**, *15* (8), 13155–13165. https://doi.org/10.1021/acsnano.1c02668.
(98) Barmparis, G. D.; Lodziana, Z.; Lopez, N.; Remediakis, I. N. Nanoparticle Shapes by Using Wulff Constructions and First-Principles Calculations. *Beilstein Journal of Nanotechnology* **2015**, *6*, 361–368. https://doi.org/10.3762/bjnano.6.35.
(99) Islam, Md. A.; Rahman, S. M. M.; Mim, J. J.; Khan, S.; Khan, F.; Patwary, Md. A. I.; Hossain, N. Applications of Molecular Dynamics in Nanomaterial Design and Characterization - A Review. *Chemical Engineering Journal Advances* **2025**, *22*, 100731. https://doi.org/10.1016/j.ceja.2025.100731.
(100) Son, G.; Li, Y.; Shneidman, A. V.; Han, J. H.; Aizenberg, M.; Sautet, P.; Aizenberg, J. Facet-Dependence of Electron Storage in Gold-Decorated Titania Nanocrystals. *Chemistry of Materials* **2023**, *35* (22), 9505–9516. https://doi.org/10.1021/acs.chemmater.3c01252.
(101) Qin, Y.; Pan, W.; Yu, D.; Lu, Y.; Wu, W.; Zhou, J. Stepwise Evolution of Au Micro/Nanocrystals from an Octahedron into a Truncated Ditetragonal Prism. *Chemical Communications* **2018**, *54* (27), 3411–3414. https://doi.org/10.1039/C8CC00973B.
(102) Kim, K.; Kim, M.-I.; Chung, J.; Ahn, J.-H.; Rhee, S. Crystal Structure of Metal-Dependent Allantoinase from Escherichia Coli. *J. Mol. Biol.* **2009**, *387* (5), 1067–1074. https://doi.org/10.1016/j.jmb.2009.02.041.
(103) Gruber, J.; Tang, S. Y.; Jenner, A. M.; Mudway, I.; Blomberg, A.; Behndig, A.; Kasiman, K.; Lee, C.-Y. J.; Seet, R. C. S.; Zhang, W.; Chen, C.; Kelly, F. J.; Halliwell, B. Allantoin in Human Plasma, Serum, and Nasal-Lining Fluids as a Biomarker of Oxidative Stress: Avoiding Artifacts and Establishing Real *in Vivo* Concentrations. *Antioxid. Redox Signal.* **2009**, *11* (8), 1767–1776. https://doi.org/10.1089/ars.2008.2364.
(104) Marchetti, M.; Ronda, L.; Faggiano, S.; Liuzzi, A.; Percudani, R.; Bettati, S. Fluorescence Quantification of Allantoin in Biological Samples by Cap-Immobilized Allantoinase/Resorcinol Assay. *Sens. Actuators B Chem.* **2018**, *255*, 2820–2828. https://doi.org/10.1016/j.snb.2017.09.099.
(105) Pavitt, D. V; de Fonseka, S.; Al-Khalaf, N.; Cam, J. M.; Reaveley, D. A. Assay of Serum Allantoin in Humans by Gas Chromatography–Mass Spectrometry. *Clinica Chimica Acta* **2002**, *318* (1–2), 63–70. https://doi.org/10.1016/S0009-8981(01)00805-1.
(106) Kozlik, P.; Hasikova, L.; Stiburkova, B.; Zavada, J.; Kalikova, K. Rapid and Reliable HILIC-MS/MS Method for Monitoring Allantoin as a Biomarker of Oxidative Stress. *Anal. Biochem.* **2020**, *589*, 113509. https://doi.org/10.1016/j.ab.2019.113509.
(107) Andries, A.; De Rechter, S.; Janssens, P.; Mekahli, D.; Van Schepdael, A. Simultaneous Determination of Allantoin and Adenosine in Human Urine Using Liquid Chromatography – UV Detection. *Journal of Chromatography B* **2018**, *1096*, 201–207. https://doi.org/10.1016/j.jchromb.2018.08.026.
(108) Tolun, A. A.; Zhang, H.; Il'yasova, D.; Sztáray, J.; Young, S. P.; Millington, D. S. Allantoin in Human Urine Quantified by Ultra-Performance Liquid Chromatography–Tandem Mass Spectrometry. *Anal. Biochem.* **2010**, *402* (2), 191–193. https://doi.org/10.1016/j.ab.2010.03.033.
(109) Il'yasova, D.; Scarbrough, P.; Spasojevic, I. Urinary Biomarkers of Oxidative Status. *Clinica Chimica Acta* **2012**, *413* (19–20), 1446–1453. https://doi.org/10.1016/j.cca.2012.06.012.
(110) Marchetti, M.; Ronda, L.; Percudani, R.; Bettati, S. Immobilization of Allantoinase for the Development of an Optical Biosensor of Oxidative Stress States. *Sensors* **2019**, *20* (1), 196. https://doi.org/10.3390/s20010196.
(111) Turner, R.; Stamp, L. K.; Kettle, A. J. Detection of Allantoin in Clinical Samples Using Hydrophilic Liquid Chromatography with Stable Isotope Dilution Negative Ion Tandem Mass Spectrometry. *Journal of Chromatography B* **2012**, *891–892*, 85–89. https://doi.org/10.1016/j.jchromb.2012.02.009.
(112) Kand'ár, R.; Žáková, P. Allantoin as a Marker of Oxidative Stress in Human Erythrocytes. *Clin. Chem. Lab. Med.* **2008**, *46* (9). https://doi.org/10.1515/CCLM.2008.244.
(113) Mulrooney, S. B.; Hausinger, R. P. Metal Ion Dependence of Recombinant *Escherichia Coli* Allantoinase. *J. Bacteriol.* **2003**, *185* (1), 126–134. https://doi.org/10.1128/JB.185.1.126-134.2003.
(114) Ho, Y.-Y.; Hsieh, H.-C.; Huang, C.-Y. Biochemical Characterization of Allantoinase from Escherichia Coli BL21. *Protein J.* **2011**, *30* (6), 384–394. https://doi.org/10.1007/s10930-011-9343-z.
(115) Martínez-Gómez, A. I.; Soriano-Maldonado, P.; Andújar-Sánchez, M.; Clemente-Jiménez, J. M.; Rodríguez-Vico, F.; Neira, J. L.; Las Heras-Vázquez, F. J.; Martínez-Rodríguez, S. Biochemical and Mutational Studies of Allantoinase from Bacillus Licheniformis CECT 20T. *Biochimie* **2014**, *99*, 178–188. https://doi.org/10.1016/j.biochi.2013.12.002.
(116) Ramazzina, I.; Cendron, L.; Folli, C.; Berni, R.; Monteverdi, D.; Zanotti, G.; Percudani, R. Logical Identification of an Allantoinase Analog (PuuE) Recruited from Polysaccharide Deacetylases. *Journal of Biological Chemistry* **2008**, *283* (34), 23295–23304. https://doi.org/10.1074/jbc.M801195200.
(117) McGinnis, S.; Madden, T. L. BLAST: At the Core of a Powerful and Diverse Set of Sequence Analysis Tools. *Nucleic Acids Res.* **2004**, *32* (Web Server), W20–W25. https://doi.org/10.1093/nar/gkh435.

(118) Varadi, M.; Anyango, S.; Deshpande, M.; Nair, S.; Natassia, C.; Yordanova, G.; Yuan, D.; Stroe, O.; Wood, G.; Laydon, A.; Žídek, A.; Green, T.; Tunyasuvunakool, K.; Petersen, S.; Jumper, J.; Clancy, E.; Green, R.; Vora, A.; Lutfi, M.; Figurnov, M.; Cowie, A.; Hobbs, N.; Kohli, P.; Kleywegt, G.; Birney, E.; Hassabis, D.; Velankar, S. AlphaFold Protein Structure Database: Massively Expanding the Structural Coverage of Protein-Sequence Space with High-Accuracy Models. *Nucleic Acids Res.* **2022**, *50* (D1), D439–D444. https://doi.org/10.1093/nar/gkab1061.
(119) Tamura, K.; Stecher, G.; Kumar, S. MEGA11: Molecular Evolutionary Genetics Analysis Version 11. *Mol. Biol. Evol.* **2021**, *38* (7). https://doi.org/10.1093/molbev/msab120.
(120) Edgar, R. C. MUSCLE: Multiple Sequence Alignment with High Accuracy and High Throughput. *Nucleic Acids Res.* **2004**, *32* (5), 1792–1797. https://doi.org/10.1093/nar/gkh340.
(121) Letunic, I.; Bork, P. Interactive Tree of Life (ITOL) v5: An Online Tool for Phylogenetic Tree Display and Annotation. *Nucleic Acids Res.* **2021**, *49* (W1). https://doi.org/10.1093/nar/gkab301.
(122) Gasteiger, E.; Hoogland, C.; Gattiker, A.; Duvaud, S.; Wilkins, M. R.; Appel, R. D.; Bairoch, A. Protein Identification and Analysis Tools on the ExPASy Server. In *The Proteomics Protocols Handbook*; Humana Press: Totowa, NJ, 2005; pp 571–607. https://doi.org/10.1385/1-59259-890-0:571.
(123) Kozlowski, L. P. IPC – Isoelectric Point Calculator. *Biol. Direct* **2016**, *11* (1), 55. https://doi.org/10.1186/s13062-016-0159-9.
(124) Hon, J.; Marusiak, M.; Martinek, T.; Kunka, A.; Zendulka, J.; Bednar, D.; Damborsky, J. SoluProt: Prediction of Soluble Protein Expression in *Escherichia Coli*. *Bioinformatics* **2021**, *37* (1), 23–28. https://doi.org/10.1093/bioinformatics/btaa1102.
(125) Hall, T. A. BioEdit: A User-Friendly Biological Sequence Alignment Editor and Analysis Program for Windows 95/98/NT. . In *Nucleic Acids Symposium Series*; 1999; pp 95–98.
(126) Seeliger, D.; de Groot, B. L. Ligand Docking and Binding Site Analysis with PyMOL and Autodock/Vina. *J. Comput. Aided. Mol. Des.* **2010**, *24* (5), 417–422. https://doi.org/10.1007/s10822-010-9352-6.
(127) Papadopoulos, J. S.; Agarwala, R. COBALT: Constraint-Based Alignment Tool for Multiple Protein Sequences. *Bioinformatics* **2007**, *23* (9), 1073–1079. https://doi.org/10.1093/bioinformatics/btm076.
(128) Crooks, G. E.; Hon, G.; Chandonia, J.-M.; Brenner, S. E. WebLogo: A Sequence Logo Generator: Figure 1. *Genome Res.* **2004**, *14* (6), 1188–1190. https://doi.org/10.1101/gr.849004.
(129) Ishida, T.; Kinoshita, K. PrDOS: Prediction of Disordered Protein Regions from Amino Acid Sequence. *Nucleic Acids Res.* **2007**, *35* (Web Server), W460–W464. https://doi.org/10.1093/nar/gkm363.
(130) Guruprasad, K.; Reddy, B. V. B.; Pandit, M. W. Correlation between Stability of a Protein and Its Dipeptide Composition: A Novel Approach for Predicting *in Vivo* Stability of a Protein from Its Primary Sequence. *"Protein Engineering, Design and Selection"* **1990**, *4* (2), 155–161. https://doi.org/10.1093/protein/4.2.155.
(131) Gill, S. C.; von Hippel, P. H. Calculation of Protein Extinction Coefficients from Amino Acid Sequence Data. *Anal. Biochem.* **1989**, *182* (2), 319–326. https://doi.org/10.1016/0003-2697(89)90602-7.
(132) Chen, C. R.; Makhatadze, G. I. ProteinVolume: Calculating Molecular van Der Waals and Void Volumes in Proteins. *BMC Bioinformatics* **2015**, *16* (1), 101. https://doi.org/10.1186/s12859-015-0531-2.
(133) Magyar, C.; Gromiha, M. M.; Pujadas, G.; Tusnady, G. E.; Simon, I. SRide: A Server for Identifying Stabilizing Residues in Proteins. *Nucleic Acids Res.* **2005**, *33* (Web Server), W303–W305. https://doi.org/10.1093/nar/gki409.
(134) Gromiha, M. M.; Pujadas, G.; Magyar, C.; Selvaraj, S.; Simon, I. Locating the Stabilizing Residues in $(\alpha/\beta)_8$ Barrel Proteins Based on Hydrophobicity, Long-range Interactions, and Sequence Conservation. *Proteins: Structure, Function, and Bioinformatics* **2004**, *55* (2), 316–329. https://doi.org/10.1002/prot.20052.
(135) Fleming, P. J.; Fleming, K. G. HullRad: Fast Calculations of Folded and Disordered Protein and Nucleic Acid Hydrodynamic Properties. *Biophys. J.* **2018**, *114* (4), 856–869. https://doi.org/10.1016/j.bpj.2018.01.002.
(136) Chepkwony, N. K.; Brun, Y. V. A Polysaccharide Deacetylase Enhances Bacterial Adhesion in High-Ionic-Strength Environments. *iScience* **2021**, *24* (9), 103071. https://doi.org/10.1016/j.isci.2021.103071.
(137) Rosano, G. L.; Ceccarelli, E. A. Recombinant Protein Expression in Escherichia Coli: Advances and Challenges. *Frontiers in Microbiology*. 2014. https://doi.org/10.3389/fmicb.2014.00172.
(138) Shirai, A.; Matsuyama, A.; Yashiroda, Y.; Hashimoto, A.; Kawamura, Y.; Arai, R.; Komatsu, Y.; Horinouchi, S.; Yoshida, M. Global Analysis of Gel Mobility of Proteins and Its Use in Target Identification. *Journal of Biological Chemistry* **2008**, *283* (16), 10745–10752. https://doi.org/10.1074/jbc.M709211200.
(139) Vasina, M.; Velecký, J.; Planas-Iglesias, J.; Marques, S. M.; Skarupova, J.; Damborsky, J.; Bednar, D.; Mazurenko, S.; Prokop, Z. Tools for Computational Design and High-Throughput Screening of Therapeutic Enzymes. *Adv. Drug Deliv. Rev.* **2022**, *183*, 114143. https://doi.org/10.1016/j.addr.2022.114143.

(140) Thomsen, M. C. F.; Nielsen, M. Seq2Logo: A Method for Construction and Visualization of Amino Acid Binding Motifs and Sequence Profiles Including Sequence Weighting, Pseudo Counts and Two-Sided Representation of Amino Acid Enrichment and Depletion. *Nucleic Acids Res.* **2012**, *40* (W1), W281–W287. https://doi.org/10.1093/nar/gks469.
(141) Yan, B. X.; Sun, Y. Q. Glycine Residues Provide Flexibility for Enzyme Active Sites. *Journal of Biological Chemistry* **1997**, *272* (6), 3190–3194. https://doi.org/10.1074/jbc.272.6.3190.
(142) Nallamsetty, S.; Waugh, D. S. A Generic Protocol for the Expression and Purification of Recombinant Proteins in Escherichia Coli Using a Combinatorial His6-Maltose Binding Protein Fusion Tag. *Nat. Protoc.* **2007**, *2* (2), 383–391. https://doi.org/10.1038/nprot.2007.50.
(143) Moerz, S. T.; Huber, P. Protein Adsorption into Mesopores: A Combination of Electrostatic Interaction, Counterion Release, and van Der Waals Forces. *Langmuir* **2014**, *30* (10), 2729–2737. https://doi.org/10.1021/la404947j.
(144) Marsh, J. A. Buried and Accessible Surface Area Control Intrinsic Protein Flexibility. *J. Mol. Biol.* **2013**, *425* (17), 3250–3263. https://doi.org/10.1016/j.jmb.2013.06.019.
(145) Cao, A. The Last Secret of Protein Folding: The Real Relationship Between Long-Range Interactions and Local Structures. *Protein J.* **2020**, *39* (5), 422–433. https://doi.org/10.1007/s10930-020-09925-w.
(146) Gromiha, M. M.; Selvaraj, S. Comparison between Long-Range Interactions and Contact Order in Determining the Folding Rate of Two-State Proteins: Application of Long-Range Order to Folding Rate Prediction. *J. Mol. Biol.* **2001**, *310* (1). https://doi.org/10.1006/jmbi.2001.4775.
(147) Lobanov, M. Yu.; Bogatyreva, N. S.; Galzitskaya, O. V. Radius of Gyration as an Indicator of Protein Structure Compactness. *Mol. Biol.* **2008**, *42* (4), 623–628. https://doi.org/10.1134/S0026893308040195.
(148) Zuev, Y. F.; Kusova, A. M.; Sitnitsky, A. E. Protein Translational Diffusion as a Way to Detect Intermolecular Interactions. *Biophys. Rev.* **2023**, *15* (5), 1111–1125. https://doi.org/10.1007/s12551-023-01108-y.
(149) Zheng, T.; Cherubin, P.; Cilenti, L.; Teter, K.; Huo, Q. A Simple and Fast Method to Study the Hydrodynamic Size Difference of Protein Disulfide Isomerase in Oxidized and Reduced Form Using Gold Nanoparticles and Dynamic Light Scattering. *Analyst* **2016**, *141* (3), 934–938. https://doi.org/10.1039/C5AN02248G.
(150) Lee, P. Y.; Costumbrado, J.; Hsu, C.-Y.; Kim, Y. H. Agarose Gel Electrophoresis for the Separation of DNA Fragments. *Journal of Visualized Experiments* **2012**, No. 62. https://doi.org/10.3791/3923.
(151) Stellwagen, N. C. Electrophoresis of DNA in Agarose Gels, Polyacrylamide Gels and in Free Solution. *Electrophoresis* **2009**, *30* (S1). https://doi.org/10.1002/elps.200900052.
(152) Ghebremedhin, M.; Seiffert, S.; Vilgis, T. A. Physics of Agarose Fluid Gels: Rheological Properties and Microstructure. *Curr. Res. Food Sci.* **2021**, *4*, 436–448. https://doi.org/10.1016/j.crfs.2021.06.003.
(153) Cheng, S.; Wang, P.; Tao, C.; Zhang, D.; Li, Z.; Yamaguchi, Y. The Effect of Electrophoretic Parameters on Separation Performance of Short DNA Fragments. *Anal. Biochem.* **2018**, *556*, 99–103. https://doi.org/10.1016/j.ab.2018.06.031.
(154) Brody, J. R.; Calhoun, E. S.; Gallmeier, E.; Creavalle, T. D.; Kern, S. E. Ultra-Fast High-Resolution Agarose Electrophoresis of DNA and RNA Using Low-Molarity Conductive Media. *Biotechniques* **2004**, *37* (4), 598–602. https://doi.org/10.2144/04374ST04.
(155) Semenov, K.; Taraskin, A.; Yurchenko, A.; Baranovskaya, I.; Purvinsh, L.; Gyulikhandanova, N.; Vasin, A. Uncertainty Estimation for Quantitative Agarose Gel Electrophoresis of Nucleic Acids. *Sensors* **2023**, *23* (4), 1999. https://doi.org/10.3390/s23041999.
(156) Descallar, F. B. A.; Matsukawa, S. Change of Network Structure in Agarose Gels by Aging during Storage Studied by NMR and Electrophoresis. *Carbohydr. Polym.* **2020**, *245*, 116497. https://doi.org/10.1016/j.carbpol.2020.116497.
(157) Schindelin, J.; Rueden, C. T.; Hiner, M. C.; Eliceiri, K. W. The ImageJ Ecosystem: An Open Platform for Biomedical Image Analysis. *Mol. Reprod. Dev.* **2015**, *82* (7–8), 518–529. https://doi.org/10.1002/mrd.22489.
(158) Ziraldo, R.; Shoura, M. J.; Fire, A. Z.; Levene, S. D. Deconvolution of Nucleic-Acid Length Distributions: A Gel Electrophoresis Analysis Tool and Applications. *Nucleic Acids Res.* **2019**, *47* (16), e92–e92. https://doi.org/10.1093/nar/gkz534.
(159) Jonkman, J.; Brown, C. M.; Wright, G. D.; Anderson, K. I.; North, A. J. Guidance for Quantitative Confocal Microscopy. *Nat. Protoc.* **2020**. https://doi.org/10.1038/s41596-020-0307-7.
(160) Morrison, L. E.; Lefever, M. R.; Behman, L. J.; Leibold, T.; Roberts, E. A.; Horchner, U. B.; Bauer, D. R. Brightfield Multiplex Immunohistochemistry with Multispectral Imaging. *Laboratory Investigation* **2020**, *100* (8). https://doi.org/10.1038/s41374-020-0429-0.
(161) Gozzi, G.; Tobias, C.; Hülagü, D.; Rurack, K.; Hodoroaba, V.-D. Toward Determination of the Surface Roughness of Particles from a SEM Image. *Microscopy and Microanalysis* **2021**, *27* (S1).

https://doi.org/10.1017/s1431927621011375.
(162) Schneider, C. A.; Rasband, W. S.; Eliceiri, K. W. NIH Image to ImageJ: 25 Years of Image Analysis. *Nature Methods*. 2012. https://doi.org/10.1038/nmeth.2089.
(163) Gallagher, S. R. Digital Image Processing and Analysis with Imagej. *Current Protocols in Essential Laboratory Techniques* **2014**, *2014*. https://doi.org/10.1002/9780470089941.eta03cs9.
(164) Dobson, E. T. A.; Cimini, B.; Klemm, A. H.; Wählby, C.; Carpenter, A. E.; Eliceiri, K. W. ImageJ and CellProfiler: Complements in Open-Source Bioimage Analysis. *Curr. Protoc.* **2021**, *1* (5). https://doi.org/10.1002/cpz1.89.
(165) Fernandes, G. M.; Silva, W. R.; Barreto, D. N.; Lamarca, R. S.; Lima Gomes, P. C. F.; Flávio da S Petruci, J.; Batista, A. D. Novel Approaches for Colorimetric Measurements in Analytical Chemistry – A Review. *Analytica Chimica Acta*. 2020. https://doi.org/10.1016/j.aca.2020.07.030.
(166) Deb, A.; Gogoi, P.; Singh, S. K.; Gooh Pattader, P. S. Noise-Activated Fast Locomotion of DNA through the Frictional Landscape of Nanoporous Gels. *Langmuir* **2022**, *38* (38). https://doi.org/10.1021/acs.langmuir.2c01897.
(167) Duncan, B.; Kim, C.; Rotello, V. M. Gold Nanoparticle Platforms as Drug and Biomacromolecule Delivery Systems. *Journal of Controlled Release* **2010**, *148* (1), 122–127. https://doi.org/10.1016/j.jconrel.2010.06.004.
(168) Anik, M. I.; Mahmud, N.; Al Masud, A.; Hasan, M. Gold Nanoparticles (GNPs) in Biomedical and Clinical Applications: A Review. *Nano Select* **2022**, *3* (4), 792–828. https://doi.org/10.1002/nano.202100255.
(169) Obalola, A. A.; Abrahamse, H.; Dhilip Kumar, S. S. Recent Advances in Gold Nanoparticle-Based Targeted Photodynamic and Photothermal Cancer Therapy. *Nanoscale Adv.* **2025**, *7* (23), 7440–7458. https://doi.org/10.1039/D5NA00767D.
(170) Singh, P.; Joshi, A. S.; Singh, H.; Mijakovic, I. Medical Importance and Pharmacokinetics of Gold Nanoparticles in the Human Body. *Mol. Cancer* **2025**, *24* (1), 252. https://doi.org/10.1186/s12943-025-02418-3.
(171) Sati, A.; Mali, S. N.; Samdani, N.; Annadurai, S.; Dongre, R.; Satpute, N.; Ranade, T. N.; Pratap, A. P. From Past to Present: Gold Nanoparticles (AuNPs) in Daily Life─Synthesis Mechanisms, Influencing Factors, Characterization, Toxicity, and Emerging Applications in Biomedicine, Nanoelectronics, and Materials Science. *ACS Omega* **2025**, *10* (31), 33999–34087. https://doi.org/10.1021/acsomega.5c03162.
(172) Ghosh, S. K.; Pal, T. Interparticle Coupling Effect on the Surface Plasmon Resonance of Gold Nanoparticles: From Theory to Applications. *Chem. Rev.* **2007**, *107* (11), 4797–4862. https://doi.org/10.1021/cr0680282.
(173) Quero-Delgado, M.; Codina, H.; Gómez, R.; Terán, F. J.; Muñoz-Fernández, M. A.; Jiménez, J. L.; Resino, S.; Sepúlveda-Crespo, D.; Martínez, I. Advances in Nanotechnology-Enabled Optical Biosensors for Dengue Virus Detection: A Systematic Review. *Med. Res. Rev.* **2026**, *46* (1), 70–111. https://doi.org/10.1002/med.70006.
(174) Jazayeri, M. H.; Amani, H.; Pourfatollah, A. A.; Pazoki-Toroudi, H.; Sedighimoghaddam, B. Various Methods of Gold Nanoparticles (GNPs) Conjugation to Antibodies. *Sens. Biosensing Res.* **2016**, *9*, 17–22. https://doi.org/10.1016/j.sbsr.2016.04.002.
(175) Bailly, A.-L.; Correard, F.; Popov, A.; Tselikov, G.; Chaspoul, F.; Appay, R.; Al-Kattan, A.; Kabashin, A. V.; Braguer, D.; Esteve, M.-A. In Vivo Evaluation of Safety, Biodistribution and Pharmacokinetics of Laser-Synthesized Gold Nanoparticles. *Sci. Rep.* **2019**, *9* (1), 12890. https://doi.org/10.1038/s41598-019-48748-3.
(176) Chung, Y.-H.; Lee, T.; Min, J.; Choi, J.-W. Fabrication of Biomemory Device Composed of Myoglobin on DTSSP Layer. *Molecular Crystals and Liquid Crystals* **2010**, *519* (1), 19–26. https://doi.org/10.1080/15421400903579788.
(177) Ohtsubo, K.; Takamatsu, S.; Gao, C.; Korekane, H.; Kurosawa, T. M.; Taniguchi, N. N-Glycosylation Modulates the Membrane Sub-Domain Distribution and Activity of Glucose Transporter 2 in Pancreatic Beta Cells. *Biochem. Biophys. Res. Commun.* **2013**, *434* (2), 346–351. https://doi.org/10.1016/j.bbrc.2013.03.076.
(178) Oliverio, M.; Perotto, S.; Messina, G. C.; Lovato, L.; De Angelis, F. Chemical Functionalization of Plasmonic Surface Biosensors: A Tutorial Review on Issues, Strategies, and Costs. *ACS Appl. Mater. Interfaces* **2017**, *9* (35), 29394–29411. https://doi.org/10.1021/acsami.7b01583.
(179) Maity, S.; Ghosh, S.; Bhuyan, T.; Das, D.; Bandyopadhyay, D. Microfluidic Immunosensor for Point-of-Care-Testing of Beta-2-Microglobulin in Tear. *ACS Sustain. Chem. Eng.* **2020**, *8* (25), 9268–9276. https://doi.org/10.1021/acssuschemeng.0c00289.
(180) Ngo, L.; Zhang, W.; Hnit, S. S. T.; Wang, Y. Improving SERS Biosensors for the Analysis of Ovarian Cancer-Derived Small Extracellular Vesicles. *Analyst* **2023**, *148* (13), 3074–3086. https://doi.org/10.1039/D3AN00398A.

(181) Cordina, N. M.; Zhang, W.; Packer, N. H.; Wang, Y. Rapid and Sensitive Glycan Targeting by Lectin-SERS Assay. *Mol. Omics* **2020**, *16* (4), 339–344. https://doi.org/10.1039/C9MO00181F.
(182) Silva, P. B. da; Silva, J. R. da; Rodrigues, M. C.; Vieira, J. A.; Andrade, I. A. de; Nagata, T.; Santos, A. S.; Silva, S. W. da; Rocha, M. C. O. da; Báo, S. N.; Moraes-Vieira, P. M.; Proença-Modena, J.; Angelim, M. K. C.; de Souza, G. F.; Muraro, S. P.; de Barros, A. L. B.; de Souza Martins, G. A.; Ribeiro-Dias, F.; Machado, G.; Fessel, M. R.; Chudzinski-Tavassi, A. M.; Ronconi, C. M.; Gonçalves, D.; Curi, R.; Oliveira, O. N.; Azevedo, R. B. Detection of SARS-CoV-2 Virus via Dynamic Light Scattering Using Antibody-Gold Nanoparticle Bioconjugates against Viral Spike Protein. *Talanta* **2022**, *243*, 123355. https://doi.org/10.1016/j.talanta.2022.123355.
(183) D'Amato, D. L.; Bessa, I. A. A.; Souza, A. B. C.; Mendes-Monteiro, L.; Mohana-Borges, R.; Allonso, D.; Ligiero, C. B. P.; Ronconi, C. M. Zika Virus NS1 Protein Detection Using Gold Nanoparticle-Assisted Dynamic Light Scattering. *Chem. Asian J.* **2024**, *19* (23). https://doi.org/10.1002/asia.202400826.
(184) Ayankojo, A. G.; Boroznjak, R.; Reut, J.; Öpik, A.; Syritski, V. Molecularly Imprinted Polymer Based Electrochemical Sensor for Quantitative Detection of SARS-CoV-2 Spike Protein. *Sens. Actuators B Chem.* **2022**, *353*, 131160. https://doi.org/10.1016/j.snb.2021.131160.
(185) Chavan, S. G.; Yagati, A. K.; Kim, H. T.; Jin, E.; Park, S. R.; Patil, D. V.; Lee, M.-H. Dimeric-Serotonin Bivalent Ligands Induced Gold Nanoparticle Aggregation for Highly Sensitive and Selective Serotonin Biosensor. *Biosens. Bioelectron.* **2021**, *191*, 113447. https://doi.org/10.1016/j.bios.2021.113447.
(186) Yazdani, S.; Daneshkhah, A.; Diwate, A.; Patel, H.; Smith, J.; Reul, O.; Cheng, R.; Izadian, A.; Hajrasouliha, A. R. Model for Gold Nanoparticle Synthesis: Effect of PH and Reaction Time. *ACS Omega* **2021**, *6* (26), 16847–16853. https://doi.org/10.1021/acsomega.1c01418.
(187) El Jery, A.; Alawamleh, H. S. K.; Sami, M. H.; Abbas, H. A.; Sammen, S. Sh.; Ahsan, A.; Imteaz, M. A.; Shanableh, A.; Shafiquzzaman, Md.; Osman, H.; Al-Ansari, N. Isotherms, Kinetics and Thermodynamic Mechanism of Methylene Blue Dye Adsorption on Synthesized Activated Carbon. *Sci. Rep.* **2024**, *14* (1), 970. https://doi.org/10.1038/s41598-023-50937-0.
(188) Rosli, M. A.; Daud, Z.; Ridzuan, M. B.; Aziz, N. A. A.; Awang, H. B.; Adeleke, A. O.; Hossain, K.; Ismail, N. Equilibrium Isotherm and Kinetic Study of the Adsorption of Organic Pollutants of Leachate by Using Micro Peat-Activated Carbon Composite Media. *Desalination Water Treat.* **2019**, *160*, 185–192. https://doi.org/10.5004/dwt.2019.24247.
(189) Wang, J.; Guo, X. Adsorption Isotherm Models: Classification, Physical Meaning, Application and Solving Method. *Chemosphere* **2020**, *258*, 127279. https://doi.org/10.1016/j.chemosphere.2020.127279.
(190) Syed, B.; Prasad, NagendraM. N.; Satisha, S. Endogenic Mediated Synthesis of Gold Nanoparticles Bearing Bactericidal Activity. *J. Microsc. Ultrastruct.* **2016**, *4* (3), 162. https://doi.org/10.1016/j.jmau.2016.01.004.
(191) Filbrun, S. L.; Driskell, J. D. A Fluorescence-Based Method to Directly Quantify Antibodies Immobilized on Gold Nanoparticles. *Analyst* **2016**, *141* (12), 3851–3857. https://doi.org/10.1039/C6AN00193A.
(192) Shipway, A. N.; Lahav, M.; Gabai, R.; Willner, I. Investigations into the Electrostatically Induced Aggregation of Au Nanoparticles. *Langmuir* **2000**, *16* (23), 8789–8795. https://doi.org/10.1021/la000316k.
(193) Chornokur, G.; Arya, S. K.; Phelan, C.; Tanner, R.; Bhansali, S. Impedance-Based Miniaturized Biosensor for Ultrasensitive and Fast Prostate-Specific Antigen Detection. *J. Sens.* **2011**, *2011*, 1–7. https://doi.org/10.1155/2011/983752.
(194) Shahub, S.; Lin, K.-C.; Muthukumar, S.; Prasad, S. A Proof-of-Concept Electrochemical Skin Sensor for Simultaneous Measurement of Glial Fibrillary Acidic Protein (GFAP) and Interleukin-6 (IL-6) for Management of Traumatic Brain Injuries. *Biosensors (Basel).* **2022**, *12* (12), 1095. https://doi.org/10.3390/bios12121095.
(195) Chen, Y.-F.; Chang, C.-H.; Lin, C.-Y.; Lin, L.-F.; Yeh, M.-L.; Jan, J.-S. Disulfide-Cross-Linked PEG-Block-Polypeptide Nanoparticles with High Drug Loading Content as Glutathione-Triggered Anticancer Drug Nanocarriers. *Colloids Surf. B Biointerfaces* **2018**, *165*, 172–181. https://doi.org/10.1016/j.colsurfb.2018.02.042.
(196) Madiyar, F.; Ghate, S.; Nielsen, K.; Govindarajan, R. S.; Kim, D.; Stark, T. Light-Enhanced Micropyramidal Sensors for Interleukin-6 Impedance Detection. In *2024 IEEE Aerospace Conference*; IEEE, 2024; pp 1–8. https://doi.org/10.1109/AERO58975.2024.10521023.
(197) Poudyal, D. C.; Dhamu, V. N.; Samson, M.; Muthukumar, S.; Prasad, S. Portable Pesticide Electrochem-Sensor: A Label-Free Detection of Glyphosate in Human Urine. *Langmuir* **2022**, *38* (5), 1781–1790. https://doi.org/10.1021/acs.langmuir.1c02877.
(198) Wei, W.-J.; Gao, H.-Q.; Fang, M.; Tang, Y.-Z.; Wei, Y. Revealing the Order–Disorder Type Phase Transition Mechanism in Two New Supramolecular Clathrates. *CrystEngComm* **2023**, *25* (9), 1333–1338. https://doi.org/10.1039/D2CE01419J.
(199) Cetin, A.; Ilk Capar, M. Functional-Group Effect of Ligand Molecules on the Aggregation of Gold

Nanoparticles: A Molecular Dynamics Simulation Study. *J. Phys. Chem. B* **2022**, *126* (29), 5534–5543. https://doi.org/10.1021/acs.jpcb.2c01132.
(200) Coelho, E.; de Andrade, D. X.; de Almeida, A. R.; Colherinhas, G. Molecular Dynamics Study of Functionalized Gold Nanoparticles: Structural and Aggregation Behavior under Varying Ionic Strength. *ACS Physical Chemistry Au* **2025**, *5* (6), 699–715. https://doi.org/10.1021/acsphyschemau.5c00077.
(201) Lee, O.-S.; Schatz, G. C. Molecular Dynamics Simulation of DNA-Functionalized Gold Nanoparticles. *The Journal of Physical Chemistry C* **2009**, *113* (6), 2316–2321. https://doi.org/10.1021/jp8094165.
(202) Xue, Y.; Li, X.; Li, H.; Zhang, W. Quantifying Thiol–Gold Interactions towards the Efficient Strength Control. *Nat. Commun.* **2014**, *5* (1), 4348. https://doi.org/10.1038/ncomms5348.
(203) Maksymovych, P.; Voznyy, O.; Dougherty, D. B.; Sorescu, D. C.; Yates, J. T. Gold Adatom as a Key Structural Component in Self-Assembled Monolayers of Organosulfur Molecules on Au(111). *Prog. Surf. Sci.* **2010**, *85* (5–8), 206–240. https://doi.org/10.1016/j.progsurf.2010.05.001.
(204) Rosas Jiménez, J. G.; Fábián, B.; Hummer, G. Faster Sampling in Molecular Dynamics Simulations with TIP3P-F Water. *J. Chem. Theory Comput.* **2024**, *20* (24), 11068–11081. https://doi.org/10.1021/acs.jctc.4c00990.
(205) Silvestri, L. G.; Johnson, Z. A.; Murillo, M. S. Adaptive Equilibration of Molecular Dynamics Simulations. *Comput. Phys. Commun.* **2026**, *320*, 109989. https://doi.org/10.1016/j.cpc.2025.109989.
(206) Voyiatzis, E.; Valsami-Jones, E.; Afantitis, A. Atomistic Insights into the Morphological Dynamics of Gold and Platinum Nanoparticles: MD Simulations in Vacuum and Aqueous Media. *Beilstein Journal of Nanotechnology* **2024**, *15*, 995–1009. https://doi.org/10.3762/bjnano.15.81.
(207) Sánchez, H. R. Residence Times from Molecular Dynamics Simulations. *J. Phys. Chem. B* **2022**, *126* (43), 8804–8812. https://doi.org/10.1021/acs.jpcb.2c03756.
(208) Goharshadi, E. K. A Review on the Radial Distribution Function: Insights into Molecular Structure, Intermolecular Interactions, and Thermodynamic Properties. *J. Mol. Liq.* **2025**, *433*, 127900. https://doi.org/10.1016/j.molliq.2025.127900.
(209) Helling, R. B.; Goodman, H. M.; Boyer, H. W. Analysis of Endonuclease R· *Eco* RI Fragments of DNA from Lambdoid Bacteriophages and Other Viruses by Agarose-Gel Electrophoresis. *J. Virol.* **1974**, *14* (5), 1235–1244. https://doi.org/10.1128/jvi.14.5.1235-1244.1974.

Appendix

List of Publications

1. **Das, S**., Krishnamoorthy, J., & Kar, R. K. (2025). Estimating the structural and spatial variables of allantoinase enzyme critical for protein adsorption. *Biochemical and Biophysical Research Communications*, *743*, 151161.

2. Kotal, A., **Das, S**., Sarangi, S., Das, N., & Kar, R. K. (2025). Image Analysis for Analytical and Microbial Studies. *Journal of Chemical Education*, *102*(4), 1684-1693.